

AD694093

ESD-TR-69-194

AIRBORNE MEASUREMENTS OF ATMOSPHERIC ANOMALIES

July 1969



AEROSPACE INSTRUMENTATION PROGRAM OFFICE
ELECTRONIC SYSTEMS DIVISION
AIR FORCE SYSTEMS COMMAND
UNITED STATES AIR FORCE
L. G. Hanscom Field, Bedford, Massachusetts

This document has been
approved for public release and
sale; its distribution is
unlimited.

OCT 7 1969

(Prepared under Contract No. F19628-68-C-0321 by EG&G, Incorporated,
Environmental Services Operation, P. O. Box 1022, Boulder, Colorado 80302)

Reproduced by the
CLEARINGHOUSE
for Federal Scientific & Technical
Information Springfield Va. 22151

110

ESD-TR-69-194

AIRBORNE MEASUREMENTS OF ATMOSPHERIC ANOMALIES

July 1969



AEROSPACE INSTRUMENTATION PROGRAM OFFICE
ELECTRONIC SYSTEMS DIVISION
AIR FORCE SYSTEMS COMMAND
UNITED STATES AIR FORCE
L. G. Hanscom Field, Bedford, Massachusetts

This document has been
approved for public release and
sale; its distribution is
unlimited.

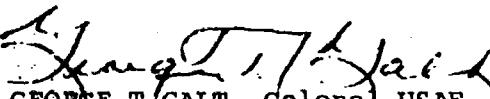
(Prepared under Contract No. F19628-68-C-0321 by EG&G, Incorporated,
Environmental Services Operation, P. O. Box 1022, Boulder, Colorado 80302)

FOREWORD

This report describes work accomplished under Contract F19628-68-C-0321 by E. G. and G, Inc., Environmental Services Operation, P. O. Box 1022, Boulder, Colorado for the Director of Aerospace Instrumentation Program Office, L. G. Hanscom Field, Bedford, Massachusetts. Lt Charles F Schafer, ESSIE, was the ESD Project Manager.

REVIEW AND APPROVAL

This technical report has been reviewed and is approved.



GEORGE T. GALT, Colonel USAF
Director of Aerospace Instrumentation
Program Office

ABSTRACT

Anomalous atmospheric conditions at Western Test Range were measured by aircraft. The inversion layer was found to possess upward warp as it approached the coast, as well as dilation, lensing, sandwiching, and waving. Flow geometry, when associated with topographic obstacles, was found to be markedly similar to that produced on laboratory models. Froude number concepts classified the anomalies accurately. Refraction corrections produced by three possible data sources were compared to assess the effects of the above described anomalies. When data from full cross sections along the sighting path were employed, along with steering equations, elevation and bending corrections were considerably greater (2x) than those produced by single point radiosondes or aircraft spiral measurements. Moreover, corrections produced by spiral data increased to seaward where the inversion became sharply defined. The validity of full cross sections defining the propagation path was best established by examining ray paths for antenna elevation angles existing at the time of signal loss when a target simulation aircraft encountered a radio hole. Ideally, a trapped ray could be expected to bend back to earth at the aircrafts' position in time and space when any one of three tracking radars lost lock on the target. A cross-section corrected propagation path defined this target position better than any other means of defining the path. Strength and distinctive geometry of the inversion at the position of loss are displayed. Mathematics employed for real-time corrections at any angle (including negative) are presented, as are mathematics for steering corrections.

TABLE OF CONTENTS

<u>Section</u>	<u>Page</u>
I INTRODUCTION	1
Structure of the Report	1
II DESCRIPTION OF ATMOSPHERIC ANOMALIES	2
The Hydraulic Jump	2
Aircraft Measurements	5
Case Studies	8
Summary	16
III COMPARISON OF REFRACTION CORRECTION INPUT DATA	21
IV RADIO HOLE MISSIONS	31
June 8, 1967, Radio Hole Mission	33
March 29, 1967, Radio Hole Mission	37
Mission Abort, or Missile Destruction Condition	41
Summary	41
V EXPOSITION ON MATHEMATICS EMPLOYED IN REFRACTION ANOMALY INVESTIGATION	43
Review and Modification of REFRAC Program	43
List of Symbols	44
Review of Pertinent Refraction Correction Principles	48
Modification of Ray Tracing for Simple Computers	50
Real-Time Corrections for Low Angles of Elevation	53
Correction Derived from Using the Curved Radar Path Instead of the Geometric	54
Target Elevation	54
Bending Error	56
A Real-Time Iterative Solution for the Bending	58
Comparisons of Refraction Corrections at Low Angles of Elevation Using the Proposed Real-Time Computa- tions with Those Obtained by Standard Solutions	60
The Anisotropic Atmosphere - A Ray Steering Program	63
VI SUMMARY AND RECOMMENDATIONS	66

TABLE OF CONTENTS (CONT'D)

<u>Section</u>	<u>Page</u>
Summary	66
Recommendations	67
Appropriate Exploratory Work	68
Summary Statement	69
 REFERENCES	 70
 APPENDICES	
Appendix A	
List of Illustrations	73
Range Error	75
Elevation Error	76
Doppler Velocity Error Angle	76
A Quadratic Exponential Model	77
Determination of the Decay Constants - Possible	
Use of the Radar Beam as an Atmospheric	
Probe	78
Appendix B	79
Pacific Inversion Layer Activity	79
General Inversion Description	79
Statistical Compilations and Field Experiments	
on Real Effects of the Inversion	81
Large-Scale Meteorological Studies	87
Summary and Suggestions	100
References	102

LIST OF ILLUSTRATIONS

Figures

- 1 Example of air flow across a ridge with hydraulic jump phenomena.
- 2 Example of hydraulic jump in a kitchen sink.
- 3 Long's laboratory photo of low Froude number.
- 4 Long's laboratory photo of moderate Froude number.
- 5 Long's laboratory photo of high Froude number.
- 6 North section from Tranquillon Peak showing low Froude number.
- 7 North section from Tranquillon Peak showing moderate Froude number.
- 8 Dynamic flow over Tranquillon Peak revealed by clouds, corresponding to moderate Froude number (see Figure 7).
- 9 High-altitude aircraft photo showing mixing zone to west and south of Tranquillon Peak - Point Arguello.
- 10 South cross section from Tranquillon Peak.
- 11 West section from Tranquillon Peak showing 45 minute time variation.
- 12 East-west section through San Nicolas Island.
- 13 High-altitude view of island with bow wake-like structure seen in the stratus deck.
- 14 North-south section through San Nicolas Island showing refraction measurements across the wake structure.
- 15 Ming Wong's computer-produced curves illustrating trapping phenomenon.
- 16 Westerly section from Point Mugu showing regions of trapping associated with the inversion.
- 17 Plot of antenna elevation angle for the 62-102 mile ascent and descent of 8 June (see Figure 16).

LIST OF ILLUSTRATIONS (CONT'D)

Figures

- 18 x-y plot for radio hole measurements, 29 March.
- 19 Actual aircraft instrument traces for inversion penetration in the southwest region of radio-hole pattern, 29 March (see Figure 18).
- 20 Geometry of curvature correction.
- 21 Ray geometry.

SECTION I

INTRODUCTION

The location of this investigation is Western Test Range. The purposes of the investigation were:

- (1) Define the hazards (anomalies) of the atmosphere with respect to their bearing on tracking problems.
- (2) Define tracking accuracies at lower limits (elevation angles zero to 5 degrees).
- (3) Assess currently employed refraction correction techniques • answer the question "How are we doing?"

Structure of the Report

Citing the structure of this report will more easily allow one to identify the logic and interdependence of topics to be presented. Appendix B contains a review of past work on the relation between the north Pacific inversion and radio propagation. The mechanisms of the inversion are explained, the factors controlling its activity (geometric changes and strength changes), are discussed, and field measurements of its effect on radar are reviewed.

Section II, Description of Atmospheric Anomalies, explains the dominant types of anomalies found at Western Test Range. Their causes and spatial distribution are explained. Section III, Comparison of Refraction Correction Input Data, compares amounts of correction applied to a given tracking event as produced by three possible data sources, balloon soundings (Raob); aircraft spirals and fully recorded refraction cross sections along the sighting trajectory. Since these correction outputs are relative to each other, Section IV is devoted to providing an absolute reference for deciding which of the three is closest to reality and how close.

Since we were unable to get the Western Test Range supplied REFRAC computer program to run through the computer, we re-programmed the correction calculations using the original mathematics to maintain consistency. A review of assumptions and possible errors is presented. Since this program is unable to handle the anisotropic atmosphere existing at Western Test Range, a ray steering program was developed. In connection with this effort, a real-time correction technique, good at any angle including negative angles, was produced. Section V presents the structure of these programs and culminates in the handling of steering problems. Appendix A contains supplementary mathematics for Section V. Section VI contains conclusions and recommendations.

SECTION II

DESCRIPTION OF ATMOSPHERIC ANOMALIES

In defining the atmospheric anomalies existing at Western Test Range (including the San Nicolas Island and Point Mugu tracking stations), we wish first to introduce work of Robert Long (1953, 1954, 1955) in flow dynamics, which discusses understanding the flow features pertinent to the anomalies found at Western Test Range. In the present instance we use the term "anomalies" to define the perturbations in the atmosphere which are characteristic of its departure from either a well-mixed standard atmosphere, or from the often generalized stratified atmosphere. A stratified atmosphere can be described as an inversion layer at about the 2,000 ft level with moist marine air below, and subsiding dry air aloft. As a generalized concept, this is correct. As a definition of the specific medium through which missiles are tracked at Western Test Range, it is not correct when one considers low-angle tracking with very accurate radar. Early low-angle acquisition of incoming missiles could be a practical reason for wanting to know more about anomalous propagation, as could the tracking of low-altitude aircraft. Before further description of atmospheric anomalies is discussed, the concept of Froude numbers and flow characteristics should be grasped.

The Hydraulic Jump

When an obstacle is placed in the path of moving fluid, a wave is formed. The geometry of this wave is dependent on the density of the fluid, the height and geometry of the obstacle, and the velocity of the fluid. These relationships are explained as follows (Skalak, 1967).

In open channel flow, the counterpart of the Mach number is the Froude number F , defined as the ratio of the flow velocity V to an elementary gravity wave velocity, $c = \sqrt{gd}$, where d is the depth of flow. For Froude number $F = V/\sqrt{gd}$ less than unity the flow is called subcritical and is in many ways analogous to subsonic flow.

Supercritical is defined as open channel with Froude number $F > 1$. It is analogous to supersonic flow. Flow in a tranquil river is usually subcritical, but rapids are supercritical. Lopez and Howell (1967) wrote of Froude number application to katabatic flow in the Andes. The same is applicable to flow over Tranquillon Peak, the Vandenberg tracking site; and San Nicolas Islands, all of which are units of the Western Test Range trilateration system.

Using

$$v_o = (gh_o)^{1/2} \quad (1)$$

to designate initial flow velocity, gravity, and wave height, Lopez and Howell (ibid) explain airflow: When cool air is considered instead of water, gravity acts on the density differences between the air strata in acceleration the flow, and g in Eq (1) is replaced, at least for relatively small vertical displacements, by

$$\gamma = (\Delta\theta/\theta) \cdot g \quad (2)$$

where θ is no longer constant but dependent on the relative potential temperature difference $\Delta\theta$. The critical spill velocity Eq (1) then becomes

$$v_o = (\gamma h_o)^{1/2} \quad (3)$$

Let us compare two cross sections 0 and 1 (Fig. 1), assuming a frictionless streamline flow. If H_o is the height of the pass over the valley floor, applying Bernoulli's equation to cross sections 0 and 1:

$$\gamma(H_o + h_o - h_1) = 1/2 (v_1^2 - v_o^2) \quad (4)$$

The equation of continuity requires that

$$\text{Discharge} = Q = v_1 h_1 = v_o h_o = \text{Constant} \quad (5)$$

Combining Eq (4) and (5) with the critical velocity of Eq (3) we arrive at

$$(h_o/h_1)^3 - (2H_o/h_o + 3)(h_o/h_1) + 2 = 0 \quad (6)$$

The Froude number, $F_1 = v_1/v_o$ expresses the degree to which the flow is supercritical. The ratio (h_1/h_o) is always less than 1 and equals the shrink ratio between the depth of the supercritical shooting flow at the base of the pass and depth of the overflowing air.

As the valley floor of Fig. 1 flattens, the supercritical velocity of the flow is rapidly diminished by friction and a "tranquil" subcritical flow region is approached. In order to satisfy continuity requirements, the depth of the flow must increase from h_1 to a certain h_2 . If this happens, waves can travel upstream in the subcritical area near h_2 but cannot do so in the supercritical area above h_1 . The wave front will therefore steepen until it breaks down somewhere between cross sections 1 and 2. In this way, a hydraulic jump is formed which tends to remain stationary. A simple illustration of the hydraulic jump may be seen by running tapwater into an empty basin (Fig. 2).

Where the stream hits the basin, a thin sheet of fast-moving water with supercritical velocity is surrounded by a ring of deeper turbulent water. A pencil point set in the thin sheet will create a "shock wave" of the familiar V-shape which clearly does not propagate upstream. This jump is often referred to as the "pressure jump" when it occurs in the air.

Illustration of the above relationship of these parameters was supplied by Long (1953, 1954, 1955) and in motion picture experiments where he showed the flow geometry of waves in a two-liquid medium of two densities as the fluids flowed over the symmetrical obstacle. Long constructed an elongated water tank similar to tropical fish tanks kept by hobbyists, in which he photographed a moving obstacle and the wave caused by the obstacle. In this case, the obstacle moved instead of the fluid, the results being the same. The camera moved with the obstacle, photographing the wave as it proceeded. The geometry of the obstacle was varied, that is, the height-length relationship, as was the velocity of the obstacle through the fluid. Figures 3, 4, and 5 extracted from 16 mm movies of Long's work, show how the shape of the wave is changed with increasing Froude numbers in a two-density stratified system. Figure 3 shows a wave train in the lee of the obstacle which is generated at low Froude numbers in the denser layer (low fluid velocities). Figure 4 shows the convergence of the lower medium on the leeward side of the obstacle as the velocity increases; and shows a hydraulic jump has occurred on the leeward side of the obstacle. In this latter instance, the flow of the fluid is faster than the travel time of any wave that might be propagated on the leeward side of the obstacle and allowed to travel upstream. Since this energy cannot pass upstream, it collects at a point downstream where the velocity drops sufficiently to allow wave generation. At this point, we have a hydraulic jump. With still higher velocities a smooth symmetrical wave forms in the stream over the obstacle, Figure 5. This can be seen in nature, for example, as a standing wave manifested by a symmetrical lenticular cloud over the Sierra Nevada. Referring still to observance in nature, we will see in the following work that the nature of the marine layer and the less dense air aloft at the Pacific Missile Range behave much like the idealized laboratory models seen in the photographs. The marine layer represents the denser medium shown in the photographs. The place of the obstacle is taken by the topographical land mass of Tranquillon Peak or San Nicolas Island. The inversion interface is the line of demarcation between the two fluids in the idealized laboratory presentation. We will see from direct aircraft measurements that the nature of the flow in the vicinity of the tracking sites at Western Test Range is identical to that of the laboratory prediction.

Aircraft Measurements

Aircraft missions were designed to obtain cross-sections along the tracking line of site between Tranquillon Peak and the Minuteman Missile pads 20 miles to the north of Tranquillon Peak; also, a cross-section was taken in the

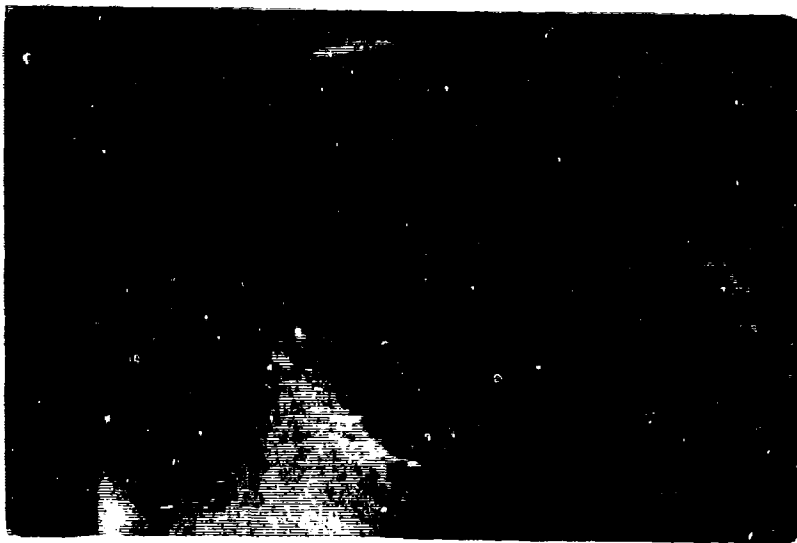


FIGURE 2. Example of hydraulic jump in a kitchen sink.



FIGURE 3. Long's laboratory photo of low Froude number.



FIGURE 4. Long's laboratory photo of moderate Froude number.

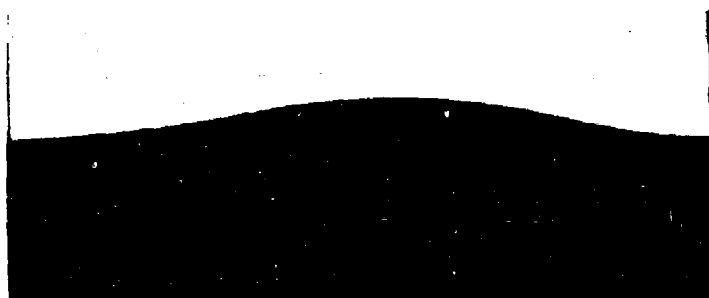


FIGURE 5. Long's laboratory photo of high Froude number.

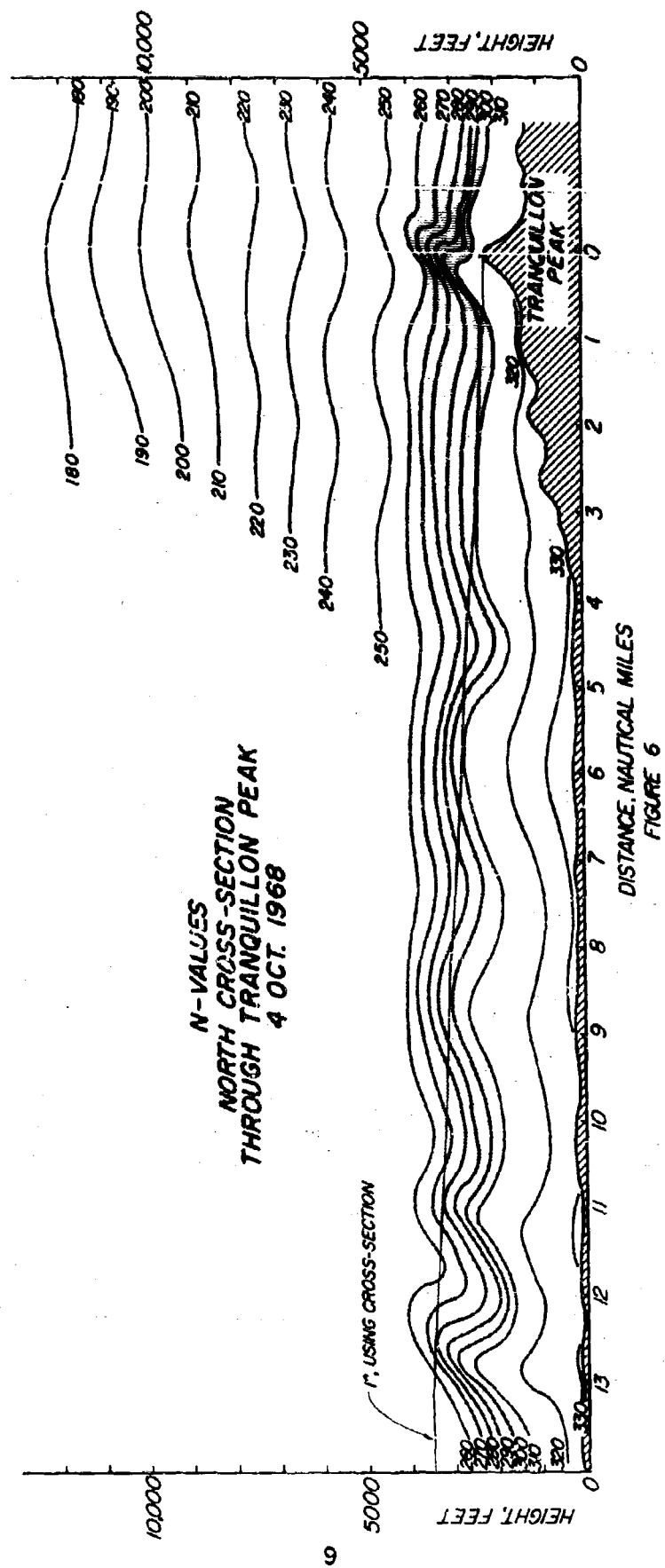
direction of westerly missile trajectories; and a cross-section was taken along the tracking line of sight for north-south orbiting vehicles. Similarly, flights in the vicinity of Pt. Mugu, and San Nicolas Island were flown. In order to obtain these cross-sections, the C-131 airplane equipped with analogue/digital recording refractometer (cycling time = 0.1 sec) radio-altimeter, and other meteorological sensing devices was flown at successively increasing 500-ft levels along the line-of-sight. Variations in the atmosphere observed as waves, lenses, sandwiching of layers, etc., showed up in the variations of the refractometer records. The inversion interface was located, and the aircraft maneuvered through the inversion repeatedly (successive dives and climbs) such that an inversion penetration occurred every 1,200 ft or so. The waves that were measured were on the order of 6,000 ft in wave-length and often much greater. Therefore, about six penetrations per wave were obtained, each penetration marking the altitude of the inversion interface at that particular point. Moreover, the aircraft was flown horizontally through a wave train and the wave fluctuations appeared on the refractometer trace as continuously changing refraction values for a constant altitude. With these inputs, it was possible to reconstruct the structure of the atmosphere along a given cross-section. These reconstructions were made in the laboratory, and the theoretical paths of radar rays (bundles, waves) were traced through these disturbed cross-sections by computer. The laboratory ray tracings are intended to reveal the hazards of the atmosphere in quantitative form (Sections II and III), and indeed must be consistent with actual signal losses experienced in tracking the C-band beacon of the C-131 aircraft.

Case Studies

The following case studies, in the vicinity of Tranquillon Peak and San Nicolas Island, and Pt. Mugu, show the wave form imposed on the atmosphere by thermal and topographic disturbances as defined by our airborne measurements.

Case 1 - 4 October 1968

Figure 6 represents a cross-section between Tranquillon Peak and the northern Minuteman Missile pads. This section is a good example of a low-velocity wave train (low Froude number, Figure 3) triggered by hills just to the northwest of the missile pads, that is, the wave train originates to the left (about 3-4 miles) of the cross-section shown. Surface wind velocity for October 4 was 8 knots. The shaded layer represents the inversion interface, that is the strong gradient zone between the marine layer and the dry air above. This is where the strong refractive bending takes place and is critical to our problem. The significance of this section is that it not only defines the hazards of the Tranquillon Peak Minuteman line-of-sight but also closely approximates the look-angle for System IV (within $\pm 15^\circ$).



Case 2 - Modified Section

More pertinent to the northerly look-angle from Tranquillon Peak is Figure 7, which was modified from a previous diffusion study (Smith, 1964). The modification consisted only in changing the measured parameter potential temperature to refractive index. Since absolute value of refraction needs only to be approximated, the relative distribution of refractivity is the important property. This section was used to emphasize, through use of independent sources, that the perturbations described are real to all field workers and can be found most any time one wishes to make the effort of measuring them; see also Cermak (1966), who shows the same effects in a 1:12,000 topographic model. This (Smith) section is particularly useful. The strong inversion on this day happened to be at an altitude where the marine to dry air interface engulfed the Tranquillon Peak radar. This example shows a cross-section with stronger wind speeds than Case 1, and is a rather typical case where the inversion layer is warped up the mountain on one side and strongly converges in a steep descent on the lee side as in Long's laboratory illustration (see Figure 4, moderate Froude number). Not only is there attenuation of the gradient layer on the downwind side of Tranquillon Peak, but the hydraulic jump and resultant mixing are also evident in the spreading of the refractopleths. Figure 8 shows a photograph of this precise Froude condition. The flow is brought out sharply by the cloud formation which is following precisely the refractopleths shown in Figure 7. In addition, Figure 9 shows where the mixing due to the hydraulic jump manages to destroy the inversion layer locally. The photograph shows a high-altitude view of Point Arguello and Sudden Ranch coastal area. The clear area to the right in the photo is the area of mechanical mixing where the winds are rounding Point Arguello. The dry air above the inversion is mixed into the marine layer, dissipating the cloud droplets. The sharp inversion interface normally found between the marine layer and the dry air above is destroyed here. The cloud erosion in the lower left of the picture shows destruction due to hydraulic jump.

Figure 10 is an aircraft measurement of the inversion layer along the southerly look angle. Note the washing out of the inversion in the right side of the diagram due to the mixing in the lee of Tranquillon Peak as previously explained. As one proceeds to seaward some 20 kilometers the inversion is reinstated in all its strength. At 40 kilometers the inversion is sufficiently strong to produce trapping. We will consider trapping later in Section IV, on radio hole missions.

Case 3 - 30 March 1967

Figure 11 shows the westerly trajectory from Tranquillon Peak to seaward with the perturbation caused by Tranquillon Peak showing very clearly. Note in the diagram that the dashed set of lines shows a section taken 45 minutes



**FIGURE 7. North section from Tranquillon Peak
showing moderate Froude number.**



**FIGURE 8. Dynamic flow over Tranquillon Peak
revealed by clouds, corresponding to
moderate Froude number.(See FIGURE 7)**

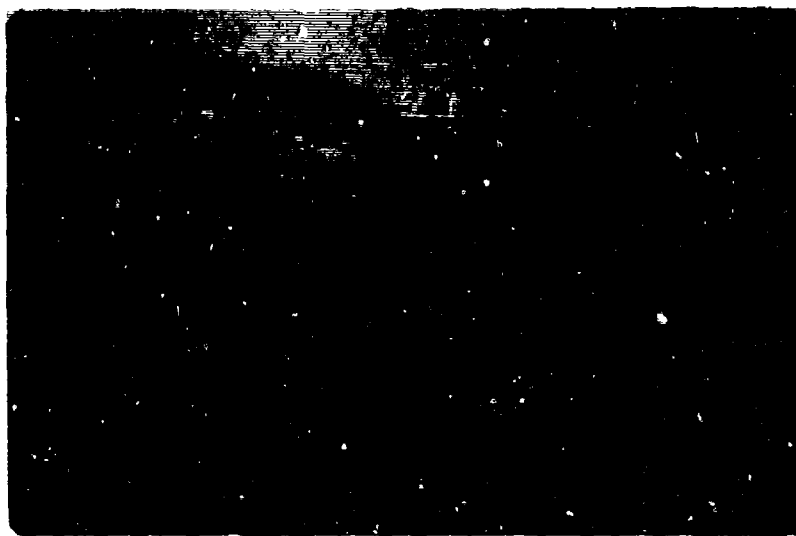
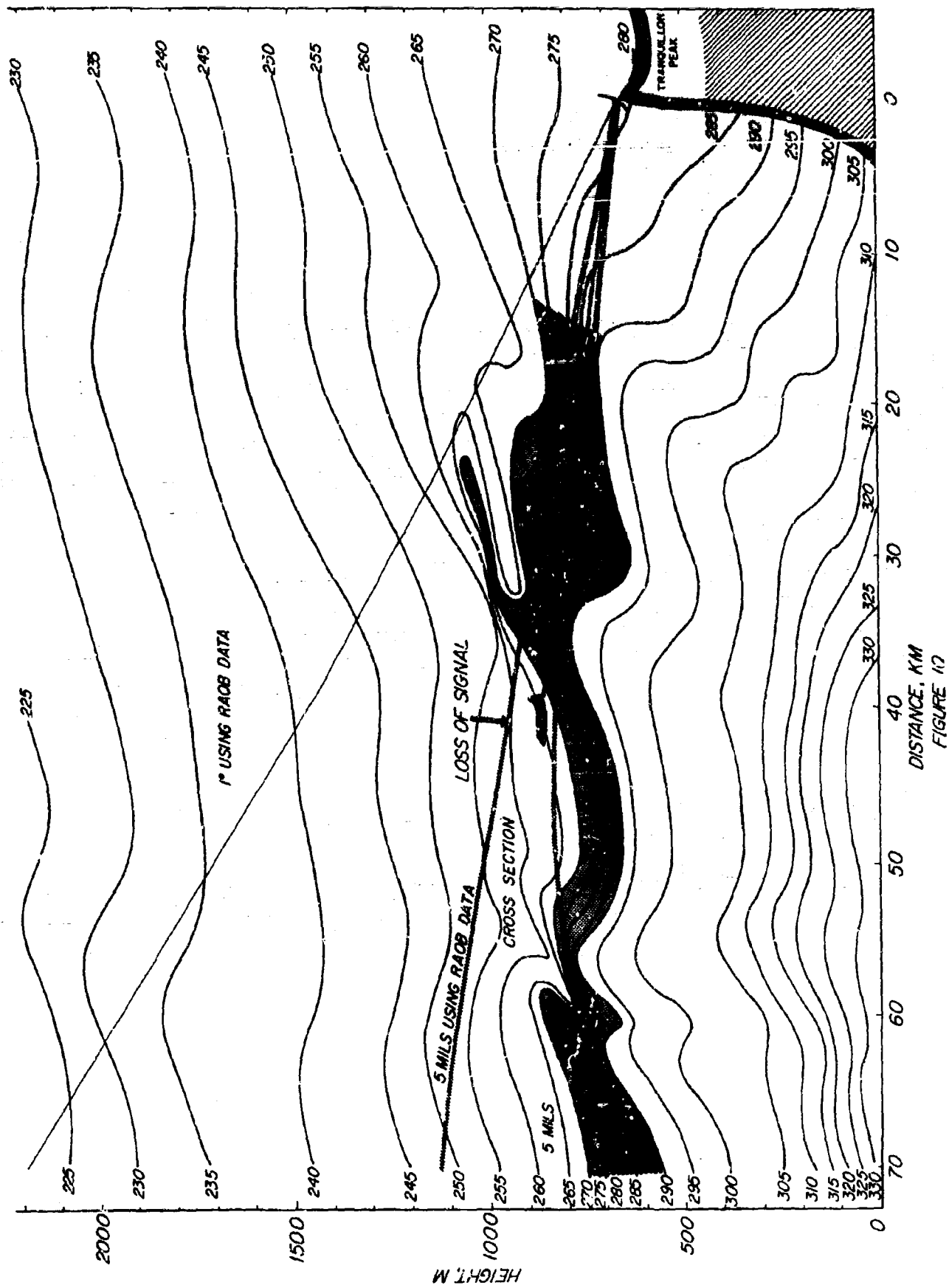


FIGURE 9. High-altitude aircraft photo showing mixing zone to west and south of Tranquillon Peak—Point Arguello.



--- RUN 1 4600-6700 FT. ; START 1400
 --- RUN 2 3800-5700 FT. ; START 1445

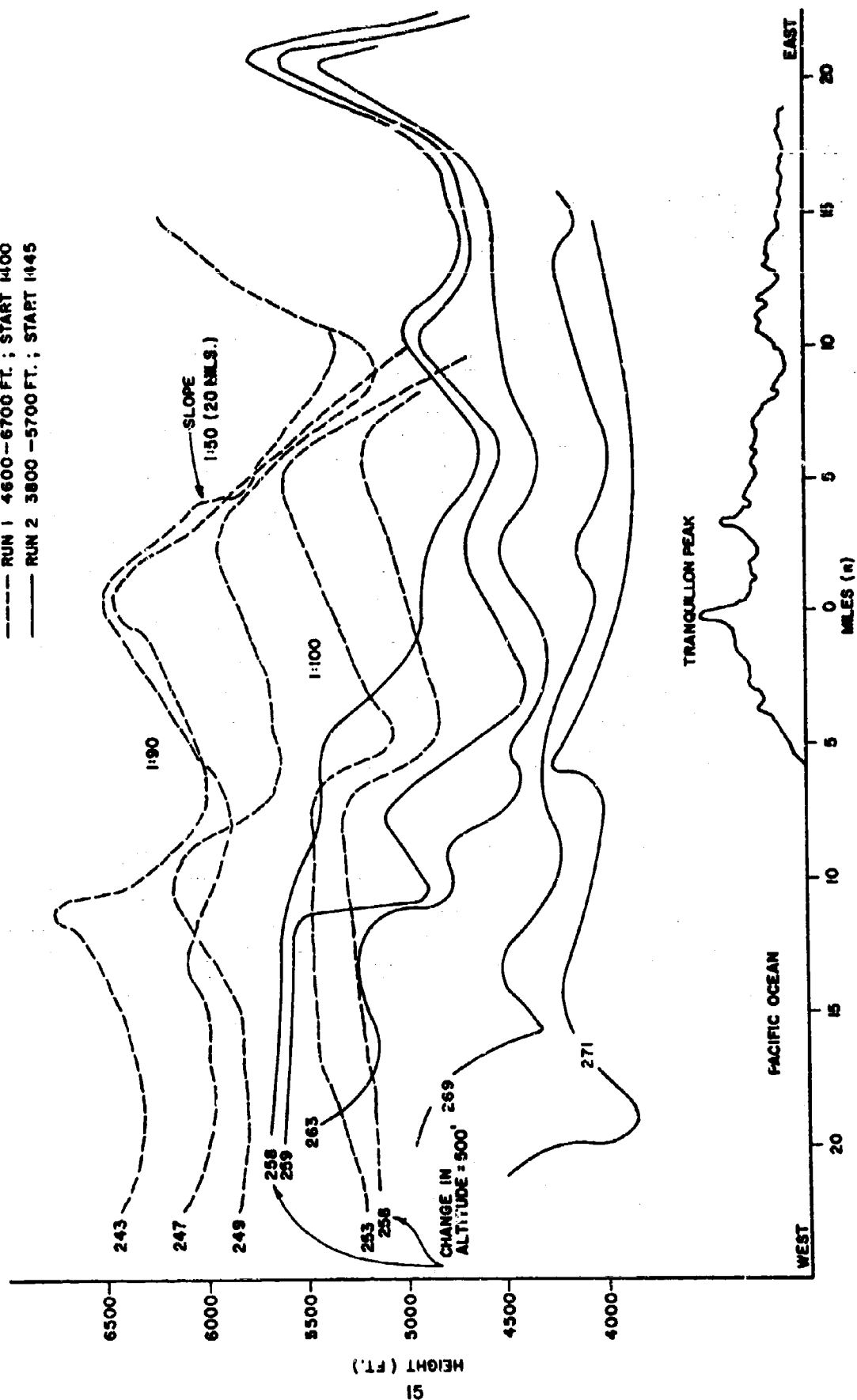


FIGURE 11

after the first section. The general effect of time variation is for the magnitude of the fluctuation to remain constant while the wave nodes shift in spatial position. The significance of this is that from the standpoint of refractive bending the magnitude of error in either case is likely to be much the same. As we follow the inversion to seaward, it stabilizes some 20 or 30 miles out. By "stabilizes" we mean that it becomes strongly stratified at one altitude with a very pronounced gradient layer (as opposed to multi layering, lensing, or complete mixing). These distinctions are not very discernible to single point balloon soundings on the beach (Vandenberg or Mugu).

Case 4 - 24 July 1967

Case 4 is a measurement of the atmosphere over San Nicolas Island on 24 July 1967. Figure 12 is an east-west section along the axis of the island and along the flow of the wind measured by aircraft. Notice how a "bow wave" forms at the windward end of the island. The turbulence effects induced by the topography are evident as a mild hydraulic jump in the right half of the diagram. Strong convergence of the gradient layer over the land mass again is identifiable for the inversion interface at mid diagram. This repeats the moderate Froude number phenomena seen in Figure 7 for Tranquillon Peak. Convergence of the inversion gradient in this manner is extremely significant when examining refractive bending, as is the general tilting and warping and waving of the inversion interface. Generally, the inversion was found to be 300 to 400 ft lower on the north side of the island than on the south side of the island.

Additional clarity of the flow pattern around the island is seen in Figure 13, as viewed from a high-flying aircraft. A wave train progresses out from the "nose" of the island. It is especially evident on the near camera side. Figure 14 shows sections across these waves. There is a doming of the airstream over the center of the island, with two sister perturbations (the V-wake) to either side.

Summary

To summarize the anomaly high points found in these case studies, the following generalizations are made.

1. With prevailing northwest wind, the inversion immediately to the south of Tranquillon Peak is likely to be destroyed by the hydraulic-jump effect associated with sufficiently high Froude numbers. This will often be noticed as an erosion of the cloud deck at inversion height. This circumstance should allow excellent target tracking. The well-mixed atmosphere here will approximate a standard atmosphere. The mixed condition should exist some 20 miles to seaward.

2. Generally, the area immediately to the west of Tranquillon Peak

This is a contour map of a coastal area, likely a runway or airfield. The map shows elevation contours ranging from 250 to 350 feet. Key features include:

- LOW WIND-LINE STRUCTURE:** Located on the left side of the map, near the 350-foot contour.
- RUNWAY ZENITH:** A point marked on the map, near the 250-foot contour.
- HYDRAULIC STRUCTURE:** A point marked on the map, near the 250-foot contour.
- INVERSION CONVEGENCE:** A point marked on the map, near the 250-foot contour.
- ELEVATION ANGLE = 1°:** Two dashed lines indicating the elevation angle, one near the 250-foot contour and another near the 300-foot contour.
- Westerly Winds, 15 kts:** A label indicating the direction and speed of the winds, pointing towards the right side of the map.
- SAN NICOLAS IS.:** A shaded area on the right side of the map, representing the island.
- Runway:** A line labeled 'RUNWAY' on the right side of the map.
- Compass Rose:** A compass rose in the bottom right corner indicating North (N) and West (W).

The map also includes a scale bar at the bottom, ranging from 0 to 4000 feet.

FIGURE 12



**FIGURE 13. High-altitude view of
island with bow wake-like
structure seen in the stratus
deck.**

**N-VALUES
S-N CROSS-SECTION
THROUGH SAN NICOLAS IS.
24 JULY 1967**

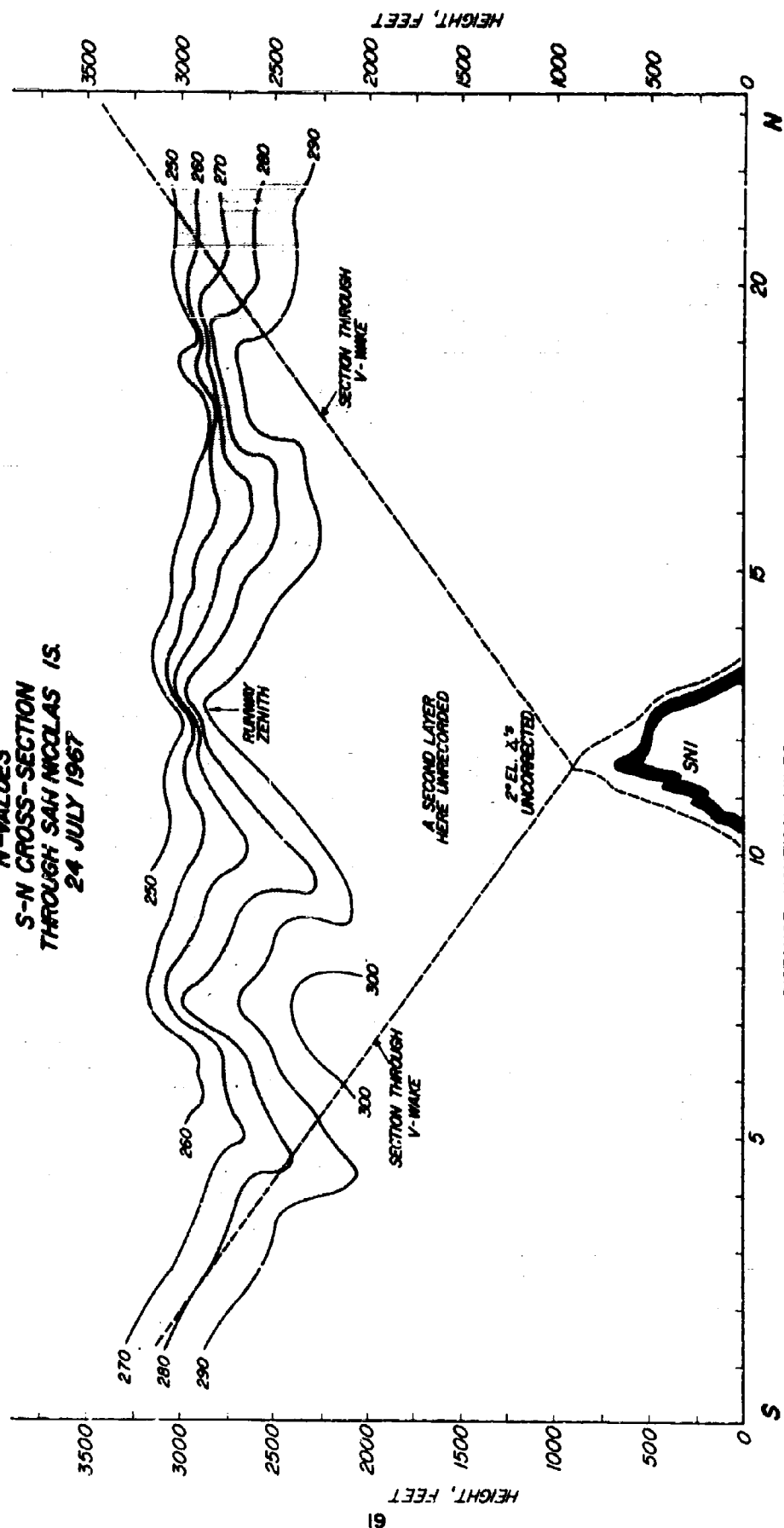


FIGURE 14

will have low-level mixing due to eddying around the land mass itself, in which case one will find a clear sky area along the beach where the mixing has eroded the cloud deck (present at inversion height). At higher altitude one will find a set of standing waves from the disturbance of the peak itself. Occasionally, serious tracking errors can be produced by strengthening of the gradient layer a short distance to seaward (~ 10 - 20 nm).

3. In the northerly sections wave trains across the Santa Inez Valley can be expected. The inversion may also have a warped geometry, which seemingly climbs upward to meet Tranquillon Peak. This warping can actually be seen by a ground observer on the north hills when the low morning sun scatters off the haze layer. The trapping and bending significance of a warped or tilted inversion layer will be discussed in the section on radio hole missions.

4. A slight elevation difference in the inversion will exist between the north and south sides of the San Nicholas Island. The gradient layer will bulge over the island on the order of 1,000 ft. A wave structure will propagate out to the north and south sides of the island. There is strong convergence of the gradient layer eastward of the mid point of the island, and a hydraulic jump induced mixing of the inversion layer downwind of this.

5. The inversion at Point Mugu may be washed out from eddy mixing associated with shear where the sea breeze front meets the north westerlies. It can also be multi layered or lensing under moderately weak stability conditions (to be seen in Figure 16, Section IV, 8 June example). The seaward strength of the inversion may be experienced close along shore at Point Mugu when strong stability conditions are present.

SECTION III

COMPARISON OF REFRACTION CORRECTION INPUT DATA

Having established the complex nature of the atmosphere at Western Test Range (Section I), quantitative estimates should be made of the differences in various tracking errors as they depend on the source of their calculations inputs. Comparisons made by Gardner (unpublished) show there is little difference in corrections to be made as a function of formulae used. The reason, of course, is that all calculations are based on Snell's Law. It will be apparent in the section, however, that one cannot afford to ignore the validity of the inputs. One faces the question "How realistic are the measurements being fed into the refraction correction calculations?"

In order to keep the comparisons valid we must use common radar elevation angles (1°), common target altitudes, and approximately the same points in time for a given day. Tables 1-6 represent measurements within an hour of each other. Altitudes are limited by the spiral height of the aircraft. Calculations are compared at this minimum height. The important points of conformance are that targets be above the anomalous section of the atmosphere. In all cases it is the relative difference in tracking errors for a given day that we wish to isolate. The general magnitude of error is of secondary interest.

The Table 1 format displays range error, elevation angle error, and bending error, as calculated for a 12,000 ft elevation refraction profile measured on 4 October 1968. The primary comparison is for the line of sight between Tranquillon Peak and the Minuteman pads located about 20 miles north of the Peak. The cross-section measurements produce bending corrections about 30 percent greater than the Vandenberg Raobs produce (7.2 versus 5.6 mils). The 65 percent difference in elevation-angle error between extreme correction values is a valid comparison for this date or other dates of comparable target altitude and range.

A secondary comparison included in Table 1 is between Point Mugu and San Nicolas Island Raobs. Although not applicable to a north cross-section comparison for Tranquillon Peak radar, the data are applicable for comparison of tracking corrections from Tranquillon Peak to the western or southern horizons respectively. One might accept the thesis that because of horizontal homogeneity far off shore a San Nicolas Island Raob is more representative of the atmosphere for Tranquillon Peak at low angles to the west over the ocean than a balloon sounding over Tranquillon Peak itself. In such case, one might employ the SNI Raob as the best representation of the atmosphere. Similarly, the same can be said for the Point Mugu relationship to Tranquillon Peak for Southern look-angles (in the near shore mixing zone). The Mugu and Vandenberg

TABLE I
COMPARISON OF REFRACTION ERRORS
VANDENBERG - NORTH
4 October 1968

Input Source	Range Error Ft	Elev. Error Mils	Bending Mils
VBG Raob ⁺	100.8	3.58	5.60
SNI Raob ⁺	104.0	2.67	4.70
Mugu Raob	102.3	3.92	6.02
TPK Spiral*	99.4	3.78	6.04
Cross Section	99.6	4.40	7.20
	TPK Spir/Mugu Raob	SNI Raob/Sect.	SNI Raob/Sect.
Extremes	99.4 - 102.3	2.67 - 4.40	4.70 - 7.20
% Difference	3	65	53
Conditions:			
Elevation angle used = 1°			
Target height = 12,000 ft.			
*Located directly over Tranq. Peak (TPK)			
⁺ As applied to TPK radar			

TABLE 2
COMPARISON OF REFRACTION ERRORS
POINT MUGU - WEST

8 June 1967

Input Source	Range Error Ft	Elev. Error Mils	Bending Mils
Mugu Raob	Not available for this time frame		
Mugu Spir 1*	86.7	2.75	4.22
Mugu Spir 2 ⁺	89.8	3.97	5.33
Mugu Section	110.0	3.50	6.00
	Spir 2/Sect.	Spir 1/Sect.	Spir 1/Sect.
Extremes	86.7 - 110.0	2.75 - 3.97	4.22 - 6.00
% Difference	27	44	42
Conditions:			
Elevation angle = 1°			
Target height = 10,500 ft			
*Located 8 nm west of Point Mugu			
⁺ Located 18 nm south of Tranq Peak, 75 nm west of Point Mugu			

TABLE 3
COMPARISON OF REFRACTION ERRORS
VANDENBERG - 250°
8 June 1967

Input Source	Range Error Ft	Elev. Error Mils	Bending Mils
VBG	86.9	2.97	4.54
Spir 2*	89.8	3.97	5.33
Spir 3 ⁺	26.0	4.31	5.53
TFK Section	90.2	1.80	3.20
	Spir 3/N. Sect.	W. Sect./Spir 3	Sect./Spir 3
Extremes	86.0 - 90.2	1.80 - 4.31	3.20 - 5.53
% Difference	5	140	73
<p>Conditions:</p> <p>Elevation angle = 1°</p> <p>Target height = 10,500 ft</p> <p>*18 nm south of Tranq Peak</p> <p>⁺57 nm west of Tranq Peak</p> <p>Table 3 compares the possibilities open for Tranq Peak refraction correction for polar orbit shots.</p>			

TABLE 4
COMPARISON OF REFRACTION ERRORS
VANDENBERG - WEST
30 March 1967

Input Source	Range Error Ft	Elev. Error Mils	Bending Mils
VBG Raob	49.0	1.10	2.17
Spir 1*	49.9	1.24	2.25
Spir 2*	49.9	0.79	1.95
TPK Section	65.0	1.60	3.10
	Raob/Sect.	Spir 2/Sect.	Spir 2/Sect.
Extremes	49.0 - 65.0	0.79 - 1.60	1.95 - 3.10
% Difference	33	103	59
Conditions:			
Elev. angle = 1°			
Target height = 7,000 ft			
*Located 30 nm and 15 nm west of TPK coast, respectively			

TABLE 5
COMPARISON OF REFRACTION ERRORS
VANDENBERG - 242°

29 March 1967

Input Source	Range Error Ft	Elev. Error Mils	Bending Mils
Spir 1*	67.7	1.96	3.19
Spir 3 ⁺	63.0	1.08	2.33
VBG Raob	66.2	1.28	2.55
VBG Section	64.6	1.60	3.20
	Spir 3/Spir 1	Spir 3/Spir 1	Spir 3/Sect.
Extremes	59.5 - 67.7	1.08 - 1.96	2.33 - 3.20
% Difference	14	82	38
Conditions:			
Elevation angle = 1 degree			
Target height - 8,000 ft			
Radar height = 2,159 ft			
*45 nm south of Tranq Peak			
⁺ 8 nm west of Point Mugu (within mixing zone)			

TABLE 6
COMPARISON OF REFRACTION ERRORS
SAN NICOLAS ISLAND - EAST-WEST

24 July 1967

Input Source	Range Error Ft	Elev. Error Mils	Bending Mils
SNI Raob	47.2	2.58	4.25
Splr *	49.0	3.68	4.40
W. Cross Section	51.7	3.70	6.60
E. Cross Section	62.4	7.80	9.70
	SNI Raob/Sect.	SNI Raob/Sect.	SNI Raob/Sect.
Extremes	47.2 - 62.4	2.58 - 7.80	4.25 - 9.70
% Difference	32	202	128
<p>Conditions:</p> <p>Elevation angle = 1°</p> <p>Target height - 4,200 ft (inversion top goes to 4,000 ft in places)</p> <p>Radar height = 860 ft</p> <p>*Spiral located between Anacapa and San Nicolas Islands. Ray traps for these measurements at 6.14 mils.</p>			

data presented show the corrections are reasonably close. It is contrary to this reasoning that SNI produces less of a bending correction than shore, or near shore, measurements, such as displayed in Table 2. The errors should increase to seaward as the inversion stabilizes and the marine air dry air interface becomes very sharply defined. This will be confirmed by the Table 7 summary and will show also that full cross sections to seaward produce even greater corrections than the seaward spirals, except for the Table 3, June 8, Vandenberg section, Figure 16. This 8 June section is very similar to that of 29 March, Figure 10, with complete washing out of the gradient near the coast. One can see in Figure 16, that the one-degree ray passes well above the sharp inversion, having penetrated in the well-mixed zone closer to the coast, thus explaining the exception. Recall how the cloudless zone of Figure 9 and the hydraulic jump of Figure 7 define this inversion destruction phenomenon.

In Table 4, Spiral 2 is least like the output from the cross section. Spiral 2 is located in the coastal mixing zone (well mixed from mechanical eddying induced by the mountainous coast itself). Spiral 1, 30 miles to sea, is most like the cross section.

Again in Table 5, the more seaward measurements produce the greatest bending error with the 8-mile spiral (within the well-mixed zone on this occasion) producing the smallest errors.

Table 6 presents a comparison between Raob, Spiral, and Cross Section for SNI. There is only a 3 percent difference in bending between the balloon data and aircraft spiral data. In this case, the spiral is well to seaward and would not be expected to differ greatly from the SNI balloon (Figure 11), which can be seen to penetrate the dynamically sharpened inversion. The cross-section tracing differs from the balloon data by 128% due to the effects of steering which are included in the cross-section correction. Note also a considerable difference in ray traces through a west section and an east section of the disturbed atmosphere. To add to the variation, a weak split inversion was found at many times (0315 LST, SNI Raob) and places (Spiral 2) on this day. The east-west section of Figure 11 shows the upper inversion (between the 290 and 260 refractopleths) dilated in the region of the islands "bow wave". There is a short contraction of refractopleths on the island's downslope, followed by a slight jump two miles downstream of the island (see Froude number explanations of flow characteristics in Section II). The upper inversion sharply contracts again downstream of the hydraulic jump. Here the one-degree ray receives a second harsh bending, which it does not receive in the west section, thus the difference in bending errors in Table 6 between east and west sections.

Table 7 is a summary of Tables 1-6. Since there is present a limited amount of statistical items, the data only suggest trends. The cross-section data

TABLE 7
SUMMARY OF TABLES 1 - 6

Date	Range Error Extremes	Elev. Error Extremes	Bending Error Extremes
4 Oct 68 % Difference	Spir/VBG Raob 3.1	SNI Raob/N. Sect. 64.8	SNI Raob/N. Sect. 53.0
8 June, Mugu	Spir 1/W. Sect. 26.9	Spir 1/W. Sect. 44.3	Spir 1/W. Sect. 42.4
9 June, VBG	Spir 3/W. Sect. 4.9	W. Sect./Spir 3 139.5	W. Sect/Spir 3 73.0
30 Mar 67	VBG Raob/W. Sect. 32.7	Spir 2/W. Sect. 102.6	Spir 2/W. Sect. 59.0
29 Mar 67	Spir 3/Spir 1 13.8	Spir 3/Spir 1 81.5	Spir 3/W. Sect. 37.8
24 July 67	SNI Raob/W. Sect. 32.0	SNI Raob/W. Sect. 202.3	SNI Raob/W. Sect. 128.0
Weighted Ave. % Diff.	17*	107	68
Spiral positions:			
4 Oct 68, VBG; at Tranq. Peak			
8 June 67; 8/270° Mugu			
8 June 67; 57/270° VBG			
30 Mar 67; 15/270° VBG			
29 Mar 67; Spir 1, 45/180° VBG			
29 Mar 67; Spir 3, 8/270° VBG			
*About 24% when considering the 4 section cases only.			

produces the greatest correction requirements for range error in 4 out of 6 cases by 24 percent. The weighted average separation of extremes is 17 percent. The cross sections produce an average of 64 percent greater bending error in 5 out of 6 cases. The average separation of extremes is 68 percent. There is a degree of confirmation, though limited, that Raobs and near coastal aircraft spirals (<15 nm) produce less error than seaward measurements. The atmosphere along the coast is better mixed. If the inversion is present it is split or dilated and higher in altitude. As could be expected, the greatest percent differences are found in the elevation errors, which are also the most critical for single radar target positioning.

Two shortcomings of this analysis are readily apparent in this data. One is the small number of statistics. A greater number of cases is certainly required before the argument can be called well founded. Support for the magnitude of variation is available in the work of Rowlandson and Herlihy (1968). Comparing aircraft spirals only they find time and space variations of the order of .5 mils for 1° antenna elevation angle when a series of spirals are compared, or seasonal groupings are compared. The second and more serious shortcoming is that comparisons have to be made against each other. An absolute reference against which all techniques of correction formula development and data gathering systems can be compared is urgently needed in this type investigation. To this end we progress to the following block of work on radio holes, which can be made to serve as this reference. It will be shown that the cross-section data inputs are closer to reality by a significant amount (2x) and would produce the greatest accuracy for low angle tracking.

SECTION IV

RADIO HOLE MISSIONS

The nature of this investigation essentially revolves around the problem of bending errors as they are affected by atmospheric anomalies. Fortunately, range errors suffer less deviation than bending errors, as they are solely dependent on retardation of wave travel. Their travel time through the anomalies is small compared to total travel time. Bending errors, on the other hand, respond to the sharpness of gradient between the anomalies and the ambient condition which produces a differential in travel speeds for portions of a wave traveling through the gradient. The small retardation error means that a target can be positioned within a very small triangle of error in the horizontal plane, using ranges from a radar triangulation system. However, the vertical bending of rays is sufficiently great at low tracking angles such that accuracy of position in the vertical plane goes out of tolerance. If one assumes a target to be located within acceptable accuracy in the horizontal plane, and the target itself supplies an accurate measure of altitude, a position is obtained which can serve as absolute reference for the analysis of bending errors. An aircraft with C-band beacon using a radar altimeter can perform such a simulation. The aircraft's down-facing radar altimeter is not affected by the anomalies in the context of this problem, and can be considered accurate to within 40 ft. If this beacon-equipped aircraft flies to seaward above the anomalous condition and experiences Loss of Signal (LOS), or severe signal distortion, allegedly due to anomalous conditions, then some combination of refraction correction formulae and data inputs should be able to predict the position of this signal loss better than others. Since it makes little difference which correction formula is used, concentration in this analysis is centered on the role played by possible data inputs and a consideration of ray steering. We intend to show which of the already presented (Section III) data collection techniques provides the most valid measurements of the atmosphere. If the measurements have produced the right amount of ray bending, they should identify with radio holes actually found in the field; that is, the rays should go negative (bend back to earth) precisely where signal is lost on the simulation target. Or, at least one set of measurements should make a better prediction of signal loss than the others. A short explanation of radio holes and ray steering is inserted here. The time and position occurrence of these radio holes is to serve as our absolute reference.

Figure 15, by Ming Wong (1951), shows diagrammatically the causes of a radio hole. Observe the series of ray traces at different elevation angles, from a transmitter at 4,000 ft elevation. Note that an inversion layer of $\Delta N = 60$, is located at 5,000 ft elevation. As the grazing angle of the propagated wave decreases, there comes a point at which the wave front, represented

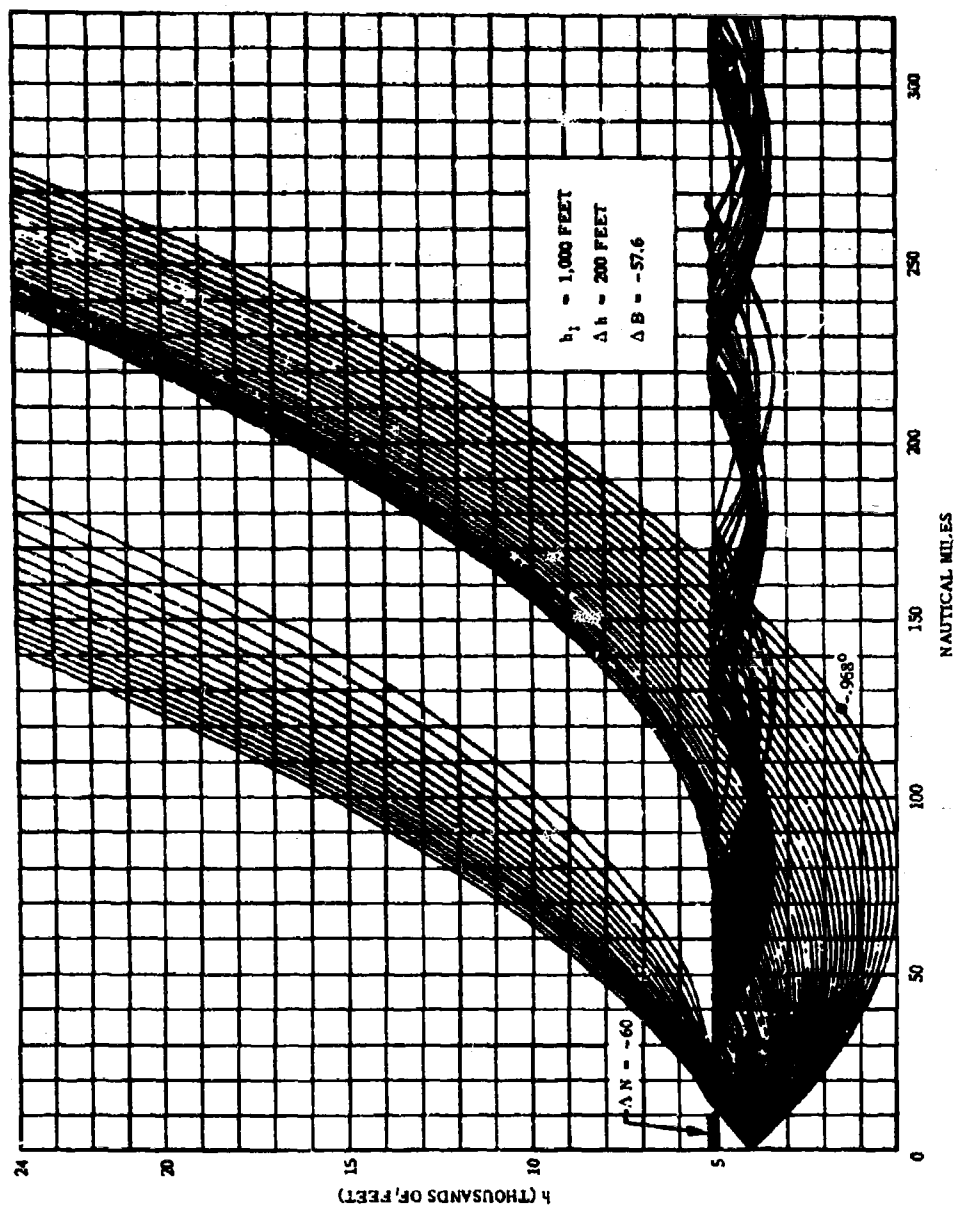


FIGURE 15

as rays, perpendicular to the front bends back into the atmosphere below the inversion layer, thus producing the gap occupying the center of the graph. This is due to retardation of the lower portion of the wave in moist air and velocity increase of the upper portion in the dryer air. As a consequence of the bending, ducting (or trapping) occurs within the inversion layer, which acts as a wave guide, and the signals are propagated beyond the normal radio horizon. This shows up in Ming Wong's diagram as the lateral continuation of waves at the 5,000 ft level. The trapping can be advantageous for acquiring a target over the horizon, but presents a problem for a target in the radio hole. The significance of this loss of track is that the tracking radar, no matter how short the period of loss, must re-acquire the vehicle in flight. Recalling that missiles are traveling on the order of thousands of feet per second, decisions regarding missile destruction, or the attempt at re-acquisition must be made in near real-time. There is also a significance to low flying attack aircraft which is self evident. (Tabulated and diagrammatic compilations of trapping conditions in general have been compiled by Ming Wong, *ibid*; Stanfield, 1962; and Kauper, 1965.)

It has been customary in the past to assume the atmosphere to be horizontally homogeneous, with simple stratification in the vertical plane. The stratification is a manifestation of inversion layer presence. Cunningham, Vickers, Fain (1963) and Cunningham, Myers and Crane (1964) attempted to define and ray trace through horizontally anomalous conditions (inversions and cumulus clouds) at Cape Kennedy. The present work specifically treats the Pacific inversion. For this purpose, we introduce ray steering, as distinct from currently employed ray tracing, to account for tilting and strong local variation of gradient. The rays were steered through the cross sections. To do this, bending as a function of refraction gradient and increasing horizontal distance was extracted from the cross sections and combined with the earth curvature correction to produce the corrected elevation at successive points in space. The elementary increments were chosen sufficiently small and varied to respond to the scale sizes of the anomalies with which we worked. A simplifying mechanism and distinctive feature of the treatment is the employment of MERS (Milli - Earth - Radii) as a fundamental unit of measurement. Details are discussed more fully in Section IV. The significance of trapping is fully realized in the case studies presented below.

June 8, 1967, Radio Hole Mission

Figure 16 shows the cross section for a westerly look-angle from Point Mugu on 8 June 1967. We have previously covered the description of the inversion, and will only call your attention to its upward warping, dilation, lensing, and consequent weaker gradient toward the beach; and its convergence and somewhat undulatory nature to seaward. These are features that have strong influence on the refraction problem. The wave-like convergence at 70-80 miles produces severe bending for low-angle rays.

Figure 1E is a detailed chart showing aircraft track and signal loss data. The chart includes a coordinate grid with latitude (12° 0' to 12° 45' N) and longitude (170° 0' to 175° 0' W). It features several tracks labeled 'SPIRAL 1' through 'SPIRAL 4' and 'P USING CROSS SECTION'. A legend in the bottom left corner defines symbols for 'LOSS OF SIGNAL', 'ACQUISITION OF SIGNAL', 'A/C TRACK', 'A/C INDICATED POSITION', 'A/C FIX', 'WEAK SIGNAL', and 'REFRACTIVE INDEX VALUES'. The chart also includes a 'VISUALLY OBSERVED MOISTURE LENSES TO SEAWARD' area and a 'BEGIN AIRCRAFT TRACK' point. Various data points are plotted, including 'LOS' (Loss of Signal) and 'AOS' (Acquisition of Signal) times and positions.

It is this bending that we wish to examine. Checking the original radar record, Figure 17, the z plot of the aircraft climb and descent shown on the cross section between 62 and 102 miles is clearly recorded with correlating time hacks. As the aircraft descended the radar elevation angle (z plot) began to weaken. At 1828 the z plot of Figure 17 indicates about 6,200 ft uncorrected for refraction. The radar altimeter indicates 5,400 ft at this time. The 1830 radar altimeter position of the aircraft is also fixed in Figure 16, against which can be compared the 1830 rays produced by cross section and spiral data. Since no Raob is available for Point Mugu, a spiral 8 miles off the coast is used, which should be a faithful substitution. The refraction uncorrected ray is also shown. The radar at 1830 is near 3.4 mils antenna elevation. The cross-section data indicates the aircraft to be 3,000 ft higher than its true position, and the spiral (Raob) data indicates the plane to be 5,400 ft higher. (It is true that these numbers are not accurate.) When the radar goes unstable, it is difficult to pick an instant in time and assign an elevation angle to it. This can be readily seen in Figure 17. The instant of signal loss represents a rapidly decaying signal to noise ratio. The acceptance level of 3 db above noise is a statistical criterion. Nevertheless, the gross differences indicated on the diagram show the order of discrepancy involved. This is evidenced in the approximation to radio horizon. Note the uppermost points of signal loss on the aircraft track slightly below the 0.0 mil ray. This ray roughly represents the radio horizon as derived through using cross-section inputs for refraction correction. The line of demarcation can be made out in the diagram, except for the 1948 LOS position which is very low, and the 2015 AOS which is very high. The 1830, 2035, 1841, 2003, and 1957 position (from low center to upper left of diagram) define a fairly believable line. The line suggests that the cross-section corrections for the 0.0 mil ray are still a trifle lean. In theory, a properly corrected 0.0 mil ray should lie on the points of signal loss.

Of further interest in Figure 16 is the data consistency of the 3-mil ray (trapped in the inversion). We know that the aircraft suffers an increasingly poor signal starting from about 1828 on the z plot. Somewhere between 1829-1831 the z and x-y plots indicate loss of lock. Around 1829.5 the z plot indicates about 3.4 mils, as close as we can estimate. According to our ray trace, 3.4 mils looks like the last of untrapped rays. At 3 mils (very close to our actual LOS elevation angle) severe bending takes place. The 3-mil ray becomes trapped. It is ducted westward and just misses the short lock acquired at 1917 as the aircraft came through the gradient layer. It is unusual to see this ray steer its way through the actually measured sections of live signal between the 100 and 120 mile points. The fact that it misses the opening at 180 miles by only 200 meters is not very disconcerting. The order in the data indicates that from the extremely complex set of measurements a sensible body of logic emerges from which significant assessments can be made.

The data of the 8 June mission support the thesis that Raobs, or near-shore

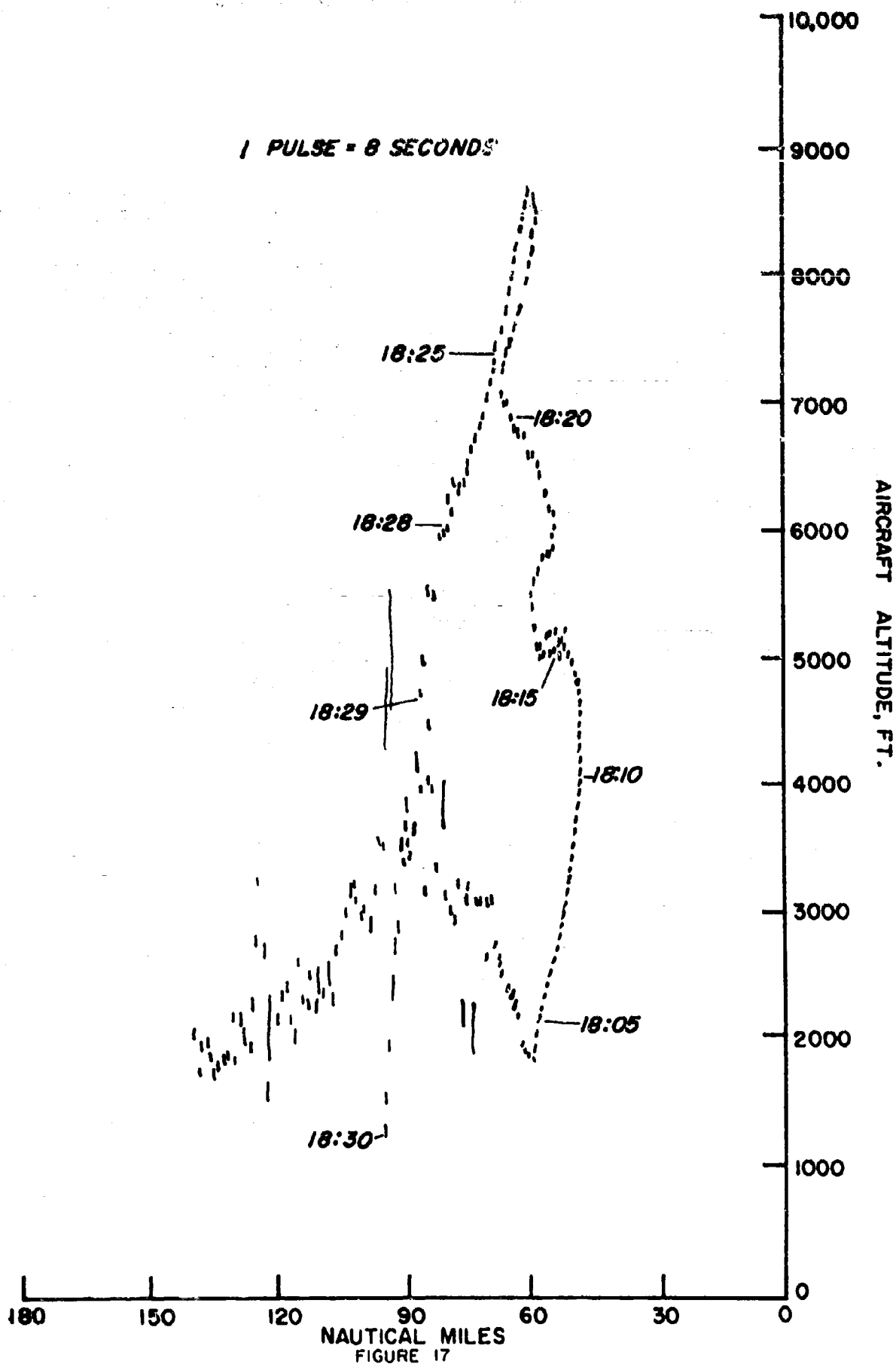


FIGURE 17
36

spirals are not the best way to define the atmosphere for refraction correction. We conclude in general that in the vicinity of 0.0 mils. at 100 nm, the cross-section corrected ray is high by about 2,200 ft. The Raob spiral is high by 4,800 ft. With no further effort than the present project, we can state that low-angle refraction errors can be halved by flying cross sections. Further experimentation could well improve this.

March 29, 1967, Radio Hole Mission

The plan for the radio hole missions called for the pilot to be informed by radio when a particular radar lost lock. The aircraft would continue on to seaward just above the inversion until there was an acquisition of signal, that is, the aircraft would fly through the radio hole. When signal was re-acquired, the aircraft would go into a down spiral through the gradient layer, and after passing through the gradient layer, pick up a return course toward the beach employing a porpoising maneuver up through the layer and back down again. This would continue until the radar operators informed the pilot that the plane had come back to its original loss of signal position on the shoreward side of the hole. At that point it would go into an upward spiral, again sounding the gradient layer on the way through. The upshot of this was that the aircraft got very fine detail with adequate data points in the immediate vicinity of the loss of lock. What we hoped to learn was what the inversion layer looked like (geometry or gradient intensity) at the immediate point of signal loss.

Figure 18 is an actual flight track which follows this plan. It is of interest to proceed around the circuit to show the correlations between radar signals and the structure of the inversion. First, notice the cyclical wave-like course plotted by the SNI radar in the vicinity of VBG radio hole (2141:04 - 2144:52). We have superposed a copy of the refractometer trace above the indicated radio hole on the diagram. It is of interest that the spacing of waves as indicated by the refractometer as the aircraft holds a steady 2,900 ft altitude is coincident with the general size of the distortions in the SNI radar. It follows logically that while sighting obliquely across a wave crest at a target crossing the crests at near crest height an azimuth variation can be produced between times when the line to the target is wholly within the marine air medium, and those times when it emerges near the target in dry air troughs between the crests. This may explain the apparent correlation between wave crests, recorded by refractometer, and track variation recorded by SNI. The speculative quality of this statement is emphasized.

Proceeding to the descending spiral left turn at the end of the west-bound leg (Figure 18), the top of the gradient layer was penetrated at 47:16. SNI lost track 16 seconds before the gradient layer was penetrated. Note, however, that Point Mugu weakened for only 16 seconds (4 data points), then came back on strong as the inversion layer was penetrated, suggesting that the inversion

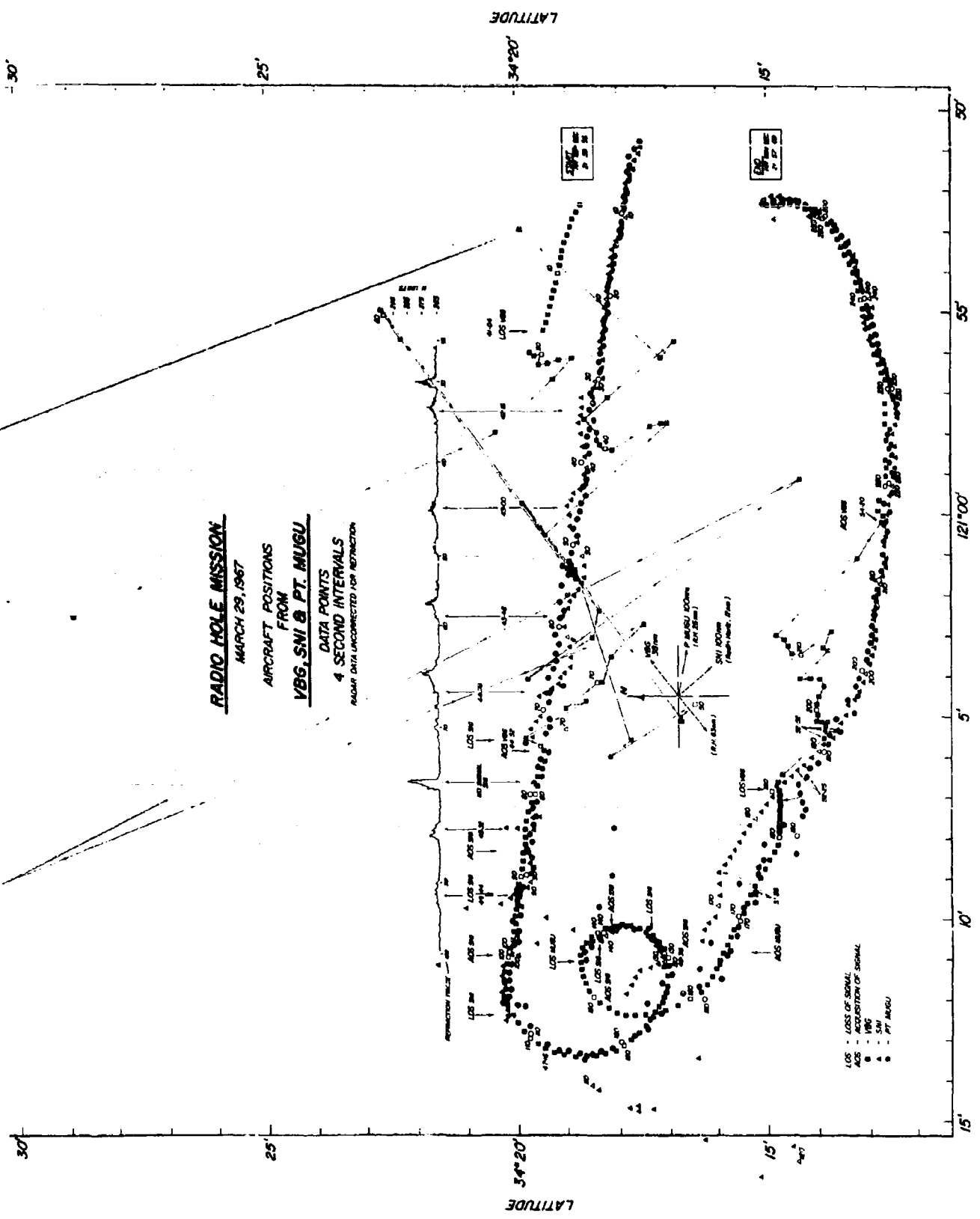


FIGURE 18

was carrying a strong Point Mugu signal within its "wave guide". Signal from SNI, however, was blocked by the inversion and did not come back until 1430, and did not give a reliable position until the bottom of the gradient layer was passed through precisely at 48:36. The aircraft stayed below the inversion with weak, intermittent and disagreeing signals. The aircraft hit the bottom of its descent at approximately 51:28, then began climbing at that point until the base of the gradient layer was intercepted precisely at 52:25.

The actual instrument traces from this penetration are presented in Figure 19. Note in Figure 18 that as the base of the gradient layer was approached, all radars disagreed. As upward penetration of the layer progressed, the tracks merged. Precisely at the top of the layer, VBG re-acquired, 52:52 (compare Figures 18 and 19 for this time), but then drifted into the same problem of short ranging that it had on the opposite side of the flight pattern (21:39:58 - 41:04). The aircraft again initiated a plunge through the gradient and came through the base of the gradient layer precisely at 54:20, when VBG came back strongly. The aircraft remained beneath the gradient layer to the end of the pattern, where an upward spiral was performed.

We see in this exercise that both azimuth and range appear to be affected more severely than previously thought by the presence of the inversion gradient layer. This assumes, of course, that one is willing to agree that two radar tracers nearly superposed, one on the other, recording a strong signal are indeed giving an accurate position in the lateral plane (with the exclusion of the 100 ft or so range error which is within our normally accepted tolerance). The inter-relation of these recorded events strongly suggests cause and effect, and gains a degree of authority for lack of alternate explanations.

Let us now look at the atmosphere in cross section along the average bearing from Vandenberg diagonally through the flight pattern from northeast to southwest. Using data from Figure 18 and several additional aircraft passes in this immediate vicinity, Figure 10 has been constructed. Data point density is sufficient for us to establish that the strong neck-like convergences of the gradient layer and its general wave shape are real. On several occasions (for example, the already presented June 8 case) our cross sections show that loss of lock has been coincident with these wave-induced convergences. In the example presently being discussed, the pattern flown was the second of two flown at the exact same point for the same radio hole, spread in time by 80 minutes. It appears that these anomalies can remain as standing wave-like phenomena for considerable time. Recall also the time variation presented in Figure 11 of the shift of wave nodes over Tranquillon Peak during a 45-minute interval. Apparently, at sea the waves are considerably more stationary, sharply defined, and of intense gradient; as opposed to the more diffuse topographically induced waves found over Tranquillon Peak.

Consider the cross-section revelation of bending effects. We have ray-traced

INVERSION LAYER PENETRATION

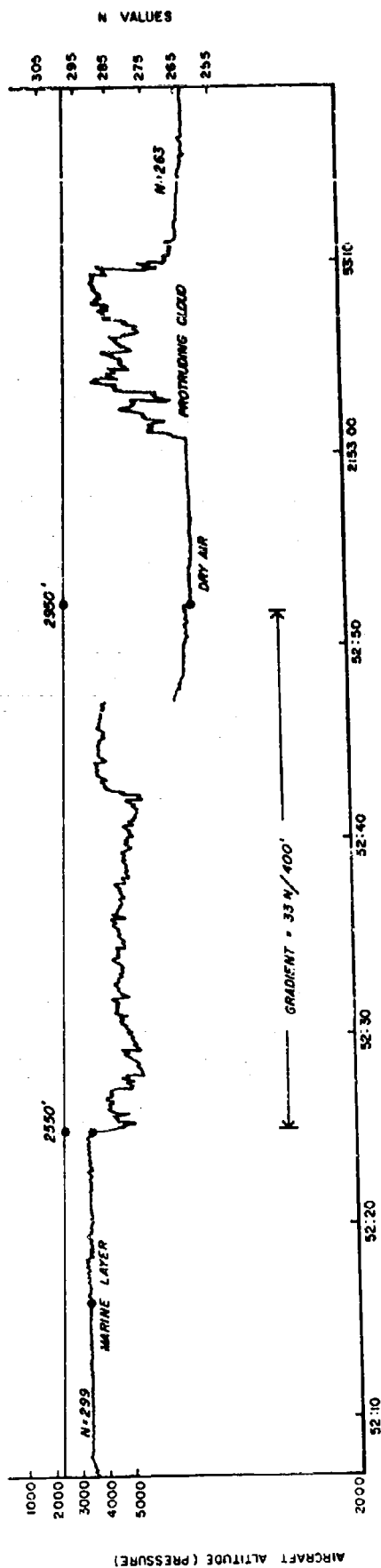


FIGURE 19

through the cross section of Figure 10 using the three possible data inputs which we have previously discussed, raobs, spirals, and cross sections. In this instance we have more precision than that obtained for our previous 8 June example. For this March 29 instance, there is excellent agreement between the aircraft position for loss of lock (41:04, Figure 18) and the antenna elevation at the time of signal loss. That is, agreement is good when the antenna elevation is corrected for refraction by cross-section inputs. Rays for balloon corrected and aircraft spiral corrected antenna elevations are shown for comparison. Again, the improvement of cross-section data inputs coupled with ray steering calculations defined the most accurate path to low-angle targets.

Mission Abort, or Missile Destruction Condition

According to Range Operations personnel, signal strength must be 3 db above noise for silo missiles to check-out before launch. Failure to obtain this minimum ratio is cause for mission abort. Moreover, failure of radars to agree on missile position immediately after launch is cause for destruction of the missile. Let us see how such negative situations can come about as direct effects of atmospheric anomalies. Recall Figure 7, which shows how the inversion layer can present severe trapping hazards for Tranquillon Peak radar. We have ray-traced through this section and find that the rays will trap below 50 mils, given these conditions. Moreover, it is possible for the main lobe of the propagation pattern to be trapped while the side lobe locks onto a missile coming up through the inversion from its silo. Assuming 0.8° minimum lobe separation, the altitude error is on the order of 1500 ft at 18 miles relative to the main lobe. For a distant radar operating under similar conditions, such as Point Pillar, tracking a Vandenberg Minuteman, the altitude disagreement between VBG and Point Pillar radars would be greatly increased. Point Pillar could experience inversion "lobe splitting" just as easily as Tranquillon Peak, with disagreement against Tranquillon Peak's missile altitude running around 6,000 ft. We have, therefore, all the ingredients needed to produce either a mission abort due to weak signal, or no signal; or a mission destruct due to confused radar after the missile has left the pad.

Summary

We have presented three radio-hole situations which have provided either direct confirmation or logical explanations of the following effect:

- 1) full cross sections employing steering corrections will produce greater accuracy for refraction correlations by a factor of 2, than corrections based on raob or aircraft spiral data sources;
- 2) azimuth variation appears to be more strongly affected by stratifi-

cation irregularities than previously believed;

3) severe bending, trapping, and lobe splitting due to variations of the inversion offer strong logic for explaining beacon fade, loss of signal, confused radar and consequent missile destruction.

CHAPTER V

EXPOSITION ON MATHEMATICS EMPLOYED IN REFRACTION ANOMALY INVESTIGATION

Sections I-IV have presented the results of field measurement analysis. In conjunction with the field program significant strides were made in the refinement of computational techniques. Starting with a review of REFRAC program (refraction correction, supplied by Western Test Range Engineering Department), consideration was given to simplification of correction techniques. This was dictated by needless complexities revealed in the review and by our own lack of an adequate computer to handle the storage.

Secondly, it was quickly learned that the simplification efforts led to the capability of real-time calculations and trapping warnings for low and negative angles.

Thirdly, one could no longer assume the atmosphere to possess horizontal homogeneity when dealing with low-angle tracking; nor could atmospheric variations be ignored on grounds that the effects are small; nor can we conveniently claim the required measurements are impossible to get. The real atmosphere demands that the irregularities be measured and accounted for. That is, signals do not systematically penetrate through a well organized medium, but must be steered through locally tilted surfaces, converging refraction gradients, and lensed, sandwiched, or washed out inversion structures. To serve this problem, a simple ray steering technique was developed, and this program along with considerations of the above issues is presented herein.

The aims of the present section are, therefore:

- 1) Review the REFRAC program supplied by the Western Test Range, and modify for present use.
- 2) Present real-time refraction correction and trapping warning techniques good for all angles.
- 3) Acknowledge the refraction complexity of the atmosphere and cope with its irregularities by ray steering techniques.

Review and Modification of REFRAC Program

The REFRAC program was reviewed and found mathematically correct, but overly complex. We were unable to reproduce trial runs. Modification was required to cure such problems as computational instability and to meet our

LIST OF SYMBOLS

- A : a variable in refraction program
- A. (DEN/2): a constant in real-time program
- AUX : an auxiliary variable in refraction program
- B : a variable in refraction program, also a constant in real-time program
- B_o : initial radar elevation angle, initial emergence angle, apparent target elevation angle
- B_i : emergence angle at ith level, angle of ray with the horizon
- β_o : true elevation of target as seen from radar
- c : speed of light in a refractive medium
- c_o : speed of light in vacuo
- C : a variable in refraction program, also a constant in real-time program
- Curv, $1/R_c$: instantaneous curvature of ray
- D : a variable in refraction program, also a constant in real-time program
- DEN : normalized decay parameter in dimensionless units in single exponential atmosphere model
- DI : an initial value in refraction program
- D_1, D_2 : normalized decay parameters in dimensionless units of quadratic exponential model atmosphere
- D_{1i}, D_{2i} : refraction parameters used in Gardner's (1964) REFRAC program
- Δ : prefix indicating increment
- Δh_i : change in height of target at ith level

ΔHD_i : slant range increment used in ray-steering program
 ΔN_i : N-unit change over fixed interval of .01 mers in ray-steering program
 $\Delta \tau_i$: bending increment at ith level
 $E, \exp(t_o^2 - t^2)$: a variable in refraction program, also a computational parameter in real-time program
 ϵ : elevation error
 γ : auxiliary angle between B_o and β_o used in Rowlandson's formulation
 δ : doppler radar error angle
 ϵ_1 : first iterated value of elevation error
 F : a variable in refraction program
 $F(x)$: a special refraction function in real-time program
 FI : an initial value in refraction program
 G : a variable in refraction program, also a computational parameter in real-time program
 h : elevation above sea surface
 h_i : elevation of ith level in stratified atmosphere, also elevation of ith point in ray-steering program
 h_o : radar elevation
 h_n : height of last point in ray-steering program
 $H, h/r_o$: elevation in normalized dimensionless units
 HD_i : range in mers of ith iteration point in ray-steering program
 HD_n : range in mers of last point in ray-steering program
 i : subindex for ith point
 $KI, 1 - \cos B_o$: an initial value used in refraction computations

$KB, 1-\cos B$: a variable used to compute emergence angle
 mer : distance subtended at earth's surface by a central angle of 1 mil
 $n, c/c_0$: index of refraction, also subindex for nth point
 n_i : index of refraction at the ith level
 $N, 10^{-6} \cdot (n-1)$: practical unit of index of refraction
 N_i : index of refraction, in practical units at ith level
 N_0 : index of refraction, in practical units, at radar elevation, also a refraction parameter in simple exponential atmosphere model
 \bar{N} : average index of refraction, in practical units, over a layer
 o : subindex indicating initial conditions
 r : radius vector from center of the earth
 r_i : radius vector to ith level
 r_0 : radius vector to radar site
 R : earth's radius
 $R_c, 1/\text{Curv}$: local radius of curvature of ray
 \bar{R}_{ci} : mean radius of curvature of ray in the ith layer
 RGERR: range error
 SE, $\sin(\text{THE})$: sine of angle subtended by radar range as seen from the center of the earth
 SR : radar electromagnetic range
 $S, SR/r_0$: radar electromagnetic range, normalized to dimensionless units
 SR_i : radar electromagnetic range of ith point
 $\text{SECA}, \sec(B_{i-1})$: secant of lower emergence angle of a computational layer
 $\text{SECI}, \sec(B_0)$: secant of initial radar elevation angle

SECB, $\sec(B_i)$: secant of upper emergency angle of a computational layer
 TANA, $\tan(B_{i-1})$: tangent of lower emergence angle of a computational layer
 TANI, $\tan(B_0)$: tangent of initial radar elevation angle
 TANB, $\tan(B_i)$: tangent of upper emergency angle of a computational layer
 TAU : total bending
 THE, θ^* : angle subtended by radar range as seen from the center of the earth
 TRGE: true range of target
 t_0 : an auxiliary constant in real-time refraction program
 t : an auxiliary variable in real-time refraction program
 τ : path bending angle
 v : a dummy variable
 V : shorthand for $1 - \cos(\tau)$
 W , $1 - \cos(\text{THE})$: an auxiliary variable in refraction program
 x : an auxiliary computational variable
 θ^* , THE: angle subtended by radar range as seen from the center of the earth
 z : a computational variable
 zz , $1/(1 - z^2)$: an auxiliary variable

own restraints of using a simple computer.

Review of Pertinent Refraction Correction Principles

Ray-tracing techniques are well developed and we need not repeat here any basic derivations. Essentially, all computing methods are based on the fact that a ray traveling in a refractive medium will bend so that its local curvature (defined as the reciprocal of the instantaneous radius of curvature R_c) is given by

$$\text{Curv} = 1/R_c = 1/n (dn/dR_c) \quad (1)$$

in which "n" is the local index of refraction. This is actually Snell's law in differential form. Differential equation (1) can be solved either formally or numerically as soon as a distribution for "n" is specified, since the radius of curvature is by definition normal to the trajectory.

The usual approach to the problem is to divide the atmosphere into a number of sufficiently thin slices so that the vertical gradient of "n" in each slice is sensibly constant. When this is done, equation (1) can be integrated formally if several further simplifying assumptions are made (Schulkin, 1952), (Weisbrod and Anderson, 1959), (Gardner, 1964).

Given a stratified atmosphere, it can be shown that the change in direction of the emergent ray between any two given elevations depends only on the initial and final indices of refraction (Bean and Dutton, 1966). This is expressed by the equation

$$n_i r_i \cos B_i = n_o \cdot r_o \cdot \cos B_o = \text{constant} \quad (2)$$

in which B_i is the emergence angle (the angle between the ray and the horizon) and r_i is the vector polar coordinate with origin at the center of the earth. Equation (2) is the finite form of Snell's law for an isotropic spherically stratified medium.

All solutions for the ray-tracing problem which are based on these premises differ only in the mathematical simplifications invoked. For instance, Schulkin's (ibid) solution for the local elementary bending of the ray for low angles of elevation between two slices is:

$$\Delta \tau_i = 2 \cdot (N_{i-1} - N_i) / (B_i + B_{i-1}) \cdot 10^{-6} \quad (3)$$

where N_i is the refractivity in "N" units,

$$N_i = (n_i - 1) \cdot 10^6 \quad (4)$$

while Weisbrod and Anderson (ibid) give theirs as

$$\Delta\tau_i = 2 \cdot (N_{i-1} - N_i) / (\tan B_i + \tan B_{i-1}) \cdot 10^{-6} \quad (5)$$

If sufficient slices are taken, and trigonometric subroutines are used, (3) will be faster in the computer than (5), while maintaining an accuracy compatible with the usually available inputs. Gardner's (ibid) solution, which uses the subtended earth's angle θ^* as the main parameter, turns out to be computationally equivalent to the Weisbrod and Anderson solution, as can be seen by the fact that Gardner's modified equation for the elementary trajectory length (Gardner, 1964, page 16)

$$SR_i - SR_{i-1} = \frac{c_o \cdot 10^{-6} \cdot N_i \cdot (H_i - H_{i-1}) \cdot (\sec B_i + \sec B_{i-1})}{c \cdot (\tan B_i + \tan B_{i-1})} \quad (6)$$

is equivalent to Weisbrod and Anderson's formulation

$$SR_i - SR_{i-1} = \bar{R}c_i \cdot \Delta\tau_i \quad (7)$$

which solves for the elementary arc length in terms of the local mean radius of curvature, $\bar{R}c_i$ and the local bending, since the mean radius of curvature $\bar{R}c_i$ is

$$\bar{R}c_i = \frac{c_o \cdot (H_i - H_{i-1}) \cdot (\sec B_i + \sec B_{i-1}) \cdot 10^6}{c \cdot 2 \cdot (N_i - N_{i-1})} \quad (8)$$

Introducing (8) and (5) into (7) actually reproduces (6).

Gardner's solution of the ray-tracing problem when a constant gradient is assumed for the refractive index between layers is unnecessarily complex computationally. For example, differences between small and very similar quantities are often programmed, as in his proposed equations (29) and (31), (Gardner, 1964)

$$SR_i - SR_{i-1} = \frac{c_o}{c} \cdot D_{2i} \cdot \cos B_o \cdot (\tan B_i - \tan B_{i-1})$$

$$\tan B = \frac{\cos \theta^* - r_o/r^*}{\sin \theta^*}$$

which although quite correct mathematically, can lead to computational instability at low angles of elevation due to cancellation of leading digits.

When using a high-speed computer to solve a problem it is generally best to

simplify the computational approach as much as possible to insure accuracy of calculation, even at the expense of increasing the number of slices and computational steps; the computer takes far longer in making logical decisions or in performing trigonometric or similar subroutines than in doing additions or multiplications. We have, therefore, strived to simplify the mathematical routines as much as possible and to avoid unnecessary storage, always checking the results against such standards as the precomputed tables for the CRPL reference atmospheres or Gardner's (ibid) computations to insure that consistency is maintained.

Modification of Ray Tracing for Simple Computers

Available computing methods were reviewed and modified to devise a simpler routine which would insure computational stability and minimum storage requirements. The programming was arranged to avoid as many trigonometric subroutines as possible. In the end we selected Weisbrod and Anderson's formulation (5) for the bending rather than Schulkin's (3), as it is possible to program the former without using many trigonometric subroutines so that it computes about as fast as Schulkin's while retaining the ability to work with high angles. Most trigonometric subroutines and large storage requirements can be avoided in the following manner:

The initial value $KI = (1 - \cos B_0)$ is computed accurately using a rational approximation designed specifically for it. Using the built-in computer trigonometric subroutine for the cosine function will lead to cancellation of leading digits at low angles of elevation

$$z = B_0 \cdot (0.0837984973 - 4.15747751/(B_0^2 - 9.98909688))$$

$$zz = 1/(1+z^2) \quad (9)$$

$$KI = 1 - \cos B_0 = 2 \cdot z^2 \cdot zz$$

The following initial constants are then stored for the starting level

$$\begin{aligned} SECI &= 1/zz/(1 - z^2) \\ TANI &= 2 \cdot z/(1 - z^2) \\ A &= 10^{-6} \cdot N_0 \\ C &= h_0/R \\ F &= A + C + A \cdot C \\ FI &= F \\ TANA &= TANI \end{aligned} \quad (9a)$$

$$TAU = 0$$

$$D = C$$

$$SR = 0$$

At the i th level ($i = 1, 2, \dots, n$), the following quantities are computed in succession to calculate the bending and the electromagnetic range

$$\begin{aligned} B &= 10^{-6} N_i \\ D &= h_i/R \\ E &= B + D + B \cdot D \\ G &= (E - FI)/(1 + E) \\ KB &= KI - G \cdot (1 - KI) \\ SECB &= 1/(1 - KB) \\ TANB &= KB \cdot (2 - KB)^{1/2} \cdot SECB \\ TAU &= TAU + 2 \cdot (A - B) / (TANA + TANB) \\ SR &= SR + B \cdot R \cdot (D - C) \cdot (SECA + SECB)/(TANA + TANB) \end{aligned} \tag{10}$$

$$\begin{aligned} TANA &= TANB \\ SECA &= SECB \\ A &= B \\ C &= D \\ F &= B \end{aligned} \tag{10a}$$

The total accumulated bending is TAU, and the last five statements are a reinitialization of conditions. We can now move to the next level and never have more than just a few constants in storage. The only subroutine needed is the square root. Since each successive KB is computed from the starting value KI, there is no build-up of rounding-off errors.

Following Gardner we now move to the $(i + 1)$ th layer and iterate these calculations until the calculated electromagnetic path exceeds the recorded one. The final i th level is then adjusted by a proportional interpolation (Gardner, 1964), so that the computed range coincides with the observed one. All the other parameters needed for the ray tracing can be derived from the total bending. We have used the subtended angle at the center of the earth "THE" as the parameter for the true range calculations, but obtained it from the bending rather than vice-versa as Gardner does. This angle is obtained from the relation

$$THE = (B_i - B_0) + TAU \tag{11}$$

Since the values of $\tan B_1$ and $\tan B_0$ are $\tan B_1$ and $\tan B_0$, it is preferable to compute directly the difference $B_1 - B_0$ rather than compute B_1 by an inverse trigonometric function subroutine, by noting that

$$x = \tan(B_1 - B_0) = \frac{\tan B_1 - \tan B_0}{1 + \tan B_1 \cdot \tan B_0} \quad (12)$$

Since at all practical radar ranges the angle $(B_1 - B_0)$ is small, we can then compute the inverse function $\arctan(x)$ by a local rational approximation designed specifically for small angles, which is faster than using the computer built-in inverse trigonometric function subroutine.

$$(B_1 - B_0) = x \cdot (6.36918871/(x^2 + 8.60141922 - 4.43698658/(x^2 + 1.9876921))) \quad (12a)$$

The true range is obtained next by solving the triangle with vertices at the center of the earth, at the radar site and at the intersection of the adjusted ith level with the ray. Since the angle subtended by the total trajectory, as viewed from the center of the earth, is small for all practical radar ranges, we found it preferable to obtain the value $W = 1 - \cos(\text{THE})$ using

$$W = \text{THE}^2 \cdot (-0.745585589 + 37.235360/(29.8938597 + \text{THE}^2)) \quad (13)$$

and then obtain the true range from

$$\text{TRGE} = R \cdot ((D - DI)^2 + 2 \cdot D \cdot DI \cdot W)^{1/2} \quad (14)$$

which avoids computational instability due to loss of leading digits. The range error is then given by the difference

$$\text{RGERR} = \text{TRGE} - \text{SR} \quad (15)$$

where we have followed the usual mathematical convention to define the error as the difference between the true value and the approximation rather than vice-versa. An error is the amount to be added (algebraically) to an observation to bring it up to its true value.

Finally, the elevation error " ϵ " is computed as follows

$$\begin{aligned} Z &= \tau \cdot (0.0837984973 - 4.15747751/(\tau^2 - 998909688)) \\ V &= 2 \cdot z/(1 + z^2) \\ \text{AUX} &= (D - DI)/(1 + D) \\ \text{SE} &= 2 \cdot z/(1 + z^2) \\ x &= (V - \text{SE} \cdot \tan B - \text{AUX})/(\text{SE} + \tan B_1 \cdot (1 - \text{AUX}) - \tan B_0 \cdot (1 - V)) \\ \epsilon &= x \cdot (0.443525198 + 9.28995955/(x^2 + 16.6943041)) \end{aligned} \quad (16)$$

The various approximations used are valid to at least 7 decimals for B_0 .

of the program is the range - as being a 300 miles. In actual comparisons we repeatedly found that we could reproduce Gardner's error computations to five significant figures. Although the main purpose was to speed-up computations for low angles of elevation, logical decisions were included to handle high angles also.

The program was completed with the addition of safeguards to warn of potential or actual trapping layers. In the latter case, the program is capable of following the trapped ray back to earth and, assuming a specular reflection, to follow the ray for as many reflections as desired. If one or more potential trapping layers are implicit in the inputs, the largest angle of penetration is computed and printed at the end of each run. The program accepts positive, negative or zero elevation angles of any magnitude. If the input is a negative elevation angle, the antenna elevation angle and range of the radio horizon are also automatically computed and printed. If the input elevation angle is smaller than the radio horizon antenna elevation, a specular reflection is assumed where the ray hits the earth and the bounced ray is followed through. A modification of the computations is necessary in this case since formula (11) no longer holds. Since a target can be reached by either a direct or a close-by ground-reflected ray at low elevations, a fact which causes no small amount of trouble in the hunting mechanism of the radar at low elevations, the ability to analyze both cases is significant. In spite of the relative program sophistication, only 41 computing statements involving about 77 multiplications and divisions, 60 additions or subtractions, 2 square root routines, and 11 logical decisions per layer are needed for the non-trapped ray. Although the present program, written in TELCOMP language, serves well the purposes of the present investigation, a modest additional effort produces real-time corrections with an accuracy compatible with the assumptions inherent in stratification.

Real-Time Corrections for Low-Angles of Elevation

We have seen that present reduction methods share in common the assumption of a stratified atmosphere in which the index of refraction varies linearly with height within selected layers. When the layers are not too far apart, this is a fair assumption, but the need for many reference layers, which require separate individual computations, greatly increases the execution time. One alternative is to precompute and to store the results of several key profiles and to interpolate for the corrections, but this requires a large storage capacity.

Refractivity profiles generally decay exponentially with height when one looks over fairly thick layers, so it is obvious that the thickness of the reference layers could be increased considerably if suitable decay constants were available. Freeman (1964), following the lead of Thayer (1961), has shown how acceptable approximations can be made to yield a closed-form solution for the

corrections are greatest at the low angles of elevation which are of primary interest in this report, and since the approximations invoked by Freeman are critical in this area, we have revised Freeman's derivation keeping second-order terms in order to investigate the possibility of improving his solution.

Since corrections are greatest at the low angles of elevation which are of primary interest in this report, and since the approximations invoked by Freeman are critical in this area, we have revised Freeman's derivation keeping second-order terms in order to investigate the possibility of improving his solution.

Correction Derived From Using the Curved Radar Path Instead of the Geometric Slant Range

Consider a bent path between two points A and B (Fig. 20) for which the total bending is τ . The radius of curvature changes continuously from A to B but we can obtain a good estimate of the error involved in substituting the curved path \overline{AB} by the chord \overline{AB} , by assuming an average radius of curvature \bar{R} between A and B will cut the segment \overline{AB} at an angle $\tau/2$. The relative error committed in substituting this arc by the chord is

$$\text{Rel err} = \frac{\text{arc} - \text{chord}}{\text{arc}} = 1 - \frac{\sin(\tau/2)}{(\tau/2)} \approx \tau^2/24 \cdot (1 - \tau^2/80, \dots) \quad (17)$$

The angle τ is generally less than 20 mils or so, so the error introduced by this substitution is generally less than one fifty thousandth of the range. A total bending of nearly 25 degrees or 430 mils would be needed to introduce a one percent range error. Bendings of this magnitude occur only under circumstances approaching the limits of the assumptions invoked for ray-tracing. We should, of course, add this correction, especially when dealing with long ranges and bendings.

Target Elevation

In what follows we will consider all distances normalized to dimensionless units by expressing them in terms of the length of the radius vector r_o from the center of the earth to the radar site. This makes it easier to keep track of the order of magnitude of the various terms involved and simplifies computations. The radius vector to the radar site is

$$r_o = R + \Delta h_o \quad (18)$$

where R is the radius of the earth (in arbitrary units) and Δh_o is the elevation of the radar site above the earth's surface in the same units. The normalized radar range S is then

$$S = SR/r_o \quad (19)$$

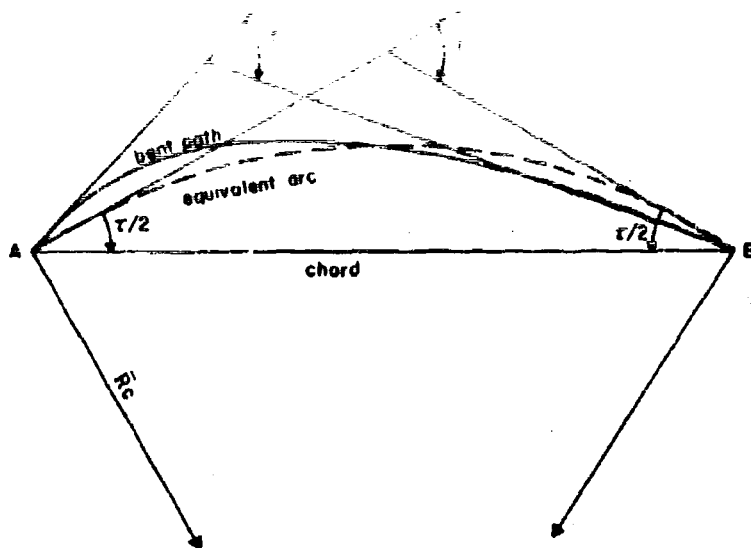


Figure 20. Geometry of curvature correction

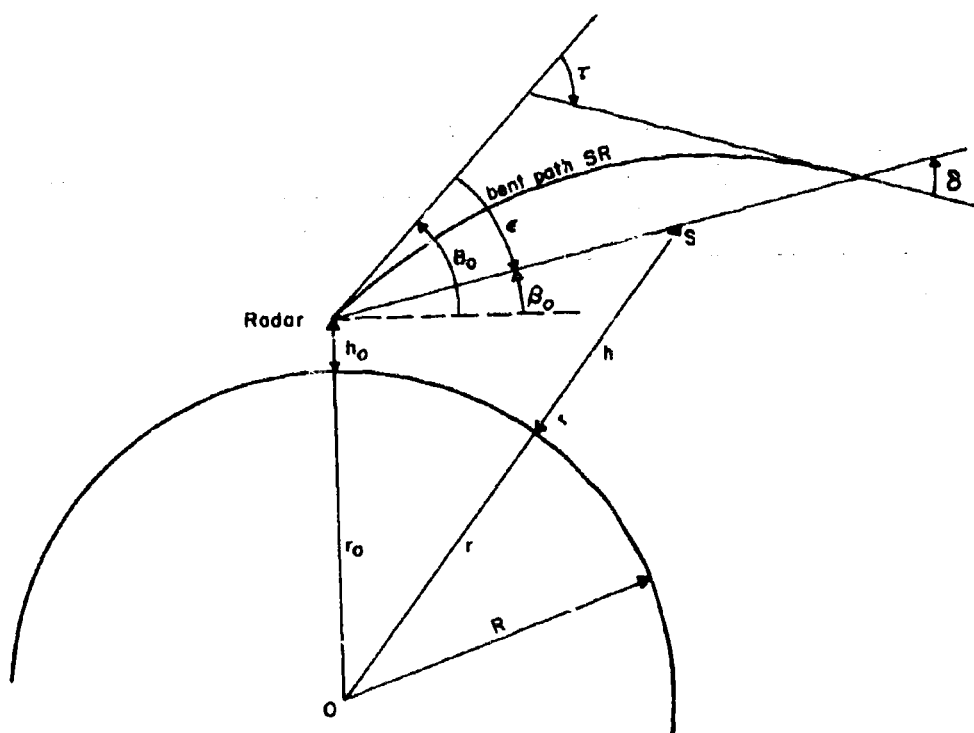


Figure 21. Ray geometry

and the local target elevation H above the reference surface at the radar is

$$H = \Delta h / r_o \quad (20)$$

If β_o is the true target elevation angle along the geometric path SR, and B_o the actual radar elevation angle, we can obtain from triangle OSR in Figure 21 the normalized target elevation

$$H = (1 + S^2 + 2 \cdot S \cdot \sin \beta_o)^{1/2} - 1 \quad (21)$$

Bending Error

An exponential profile is next assumed, with a reference surface refractive index N_o (in "N" units) and a decay constant DEN so that the refractive index at the normalized height H above the reference surface is given by

$$N = N_o \cdot \exp(-\text{DEN} \cdot H) \quad (22)$$

We must note that the decay constant must also be expressed in terms of the radius vector r_o .

If the atmosphere is stratified, the ray will obey Snell's law in spherical coordinates (2) and in normalized units the emergence angle B at elevation will satisfy the relation

$$\cos B = n_o \cdot \cos B_o / (n \cdot (1 + H)) \quad (23)$$

in which

$$\begin{aligned} n_o &= 1 + 10^{-6} \cdot N_o \\ n &= 1 + 10^{-6} \cdot N \end{aligned} \quad (24)$$

substituting (22) and (24) into (23) yields

$$\cos B = \frac{(1 + 10^{-6} \cdot N_o) \cdot \cos B_o}{(1 + 10^{-6} \cdot N_o \cdot \exp(-\text{DEN} \cdot H)) \cdot (1 + H)} \quad (25)$$

We will next assume that the normalized range is of the order 10^{-1} or smaller. Expanding (21) to a second order approximation

$$H \approx 1/2 \cdot [(S \cdot \cos \beta_o + \tan \beta_o)^2 - \tan^2 \beta_o] \quad (26)$$

Furthermore, the quantity $10^{-6} \cdot N_o \cdot \exp(-\text{DEN} \cdot H)$ in the denominator of (25) never exceeds $5 \cdot 10^{-4}$, so it is always three orders of magnitude

smaller than unity. In addition, from (26) we have

$$H/S \approx (\sin \beta_0 + S/2 \cdot \cos^2 \beta_0, \dots) \quad (27)$$

which indicates that for small angles of elevation, it is at least one order of magnitude smaller than S within the assumptions made. We can, therefore, to at least a second order of approximation, rewrite (25)

$$\cos B \approx (1 + 10^{-6} \cdot N_0 \cdot (1 - \exp(-\text{DEN} \cdot H) - H)) \cdot \cos \beta_0 \quad (28)$$

The elementary bending at any point of the path is given by

$$d\tau = (1/n) \cdot (dn/dH) \cdot \cos B \cdot dS \quad (29)$$

Taking derivatives in (22) and combining with (24) and (28) we get

$$d\tau \approx -10^{-6} \cdot N_0 \cdot \text{DEN} \cdot \cos \beta_0 \cdot [1 + 10^{-6} \cdot N_0 \cdot (1 - 2 \cdot \exp(-\text{DEN} \cdot H) - H) \cdot \exp(-\text{DEN} \cdot H)] \cdot dS \quad (30)$$

We will now introduce a new variable to simplify the handling of the various terms. Let

$$\begin{aligned} A &= (\text{DEN}/2)^{1/2} \\ t_0 &= A \tan \beta_0 \\ t &= t_0 + A \cdot S \cdot \cos \beta_0 \end{aligned} \quad (31)$$

Then, (26) can be written

$$H \approx (t^2 - t_0^2)/2A^2 \quad (32)$$

and hence

$$dS = dt / (A \cdot \cos \beta_0) \quad (33)$$

so equation (30) becomes

$$d\tau \approx -2 \cdot 10^{-6} \cdot N_0 \cdot \cos \beta_0 \cdot \sec \beta_0 \cdot [1 + 10^{-6} \cdot N_0 \cdot (1 - 2 \cdot \exp(t_0^2 - t^2) + (t_0^2 - t^2)/2A^2) \cdot \exp(t_0^2 - t^2)] \cdot dt \quad (34)$$

which can be integrated formally to yield

$$\tau = B \cdot (F(t_0) - E \cdot F(t)) + D \cdot (t_0 - E \cdot t) + C \cdot (F(\sqrt{2}t_0) - E^2 \cdot F(\sqrt{2}t)) \quad (35)$$

in which $F(x)$ stands for the function

$$F(x) = 2 \cdot \exp(x^2) \cdot \int_x^\infty \exp(-v^2) \cdot dv \quad (35)$$

The function $F(x)$ varies smoothly from $\sqrt{\pi}$ to zero when the argument x varies from zero to an infinitely large value, and admits a simple and accurate rational approximation. When second order terms are retained in (35) the constants are

$$\begin{aligned} B &= 10^{-6} \cdot N_0 \cdot A \cdot (1 + 10^{-6} \cdot N_0 + (2t_0^2 - 1)/4A^2) \\ C &= 2 \cdot 10^{-12} \cdot N_0^2 \cdot A \\ D &= 10^{-6} \cdot N_0 / 2A \\ E &= \exp(t_0^2 - t^2) \end{aligned} \quad (37)$$

$$F(x) = 1.00129 / (x + .039262 + .1856633 / (x - 9.024780 + 115.2736 / (x + 12.29742)))$$

The rational approximation developed for $F(x)$ is accurate to about five decimals for all ranges of x . All of these expressions can be computed very fast even on a small computer.

An analysis was then made of the extreme possible values of all the constants in (37). The two correcting terms which multiply constants C and D turned out to be at least one order of magnitude smaller than the first term.

In view of other uncertainties, it was decided to drop these correcting terms altogether, simplifying further the computations. A similar order-of-magnitude analysis indicated that both $(2t_0^2 - 1)/4A^2$ and $10^{-6} \cdot N_0$ are always at least one and three orders of magnitude smaller than unity respectively, when the assumption is made that the order of S is 10^{-1} . Therefore, we also dropped these terms from the parenthesis, with the final result

$$\tau = 10^{-6} \cdot N_0 \cdot A \cdot (F(t_0) - E \cdot F(t)) \quad (38)$$

which is basically similar to Rowlandson's (ibid) formulation for moderate to long ranges, but which remains accurate at short ranges. This analysis also shows that it is not practical to improve further on Freeman's approach by keeping second-order terms.

A Real-Time Iterative Solution for the Bending

Equation (38) still suffers from the disadvantage of Freeman's original

It is the author's opinion that the use of approximation (26) is not very accurate, especially at longer ranges and for larger values of the bending parameter N_0 . The true elevation β_0 can also be obtained by an iterative procedure starting from the known radar elevation angle B_0 . A complete solution for β_0 , however, is neither necessary nor desirable. As already pointed out by Freeman (ibid) in his original paper, using the radar elevation angle B_0 in place of β_0 tends to underestimate τ because the computing line of sight tends to be above the real path. Using the true value of β_0 , while improving the approximation, tends to overestimate the bending as the slant path now lies below the true path. We should also point out here that another and even larger source of error comes from the use of approximation (26) at the longer ranges. The real elevation error $\epsilon = \beta_0 - B_0$ and the true bending τ are related by the expression

$$\epsilon = - \arctan \left\{ \frac{\cos \tau + \sin \tau \cdot \tan B - n/n_0}{n/n_0 \cdot \tan B_0 + \sin \tau - \cos \tau \cdot \tan B} \right\} \quad (39)$$

Since τ is always a small angle, if we make the customary small-angle approximations and keep up to second-order terms, using (24), (22), (32) and (37)

$$\epsilon \approx \frac{\tau^2/2 - \tau \cdot \tan B - 10^{-6} \cdot N_0 \cdot (1 - E)}{\tau + \tan B_0 - \tan B} \quad (40)$$

Further, Weisbrod and Anderson (1959) have shown that over short ranges

$$\tau \approx \frac{-2 \cdot (N_0 - N) \cdot 10^{-6} \approx -10^{-6} \cdot N_0 \cdot (1 - E)}{\tan B + \tan B_0 - \tan B} \quad (41)$$

so for short ranges the numerator of (40) reduces to $\tau^2/2$. At the same time, $(\tan B_0 - \tan B) \ll \tau$, so the denominator of (40) tends to τ .

$$\epsilon \longrightarrow \tau/2 \text{ (short ranges)} \quad (42)$$

and this approximation will undercorrect longer ranges, since as the range increases indefinitely, $\tan B$ increases without bounds and from (40)

$$\epsilon \longrightarrow \tau \text{ (long ranges)} \quad (43)$$

If we apply correction (42) to the initial elevation angle B_0 only once, there will be a tendency for compensation at long ranges since (42) undercompensates at long ranges which is exactly what we need.

This compensation mechanism indeed works, so the final programming was made by setting $\beta_0 = B_0$ initially and computing an approximate bending τ_1 by using (38). The initial elevation guess is corrected by adding half the approximate bending $\tau_1/2$ and the final bending τ is computed using (38) again.

The computer requirements are very small and the only subroutine involved is the computation of the single exponential E in (37). Once the total bending τ is available, all the other parameters can be extracted from it. Accordingly, Appendix A contains the calculations for Range Error, Elevation Error, and Doppler Velocity Error Angle. There also appear suggestions for quadratic exponential atmospheres, and for a possible use of the radar beam as an atmospheric probe. We regard this as "spillout" from the present work.

Comparisons of Refraction Corrections at Low Angles of Elevation Using the Proposed Real-Time Computations with Those Obtained by Standard Solutions

Tables 8 and 9 present a comparison between the exact solutions for the refraction corrections at low angles of elevation for a standard CRPL reference atmosphere and those developed in this report. For shortness, we refer to the exact and the iteration results.

Tables 8 and 9 illustrate the remarkably good fit between the iteration and the exact solutions. The data is presented in tabular form because it would not have been practical to present it in graphical form, as the two lines would have plotted one on top of the other in most cases. The fit is particularly good at medium and short ranges, an area where Rowlandson's (1968) simplifications start losing validity. The largest absolute error in range error stays under 2 meters in the worst case, which is smaller than the size of most targets. Even at zero elevation, the bending and elevation error discrepancies do not exceed .2 mil, which are smaller than differences that occur due to uncertainties in our knowledge of the state of the atmosphere. This is especially impressive if we realize that the iteration technique is perfectly general and uses no "ad hoc" parameters to improve the fit.

It must be pointed out, however, that these comparisons were made with a well-behaved model, and that greater differences may be expected with a real atmosphere, a point which will be taken up later when the discussion of the determination of the decay constants is considered. A most important fact is that only about 107 multiplications and divisions, 70 additions and subtractions, 2 exponential subroutines, 2 square roots and 3 logical decisions are needed for a complete solution of all refraction errors, which makes the procedure near real-time even on the smallest computer. The algorithm is much faster than Rowlandson's as there is no need to integrate

TABLE 8

Comparison between exact range and total bending errors for a standard CRPlatmosphere for different ranges and radar elevation angles, and the values obtained by the iteration real-time technique.

Legend: E = exact value of error

I = error computed using the iteration technique

B_0 = initial radar elevation angle

B_0 = (Mils)/Rg(km)		RANGE ERROR(meters)					TOTAL BENDING(mils)				
		10	50	100	200	600	10	50	100	200	600
0	E	3.4	17.1	33.6	62.9	110.1	.5	2.7	5.3	9.7	16.0
	I	3.4	17.1	33.9	64.0	110.4	.5	2.7	5.3	9.9	16.3
2	E	3.4	17.0	33.1	61.0	103.7	.5	2.7	5.2	9.4	15.0
	I	3.4	17.0	33.3	62.1	102.5	.5	2.7	5.2	9.6	15.3
5	E	3.4	16.8	32.4	58.3	94.4	.5	2.7	5.1	9.0	13.8
	I	3.4	16.8	32.6	59.2	94.0	.5	2.6	5.1	9.2	14.0
10	E	3.4	16.5	31.1	54.3	81.6	.5	2.6	4.9	8.4	12.0
	I	3.4	16.5	31.3	54.9	81.3	.5	2.6	4.9	8.5	12.2
20	E	3.4	16.1	29.1	47.4	64.5	.5	2.5	4.5	7.3	9.5
	I	3.4	15.9	29.1	47.6	63.8	.5	2.5	4.5	7.4	9.6
50	E	3.3	14.2	23.6	33.1	37.7	.5	2.2	3.7	5.1	5.6
	I	3.3	14.2	23.5	32.6	36.7	.5	2.2	3.7	5.1	5.6
100	E	3.2	11.9	17.3	21.1	21.2	.5	1.9	2.7	3.1	3.2
	I	3.2	11.9	17.2	20.2	20.8	.5	1.9	2.7	3.1	3.2
200	E	3.0	8.7	10.9	12.0	13.6	.5	1.3	1.6	1.7	1.7
	I	3.0	8.7	10.5	10.8	11.0	.5	1.3	1.6	1.7	1.7

TABLE 9

Comparison between elevation and Doppler velocity angle error for a standard CRPLatmosphere for different ranges and radar elevation angles, and the values obtained by the iteration real-time technique

Legend: E = exact value of error

I = error computed using the iteration technique

B_0 = initial radar elevation angle

		ELEVATION ERROR (mils)					DOPPLER ERROR (mils)				
B_0	R_g										
	(Miles)(km)	10	50	100	200	600	10	50	100	200	600
0	E	.3	1.3	2.7	5.1	11.1	.3	1.3	2.6	4.6	4.9
	I	.3	1.3	2.7	5.1	11.3	.3	1.3	2.6	4.8	5.0
2	E	.3	1.3	2.6	5.0	10.6	.3	1.3	2.5	4.4	4.5
	I	.3	1.3	2.6	5.0	10.8	.3	1.3	2.6	4.6	4.5
5	E	.3	1.3	2.6	4.9	9.9	.3	1.3	2.4	4.2	3.9
	I	.3	1.3	2.6	4.9	10.0	.3	1.3	2.5	4.3	3.9
10	E	.3	1.3	2.5	4.6	8.9	.3	1.3	2.3	3.8	3.1
	I	.3	1.3	2.5	4.6	9.0	.3	1.3	2.4	3.9	3.1
20	E	.3	1.3	2.4	4.2	7.4	.3	1.2	2.1	3.1	2.1
	I	.3	1.3	2.4	4.2	7.5	.3	1.2	2.1	3.1	2.1
50	E	.3	1.2	2.1	3.3	4.7	.3	1.0	1.6	1.8	.9
	I	.3	1.2	2.1	3.3	4.8	.3	1.0	1.6	1.8	.8
100	E	.3	1.0	1.7	2.3	2.9	.2	.8	1.0	.8	.3
	I	.3	1.0	1.7	2.3	2.9	.2	.8	1.0	.8	.3
200	E	.2	.8	1.2	1.4	1.6	.2	.5	.5	.3	.1
	I	.2	.9	1.2	1.4	1.6	.2	.5	.4	.3	.1

numerically for the elevation error.

The Anisotropic Atmosphere - A Ray-Steering Program

The detailed refractometer cross sections available in this project have shown that the assumption of stratification is valid only as a first-order approximation. Isopleths of refractive index (refractopleths) are generally tilted with respect to the earth's geopotential surfaces and the gradients are far from isotropic in the horizontal. These departures exert their greatest influences at low angles of incidence for the propagated rays which are of interest in this report.

In trying to follow a ray through an anisotropic medium, we are confronted with two practical problems. The first one is the description of the medium itself since we now have to specify the three-dimensional distribution of the refractive index, and the data handling problem becomes formidable. The second one is that the integration of the ray equations has to be accomplished by some sort of numerical integration scheme, since an analytical description of the complex refractopleth patterns is a very difficult task. Initially, we considered a simplified scheme to describe the observed patterns by using orthogonal polynomials, following the lead of Wadsworth (1951) who had some success in doing the same with pressure patterns. The objective in mind was to relieve the storage problem in the computer. In common with what was found by Lopez and Nason (1967) in a modelling study of precipitation patterns, which resemble refractopleths a great deal, this approach did not prove practical.

A description of the patterns by gridpoints is the next approach, and would have been the one used except that difficulties in procuring an adequate computer limited severely the storage capacity available. The logical compromise was to use the human brain, wherein a hybrid graphical-computational approach was used in the exploration work. Two independent analyses were performed on the same data to identify human error in pattern display.

All distances were normalized in terms of the radius of the earth, and a practical unit, the "mer" (for milli-earth-radius), equal to the distance subtended by one mil angle at the earth's surface was introduced to simplify the computations. A simple piecewise integration scheme using a variable horizontal step unit was next devised to compute the terminal elevation of the ray at the end of each step. The details of the procedure are given in the next paragraph.

As long as the data has to be plotted in cross-section form to check its validity in exploration work, this hybrid procedure is perfectly satisfactory. It is very easy to computerize the whole operation by describing the patterns by means of grid points, storing them in the computer and letting the computer

do the differencing and interpolation.

It is then possible to envision a workable system in which two airplanes are stacked one above the other, one porpoising through the lower atmosphere and the other around the inversion, both telemetering the data in real-time to a computing center which would process and store it in readiness for tracing any selected ray. A total time of some 45 minutes should be needed to run a given cross section, and since horizontal differences are less marked than vertical ones, a triangular run between the various radar centers should define the horizontal changes in a practical manner.

Computations for Ray Steering

Computations for the ray tracings were carried out by a piece-wise integration of equation (1) as follows. An arbitrary interval ΔHD_i in mers was selected at the i th point, so that if the ray were extrapolated by this much, the vertical gradient remained sensibly constant. It was then assumed that 1) the difference between the i th ray segment and its horizontal projection was a second order quantity. This assumption is quite tenable for rays up to at least 100 mils elevation; 2) the ray can be approximated by an arc of circle whose curvature equals the average curvature of the segment.

The curvature at any point in the segment equals the local logarithmic derivative of the refractive index $(1/n) \cdot (dn/dR_c)$, where R_c is the local radius of curvature. If we substitute the averaged derivative over the segment by the corresponding finite difference equivalent, noting that the factor $(1/n)$ differs from unity by at most a third-order quantity and that $n = 1 + 10^{-6} N$, we obtain the expression $\Delta \bar{N} \cdot 10^{-6} / \Delta R_c$ for the average curvature. Refractive indices are available only in the form of cross-sections with limited data, so a compromise is needed for the selection of the radius of curvature increment ΔR_c . If we make it small to approximate the local derivatives we will have uncertainties in the determination of the averaged refractive index change $\Delta \bar{N}$. If we make it too large, we will smooth out many real irregularities. In the end, a value of $\Delta R_c = .01$ mers (about 67 meters) was chosen as the best compromise. For this fixed value of ΔR_c , the average curvature for the segment ΔHD is $10^{-4} \cdot \Delta \bar{N}$ and the average local bending will be $\Delta \tau = \Delta \bar{N} \cdot \Delta HD / 10$ (mils).

The net change in elevation from the extrapolated position then follows immediately since it equals the difference in elevation due to the opposing effects of the earth's and the ray's curvature. Since both trajectories are assumed circular, the computations are greatly simplified. The angle of emergence follows from relation (11) between the bending and accumulated horizontal distance.

The scheme of the computations for the i th point is as follows: (All distances

are in mers and angles in mils)

$$\begin{aligned}
 \Delta\tau_i &= \Delta N_i / 10 \\
 \Delta h_i &= (2 \cdot B_{i-1} + \Delta HD_i - \Delta\tau_i) \cdot \Delta HD_i / 2 \\
 h_i &= h_{i-1} + \Delta h_i \\
 B_i &= B_{i-1} + \Delta HD_i - \Delta\tau_i \\
 HD_i &= HD_{i-1} + \Delta HD_i \\
 \tau_i &= \tau_{i-1} + \Delta\tau_i
 \end{aligned} \tag{44}$$

Computations are iterated until the nth and last point, and then the refraction corrections are obtained from

$$\begin{aligned}
 RGERR &= 10^{-6} \cdot \sum_{i=0}^{i=n} \Delta HD_i \cdot N_i \quad (\text{mers}) \\
 \tau &= HD_n + B_o - B_n \quad (\text{mils}) \\
 \epsilon &= B_o + HD_n / 2 - 10^3 \cdot h_n / HD_n \quad (\text{mils})
 \end{aligned} \tag{45}$$

The range error "RGEER" can be changed to more conventional units by using the equivalences 1 mer \approx 6370 m \approx 20900 ft. As a check, the value obtained for the total bending from (45) must coincide with the value of τ_n in (44).

The computations involved in (44) are extremely simple, and by exercising judgement over the selected intervals, we found that rays could be traced very rapidly with as few as a dozen key points along the trajectory. We have checked the approximations involved in (44) by repeating the calculations using shorter intervals and more accurate formula, and found that as long as the initial elevation is under 100 mils there is no need for greater sophistication. Currently available inputs just do not justify the use of greater computing effort.

SECTION VI

SUMMARY AND RECOMMENDATIONS

Summary

With prevailing northwest wind, the inversion immediately to the south of Tranquillon Peak is likely to be destroyed by the hydraulic-jump effect associated with sufficiently high Froude numbers. This will often be noticed as an erosion of the cloud deck at inversion height. This circumstance should allow excellent target tracking. The well-mixed atmosphere here will approximate a standard atmosphere. The mixed condition should exist some 20 miles to seaward.

Generally, the area immediately to the west of Tranquillon Peak will have low-level mixing due to eddying around the land mass, in which case one will find a clear sky area along the beach where the mixing has eroded the cloud deck (present at inversion height). At higher altitude one will find a set of standing waves from the disturbance of the peak itself.

In the northerly sections wave trains across Santa Inez Valley can be expected. The inversion may also have a warped geometry which seemingly climbs upward to meet Tranquillon Peak. This warping can actually be seen by a ground observer on the north hills when the low morning sun scatters off the haze layer. The trapping and bending significance of a warped or tilted inversion layer has been brought out in the section on radio hole missions.

There will be a slight elevation difference in the inversion between the north and south sides of San Nicholas Island. The gradient layer will bulge over the island on the order of 1,000 ft. It will have a V-wake structure propagating out to the north and south sides of the island. It will have a large standing wave off the windward nose of the island. There is strong convergence of the gradient layer eastward of the mid point of the island and a hydraulic jump induced mixing of the inversion layer downwind of this, producing a well mixed wake off the eastern end of the island.

The inversion at Point Mugu may be washed out from eddy mixing associated with shear where the sea breeze front meets the north westerlies. It can also be multi layered or lensed under moderately weak stability conditions (to be seen in Figure 16, Section IV, 8 June example). The seaward strength of the inversion may be experienced close along shore and over the station at Point Mugu when strong stability conditions are present.

The statistics of refractive index corrections so far accumulated suggest that corrections increase from shore to seaward as a function of increasing sharpness

in the gradient layer. Fully measured cross sections for which ray steering models are employed produce greater corrections than those produced from Raob or aircraft spiral data employing "stratified atmosphere" models. The average separation of relative error between the extremes of data and formulae employed in a comparison of refractive corrections between Raobs, spirals, and cross sections is 68 percent over six cases analyzed in detail. The greatest differences are found in the elevation errors.

Investigation of the relation between the altitude position of a C-band beacon equipped aircraft and its indicated radar position when loss of lock is experienced shows that the actual position of signal loss is much better defined if a full cross section and steering techniques are used to correct the radar for refraction.

Signal loss is associated with atmospheric wave nodes and sharply converging refractopleths in the gradient layer. This accounts for crossing over of antenna angles in the vertical plane. This is reflected in the radar's hunting in the vertical plane at very low angles (< 10 mils). This does not preclude that hunting may also be a function of the usually alleged multipath (which in these circumstances is almost synonymous).

The atmospheric waves found at sea at the inversion interface may dwell for considerable time in one place (80 min.). Where associated with the Tranquillon Peak topographically induced waves the node positions of the waves may shift in the lateral plane, but wave size and geometry remains the same (45 min. comparisons).

Examination of REFRAC correction program supplied by Western Test Range reveals that the program is mathematically correct but overly complex. Its inability to produce a satisfactory run forced a redesign of the program which now contains only 41 computing statements; involving 77 multiplications and divisions, 60 additions and subtractions, 2 square root routines, and 11 logical decisions per layer. This is the sole requirement for the real time correction of a non-trapped ray. The program has run on a TELCOMP system serviced by a PDP-7 computer. The program serves any elevation angle, including negative angles and warns of impending trapping conditions.

The problem of steering rays through an anisotropic atmosphere is described and formulae presented for appropriate ray tracing where strong irregularities exist along the sighting line.

Recommendations

If accuracy and reliability demands on the trilateration system at Western Test Range become no greater than they presently are, do nothing except learn more about the hazards of side lobe splitting as a function of the inversion layer.

This can, and may have caused at least one missile destruction in the past. Use a mid-path reflector (an alternative steeper angle path) for checking beacon fade on the pre-launch Minuteman checks when inversion interference is suspected.

If accuracy and reliability demands on the trilateration system at Western Test Range are likely to become greater in the near future, then

- 1) Confirm the inversion effects brought to light in this investigation.
- 2) Introduce meteorological forecasts of the condition of the inversion before shot time (see Appendix B).
- 3) Forget about the tiny differences in the various correction formulae and devise better techniques for coping with the very real differences in atmospheric data inputs.
- 4) Go to real-time refraction corrections with built-in trapping warnings.
- 5) Focus attention on procuring full cross sections, starting 30-40 minutes before shot time.

We propose for pre-launch cross sections that

- 1) Two aircraft begin exploration of the inversion at sea, at $t-90$ ($t = 0$ = shot time) where low-angle rays will intercept the gradient layer (depends on the height of the layer). The aircraft will establish layer height, gradient, and geometrical irregularity.
- 2) At $t-35$ one aircraft begins to map a cross section for the first 15 miles in front of the radar, from the top of the inversion to the surface. The second maps the precomputed interception zone (where the rays will pass through the inversion).
- 3) During the entire pre-shot mission, both aircraft telemeter their data directly to the beach in real time. The cross sections are constructed in computer memory. Prior to the $t-35$ mappings, preliminary ray tracings are made to help identify regions for concentration of mapping effort during the next 30 minutes. At $t-5$ the mapping aircraft are diverted off the intended trajectory. Between $t-5$ and $t = 0$ the cross sections are ray-traced again for possible danger points. At $t = 0$ the cross sections are used for real-time refraction corrections to missile trajectory.

Appropriate Exploratory Work

It has been learned that radar targets have been placed on Santa Cruz Island

for calibration in the past (Bankston, 1964). Such could also be useful at San Nicolas Island or at sea with a balloon and spar buoy combination. Where greater height is required, tethered balloons monitored for position by cine theodolites should be considered. These fixed targets would then be used as absolute reference while more is learned about mapping of cross sections, management of aircraft, and instrumentation and telemetry, and ray tracing for error prediction. We further propose a system be investigated wherein a backward solution of the refraction equations is performed so that adjusting parameters are computed from the cross-section data. This approach has developed as unexpected spill-out from the present project. We have devised a preliminary method for performing the mathematics of this back solution which requires only knowledge of the true position of two targets at two different ranges. The radars themselves could then act as atmospheric probes. During the research aspects of such a program, two or three high-speed horizon level and near-horizon fly-bys should be incorporated wherein the tracking of a true inertial target reference should reveal anomalous sections of the atmosphere, manifested as unstable radar, to which would be applied backward solutions.

Summary Statement

The era of mathematical exercises in designing correction models based on simple assumptions is over. When two or three mil errors can be demonstrated solely due to atmospheric anomalies, it makes little difference that mathematical model A is better than mathematical model B because it computes to .01 mils. If greater accuracies are to be expected at low angles from the Western Test Range, we must recognize the fallacy of assuming an ideal standard atmosphere.

REFERENCES

- Hankston, L., 1964: "Correction of Radar Elevation Angles Less than One Degree". Proc. Second Tropospheric Refraction Effects Technical Review Meeting, Tech. Doc. Report No. ESD-TDR-64-103, Electronic Systems Division, Air Force Systems Command.
- Bean, B. R. and E. J. Dutton, 1966: "Radio Meteorology". National Bureau of Standards Monograph No. 92, p. 52.
- Cermak, J. E., and J. Peterka, 1966: "Simulation of Wind Fields over Point Arguello, California". Engineering Research Center, Colorado State University, Fort Collins, Colorado, Contract N123 (61756) 34361A(PMR), 75 pp.
- Cunningham, R., Myers and Crane, 1966: Separate articles on same project in Proceedings of the Third Tropospheric Refraction Effects Meeting, Electronic Systems Division, USAF, L. G. Hanscom Field, Bedford, Mass., ESD-TDR-64-148, Vol. II.
- Cunningham, R., W.W. Vickers, C.C. Fain, 1963: "Effects of Clouds and Moist Layer Roughness on Range Rate Errors of Radio Interferometer Tracking and Guidance Systems", Air Force Cambridge Research Laboratories, Science Report AFCRL-63-706.
- Debye, P., 1957: "Polar Molecules". Dover Publications, New York, pp 89-90.
- Freeman, J. J., 1964: "The Real-Time Compensation for Tropospheric Effects On the Measurement of Range and Range Rate". Proc. of the 2nd Tropospheric Refraction Effects Tech. Review Meeting, ESD of Air Force Command, Bedford, Mass., 65D-TR-64-103, Vol. II.
- Gardner, C., 1969: "Comparison of Radar Refraction Correction Computer Programs, at Selected Test Ranges". EPWG Task 2, Unpublished Report, in preparation.
- , 1964: "Determination of Elevation and Slant Range Errors Due to Atmospheric Refractions" (revised). Pacific Missile Range, Tech. Note No. 3280-6, 63 pp.
- Kauper, E. K., D. F. Hartman and Charlotte J. Hopper, 1961: "Smog Forecasting in the Los Angeles Basin". Air Pollution Control District, County of Los Angeles, Air Quality Report No. 37, 21 pp.

- Long, R., 1953: "Experiments with a Two-Fluid System", Tellus, Vol. 5.
- , 1954: "Continuous Density Gradients", Tellus, Vol. 6.
- , 1955: "Some Aspects of the Flow of Stratified Fluids", Tellus, Vol. 7.
- Lopez, M., and W. Howell, 1967: "Katabatic Winds in the Equatorial Andes". Encyclopedia of Atmospheric Sciences and Astrogeology, Reinhold Publishing Corp., New York, pp. 518-522.
- Nason, C.K. and M.E. Lopez, 1967: "A Test of Certain Evaluation Designs for Cloud-Seeding Experiments". Final Report, Atmospheric Water Research, Bureau of Reclamation, Contract 14-06-D-5962.
- Rowlandson, L., and J. Herlihy, 1968: "Refraction Induced Tracking Errors and Correction Methods for the AF Western Test Range." Syracuse University Research Corp., New York, Contract No. F19628-68-C-0209, 105 pp.
- Rowlandson, Lyall, 1968: "Simple Analytical Functions which Provide Magnitudes of Range and Angle Errors for Propagation in an Exponential Atmosphere". Aerospace Instrumentation Program Office, ESD, Contract F19628-68-C-0209, Syracuse University, 27 pp.
- Schulkin, M., 1952: "Average Radio Refraction in the Lower Atmosphere." Proc. IRE 40, 554-561.
- Smith, E.K. and S. Weintraub, 1953: "The Constants in the Equation for Atmospheric Refractive Index at Radio Frequencies". Proc. IRE 41, 1035-1037.
- Smith, T. B., E. Kauper, S. Berman, F. Vukoviech, 1964: "Micrometeorological Investigation of U.S. Naval Facility, Point Arguello, California". Meteorology Research, Inc., Altadena, California, Contract N123-(61756) 32885 A (PMR), pp.120.
- Skalak, R., 1967: "Fluid Mechanics". Encyclopedia of Atmospheric Sciences and Astrogeology, Reinhold Publishing Corp., New York, p. 389.
- Stanfield, J.W., 1962: "An Aid for Predicting Radar Refraction in the Point Mugu Area, "U.S. Naval Missile Center, Point Mugu, California. Tech. Memo No. NMC-TM-62-44, 18 pp.

Thayer, G. D., 1961: "A Formula for Radio Ray Refraction in an Exponential Atmosphere". NBS, J. Research 66, D No. 3.

Wadsworth, G. P., 1951: "A Possible Experimental Design for Testing the Effectiveness of Cloud Seeding". Report for the Geophysical Research Directorate, Cambridge Field Station, Contract AF19(122)-401.

Weisbrod, S. and L. J. Anderson, 1959: "Simple Methods for Computing Tropospheric and Ionospheric Refractive Effects on Radio Waves" Pro. IRE 47, pp. 1770-1777.

Wong, M. S., 1951: "Ray Tracing Picture of Radio Wave Propagation in Arbitrary Atmosphere". Wright Air Development Center, Dayton Ohio, WADC Report No. 6631.

LIST OF ILLUSTRATIONS

APPENDIX

Figure No.

- B-1 Normal three-dimensional trajectories of air parcels starting at various positions at 700mb. (Number along trajectories; height in thousands of feet). After Neiburger, 1965.
- B-2 Occurrence of refractive layers (by percentage) over San Nicolas Island and Point Mugu during 1956. After Carr, 1958.
- B-3 Distribution of elevated layers with the refractive-index gradient greater than $-36N/1,000$ feet during July and August of 1956-57 over San Nicolas Island (110 observations). After Carr, 1958.
- B-4 Height Gain Measurements. After Bowen, 1965.
- B-5 Average diurnal duty cycle for Channel 9. After Bowen, 1965.
- B-6 Montgomery Field, San Diego, 0000z, $\theta_0 = 0\text{mr}$. After Shedd, 1966.
- B-7 Hilo, Hawaii, 0000z. $\theta_0 = 0\text{mr}$. After Shedd, 1966.
- B-8 Percentage of observations with no inversions during the months June-September. After Neiburger, 1966.
- B-9 Average potential temperature of inversion base during summer ($^{\circ}\text{K}$). After Neiburger, 1966.
- B-10 Normal sea surface temperatures in July ($^{\circ}\text{C}$). After Neiburger, 1966.
- B-11 Average height of inversion base during summer (hundreds of meters). After Neiburger, 1966.
- B-12 Average thickness of inversion during summer (hundreds of meters). After Neiburger, 1966.

B-13

Average summer cross section from San Francisco to
Honolulu. After Neiburger, 1966.

APPENDIX A

All refraction errors are interdependent. For the iteration technique, we have selected the bending error as the base from which all the other refraction errors are obtained, since the convergence of the iterations for the bending error is very fast and the computing procedure straightforward. In what follows, we show in detail the computation of the remaining refraction errors.

RANGE ERROR

Initially, we neglect the curvature of the path in the range computations (Section V). The elementary retardation error is (Weisbrod and Anderson, 1959)

$$d(\text{RGERR}) = -(n-1)dS \quad (46)$$

Introducing (24), (22), (32) and (33)

$$d(\text{RGERR}) = - \frac{10^{-6} \cdot N_o \cdot \exp(t_o^2 - t^2) \cdot dt}{A \cdot \cos \beta_o} \quad (47)$$

which can be integrated directly to yield

$$\text{RGERR} = -10^{-6} \cdot N_o \cdot \sec \beta_o \cdot (F(t_o) - E \cdot F(t)) / 2A^2 \quad (48)$$

where $F(x)$ is defined by (36).

Comparing (48) and (38) we obtain

$$\text{RGERR} = \tau \cdot \sec \beta_o / 2A^2 \quad (49)$$

If we now add the correction for curvature of path (17)

$$\text{RGERR} = (\tau \cdot \sec \beta_o / 2A^2 + S \cdot \tau^2 / 24) \cdot r_o \quad (49a)$$

where the range error has been multiplied by r_o to express it in conventional units. We can see from (49a) that for small angles of elevation the choice of β_o is not very critical since the secant varies very slowly at low angles of elevation. We can therefore substitute B_o for β_o in (49a) and obtain as the final expression

$$\text{RGERR} = \tau \cdot r_o \cdot (\sec B_o / 2A^2 + S \cdot \tau / 24) \quad (50)$$

ELEVATION ERROR

An iterative procedure can be used to determine the elevation correction " ϵ ". From equation (40) we can see that once τ is available, the elevation correction ϵ depends only on an estimation of the emergence angle B . Although (25) and (26) provide the basis for an initial estimation by setting $\beta_o = B_o$, the angle B is generally small and is not well determined by its cosine. It is better to modify the computations in a manner similar to that done in Section V and to proceed as follows:

Let

$$G = (t_o^2 - t^2)/2A^2 - 10^{-6} \cdot N \cdot (1 - E) \quad (51)$$

where t , t_o and E are obtained from (31) and (37) by setting $\beta_o = B_o$

and let

$$KI = 1 - \cos B_o \quad (52)$$

be computed accurately by using a suitable rational approximation as suggested in Section V.

Then

$$KB = BI + G \cdot (1 - KI) \quad (53)$$

and

$$\tan B = (KB \cdot (2 - KB))^{1/2} / (1 - KB) \quad (54)$$

$$\tan B_o = (KI \cdot (2 - KI))^{1/2} / (1 - KI) \quad (55)$$

A first estimation ϵ_1 is now obtained by using (40). A second iteration is now made by recomputing t , t_o and E from (31) and (37) using

$$\beta_o = B_o + \epsilon_1 \quad (56)$$

This second iteration yields a final estimation for the elevation error ϵ . The convergence of this iterative procedure is sufficiently fast that no further meaningful improvement in ϵ can be expected from further iterations.

DOPPLER VELOCITY ERROR ANGLE

Millman (1961) has shown that doppler velocity error in the radial direction which can be attributed to refraction is, to a first order approximation, measured by the angle δ (Figure 21), which is the angle between the ray direction and the slant path. From Figure 21, it can be seen that

$$\delta = \beta_o - \tau - B_o \quad (57)$$

But since $\beta_0 - B_0 = \epsilon$, the elevation error, we have that

$$\delta = \epsilon - \tau \quad (58)$$

which shows that a doppler correction angle is immediately available from the estimates for the total bending and the elevation angle error.

A QUADRATIC EXPONENTIAL MODEL

In our previous work, an algorithm has been developed to perform fast and accurate refraction corrections for an atmosphere whose refracting index decays exponentially with height. The logical question has been considered by Bean and Thayer (1959) and practical experience has shown that the exponential model fits most observed profiles reasonably well. Rowlandson (1968) has shown that even large departures from the exponential model results in modest differences in the computed corrections if suitable parameters are chosen.

We can use available direct inputs such as radiosonde data, spirals, etc., to derive the parameters of a best-fitting exponential model. There is another alternative (suggested in our summary and recommendation) if targets of known position are available, of using the radar as an atmospheric probe by performing a back solution of equation (38). For the moment, however, we are concerned with the first alternative.

If a refractive profile is available, the solution for the best parameters is handled by standard curve-fitting techniques such as a least-squares routine. The simple exponential model which we have been considering involves fitting a least-squares straight line to H_1 and $\ln(N_1)$. As soon as several of these plots are made, however, one is immediately tempted to improve the fit by going to higher-order polynomials, especially where a strong inversion is present. If the monomial in the exponent of equation (22) is substituted by a binomial, we obtain a quadratic model where

$$N = N_0 \cdot \exp(-D_1 \cdot H - D_2 \cdot H^2) \quad (59)$$

and we could fit a parabola to the plot of H_1 , $\ln(N_1)$ instead of a straight line.

If we make the appropriate substitutions in (22) and (25) and neglect terms higher than second-order in the subsequent derivations, we find that we only need to make

$$A = (D_1/2)^{1/2} \cdot (1 + D_2 \cdot \tan^2 \beta_0 / (D_1/2))^{-1/2} \quad (60)$$

instead of the value given in (31) to arrive at the same solution (38) for τ . This makes the use of a quadratic model almost as practical as that of the

simpler linear exponential, since the fitting of a parabola to a set of data is still a very simple computational procedure. However, in general, we have seen that single point radiosonde data may not detect the atmospheric anomalies which so much affect tracking at low angles of elevation, so the gain in accuracy using a quadratic model may be illusory. If detailed cross-section data or targets of known position are available, it seems preferable to use the linear exponential model to estimate an equivalent average decay parameter in the manner suggested in the next paragraph.

DETERMINATION OF THE DECAY CONSTANTS - POSSIBLE USE OF THE RADAR BEAM AS AN ATMOSPHERIC PROBE

It is obvious that the success of the real-time computations depend on a proper estimation of the parameter N_0 and the decay constant DEN in the case of a simple exponential atmosphere or the two decay constants D_1 and D_2 of the quadratic model. A least-squares fitting routine could be used to determine the constants when inputs such as radiosonde data are available. Rowlandson (1968) has discussed this problem in more detail.

In the course of our work, we had atmospheric data at our disposal, and it soon became evident that the radar inputs themselves could be used to estimate the decay constants if we could solve the refraction equations backwards. We posed the question: If we know what the elevation angle and bending corrections should be, what average state of a hypothetical stratified atmosphere would have such a solution for the given initial conditions? Since the equations are non-linear and the unknowns are implicit, some sort of iterative solution is necessary. We have made a preliminary exploration of the problem and have succeeded in devising a technique based on the bisection method to isolate the roots rather rapidly. The procedure appears to be both convergent and stable.

The bonus to be gained from such a procedure is quite apparent. If two targets of known position are available, radar inputs define the constants of an average equivalent atmosphere. The targets can be fixed or stationary, but in view of the many desirable look angles, a fly-by using inertial guidance seems to offer the greatest potential to define an equivalent atmosphere.

We have already made computations using the known position of the aircraft as defined by the radio altimeter and the radar range as the best available absolutes, and have come out with decay constants which can reproduce the actual departures at intermediate points far better than the radiosonde of simple spiral data. Since the procedure cannot pinpoint the exact location of the anomalies, but averages them throughout, this short survey indicates that the observations should be carried at two elevations and two ranges, one at least a fairly long one to insure that a thick slice of the lower atmosphere is traversed. This is an area that should be explored further.

APPENDIX B

PACIFIC INVERSION LAYER ACTIVITY

During our 1967 Vandenberg operations serious thought was given to the possibility of predicting inversion layer activity (changes in strength and/or geometry) by statistical techniques and mathematical modeling. One would hope to identify parameters for which physical observations and theory would indicate they had strong control over inversion activity. The control would be confirmed by statistical correlation from which one would next model the theoretical association of these parameters. The intent would be to simulate inversion activity. The applied reason for such effort would be for predicting inversion conditions that were hazardous to missile tracking. The first phase of this program has been completed, that of identifying parameters for which theory or past work indicated a degree of control over inversion activity. A condensation of this research appears in this Appendix. A good understanding of inversion activity and its significance to radar can be obtained from this review.

GENERAL INVERSION DESCRIPTION

Tracking variations at Vandenberg Air Force Base can be traced to the presence of the strong northeast Pacific inversion through which most tracking must take place. The inversion layer is formed at the interface between subsiding anti-cyclonic air from aloft and the marine layer generated immediately above the ocean surface. These layers have markedly different temperature and water vapor characteristics. Sandwiched between these two air masses, is the inversion layer, about 150 m. in thickness, and rising from an altitude of some 400 m. off the coast of California to 2,000 m. over Hawaii. It also experiences a slight upward warping along the immediate California coast.

Figure B-1, after Neiburger, 1965, shows the general summer position of an anti-cyclonic high pressure system which is characterized by dry subsiding air. Note the streamlines of flow, diverging from the center of the high pressure area, flowing along the coast of California, then to the southwest to form the northeast trades.

A large lateral plane of demarcation (the inversion layer) between the upper subsiding air and lower marine air mass is maintained by the temperature inversion at their interface. Since the temperature increases markedly with height in this layer, strong dynamic stability is created. This stability is generally sufficient to prevent penetration by the convective cells generated by the heat released from the ocean surface. As one moves westward from the coast of California, however, cumulus convection increases due to

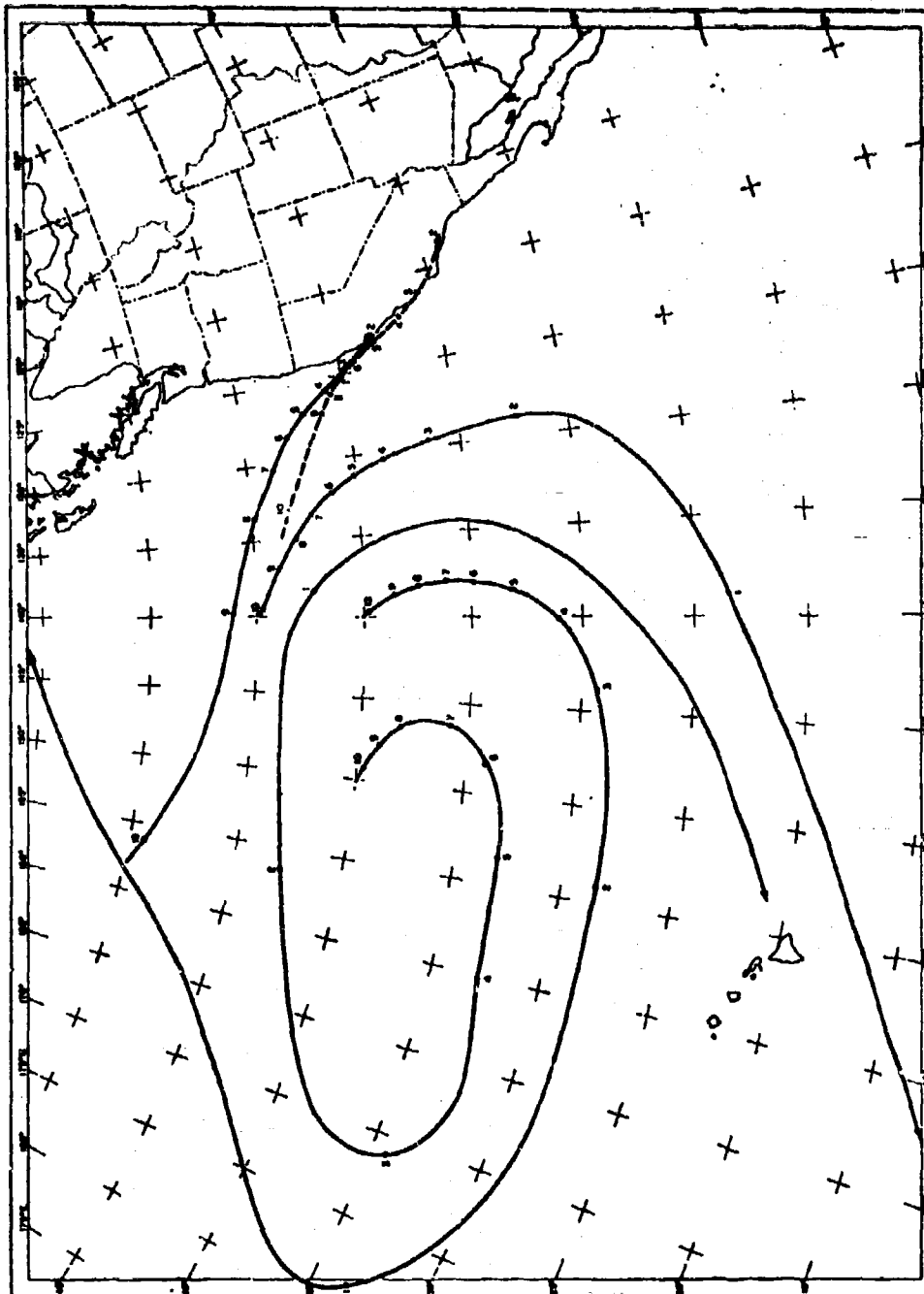


Figure B-1 NORMAL THREE-DIMENSIONAL TRAJECTORIES OF AIR PARCELS STARTING AT VARIOUS POSITIONS AT 700 mb. (NUMBER ALONG TRAJECTORIES; HEIGHT IN THOUSANDS OF FEET). AFTER WEIBURGER, 1965

increasing Ocean temperature. It increases to a degree where the upward transport of vapor and momentum are sufficient to penetrate the stable layer. The penetration starts with mild perturbations of the layer and increases to actual penetration of the layer in the vicinity of Hawaii. We recognize these penetrations as chimney-type cumulus clouds. It is the upward transport of vapor and momentum, through convection, that is responsible for both the raising of the inversion layer as one goes westward and the eventual destruction of the inversion layer. Since greater and greater amounts of vapor are mixed into the dry air above, the dry air becomes more like the air of the lower marine layer. The inversion layer itself gets thicker with more diffuse boundaries as the mixing reaches upward. Eventually the inversion demarcation completely disappears. The interface between the dry and moist air is not a discontinuity, for mass transfer actually takes place between the dry and moist air. It is the physical characteristics of the mass that change.

The preceding paragraphs (taken largely from Riehl, 1951, and Neiburger, 1965) should give one a gross concept of the nature of the northeast Pacific inversion. This is the crux of our concern with respect to tracking problems.

The balance of this exposition reviews the real effects of the inversion as demonstrated by field experiments, by Carr et al (1958) and Bowen et al (1965), and supplements this with statistical compilations by these same authors, and also Sheddy (1966). Next the work of Riehl et al (1951), and Neiburger (1965) is reviewed in sufficient detail to isolate the physical parameters which their data indicate could reasonably be suspected of exercising some control over the activity of the inversion layer. These parameters are to be investigated for their value as predictors of inversion layer activity. These parameters are tabulated in the summary at the end of this writing. An investigative approach to the handling of these parameters is suggested, along the lines of an eigenvector analysis by Stidd (1967); or, a screened multiple-discriminate analysis by Enger (1965). The following review will establish the state of the art regarding work on the Pacific inversion pertinent to existing tracking problems at Vandenberg as well as establish a point of departure for an investigation regarding inversion activity prediction.

STATISTICAL COMPILATIONS AND FIELD EXPERIMENTS ON REAL EFFECTS OF THE INVERSION

As an indication of the occurrence of strong refraction conditions over San Nicolas Island and Point Mugu, Carr has plotted data from 1956, Figure B-2 showing the time variation (annual) of the frequency of occurrence of inversions strong enough to produce trapping conditions (with refractive index greater than 36 N per 1,000 feet). The circled numbers adjacent to data points are numbers of observations. Note that the frequency of occurrence of tracking conditions has a maximum in summer. These data are in agreement with similar compilations by Sheddy (1965) and Bowen (1966), among others.

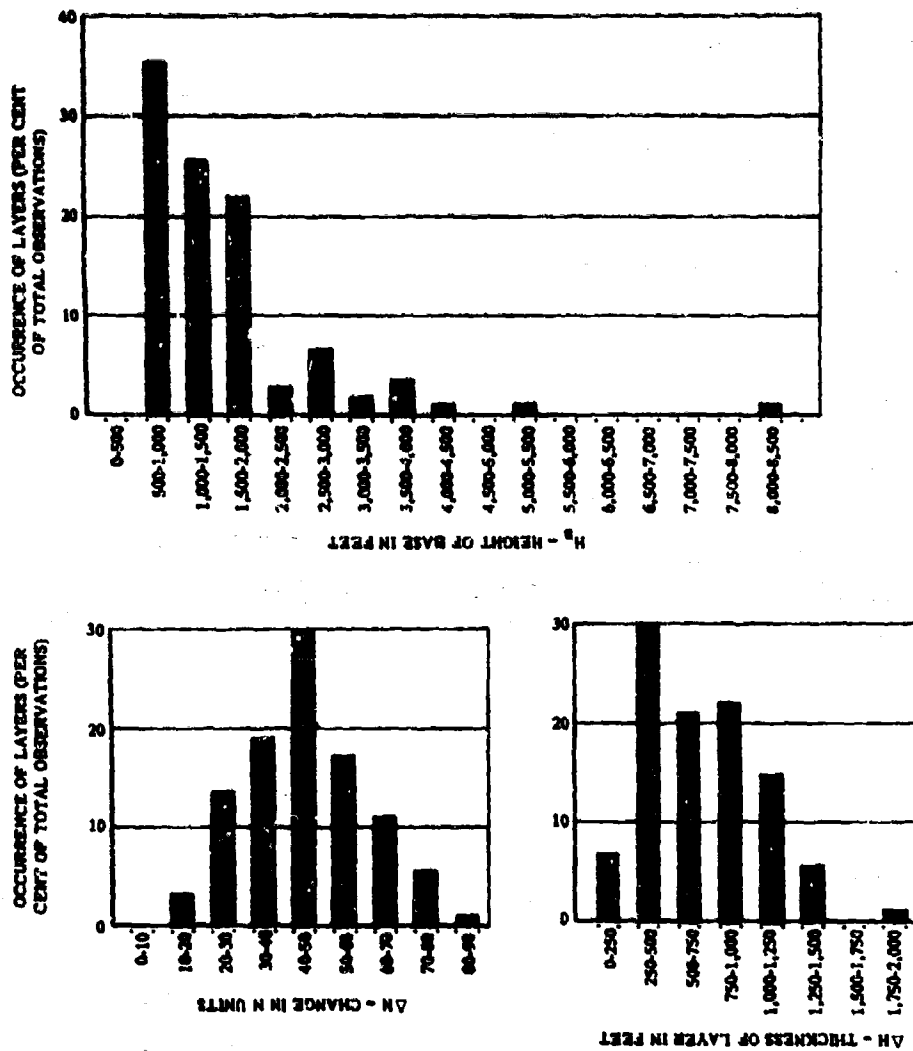


Figure 8-2. OCCURRENCE OF REFRACTIVE LAYERS (BY PERCENTAGE) OVER SAN NICOLAI ISLAND AND POINT MUGU DURING 1956. AFTER CARR, 1958

Additional data compiled on the distribution of elevated layers during the summer maxima are shown in Figure B-3. The modes of these distributions suggest that we are likely to find a layer with a 40 or 50 N unit change with 250 to 500 feet of layer thickness, and with the base of the layer 1,000 feet in altitude.

In the work of Bowen et al (1965), we find an empirical display of the relation between the inversion layer and trapping conditions. Bowen and his colleagues set up three receivers on the abruptly precipitation coast of Point Buchon 170 miles northwest of Los Angeles. These stations monitored signal strength from Hawaiian television stations at several frequencies. In Figure B-4, we note from the signal strength record (left margin) that stations A and C received stronger signals the closer the inversion layer came to their respective altitude levels. As the inversion layer climbed with time the strength of the signal dropped. These experimental recordings accentuate the importance to be attached to inversion layer and receiving station geometry. The fluctuations in the signal strength curves are alleged to result from the passage of undulations in the geometry of the inversion layer itself. In general, the signals that were received at the upper and lower sites were similar in fading characteristics but not in power levels received. Signal level at the upper site was higher than the lower site. On several occasions signals were received at respective stations, only when the inversion layer moved directly through the antenna structure (ducting). On these occasions the inversion layer was characterized by very sharp gradients.

From the same work the investigators have compiled the statistics of signal strength received as a function of time, diurnally and seasonally. We note in Figure B-5 the signal strength peaking at about 1530 in the afternoon. This is probably near the time of maximum absorption of insolation (temperature) at the top of the marine layer, and conceivably could be a contributing mechanism to diurnal fluctuation of the layer (this parameter should be included in any inversion predictor investigation).

Sheddy (1966) has made a study of the magnitude of the angle of arrival error of a horizontal ray using data from radiosondes from different geographical locations (San Diego, Weather Ship N in mid-ocean and Hilo, Hawaii) and time of year. The angle errors computed from radiosonde profiles are then compared against angle errors calculated from the use of the surface index of refraction, in the CRPL reference atmosphere model. Sheddy shows for San Diego that angular error is greatest in summer as might be expected from the higher water contents in the lower atmosphere during this season; and Figure B-6, after Sheddy, shows the difference in error, e_d , between a radiosonde-based calculation and CRPL reference atmosphere-based calculation also is greatest in the summer. (Magnitude of error is lower at higher elevation angles, but the shape of curve is the same. There is also a winter night anomaly at San Diego, where the error difference becomes

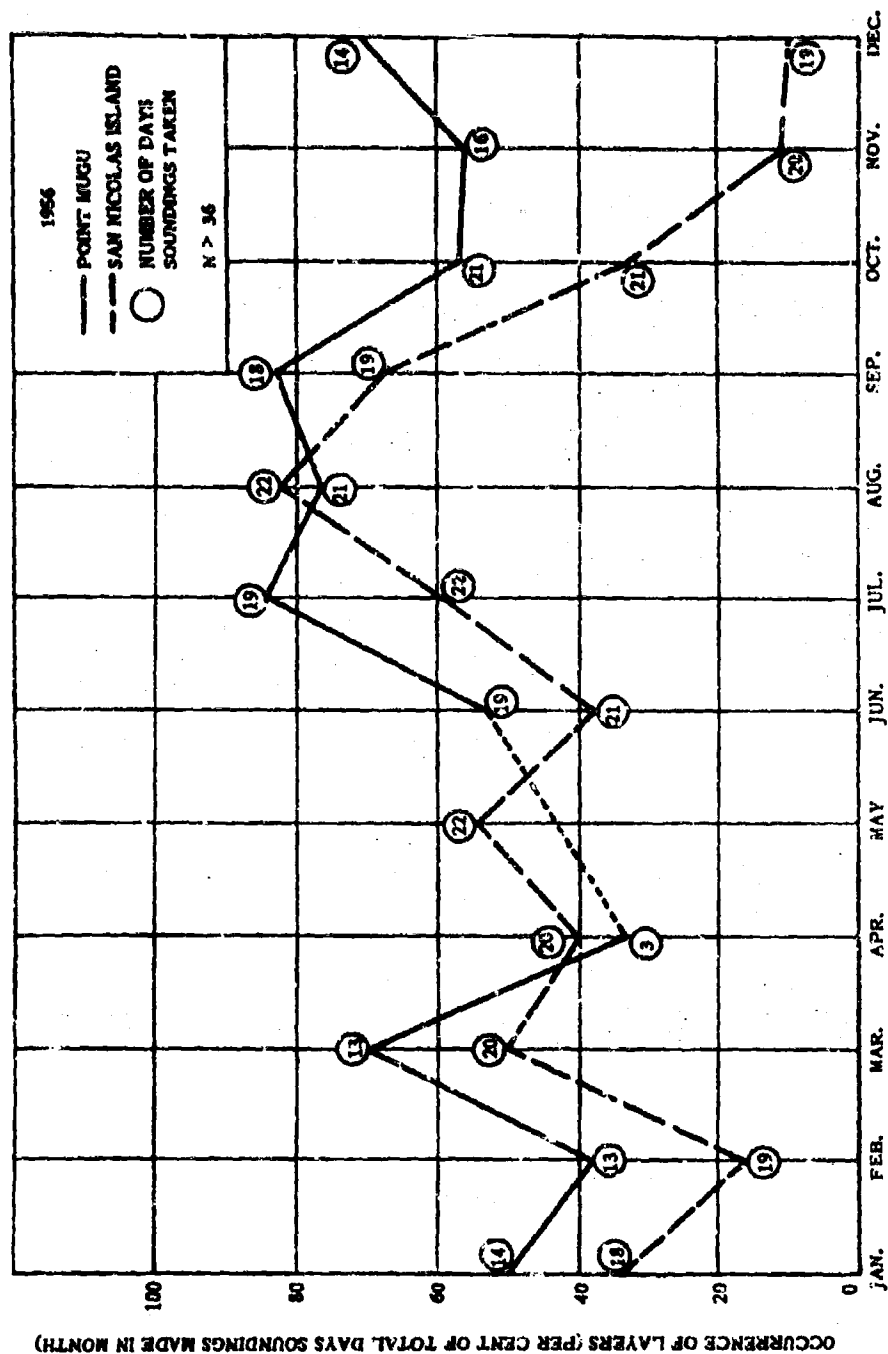


Figure B-3 DISTRIBUTION OF ELEVATED LAYERS WITH THE REFRACTIVE-INDEX GRADIENT GREATER THAN $1/36N/1,000$ FEET DURING JULY AND AUGUST OF 1955-57 OVER SAN NICOLAS ISLAND (110 OBSERVATIONS). AFTER CARR, 1956

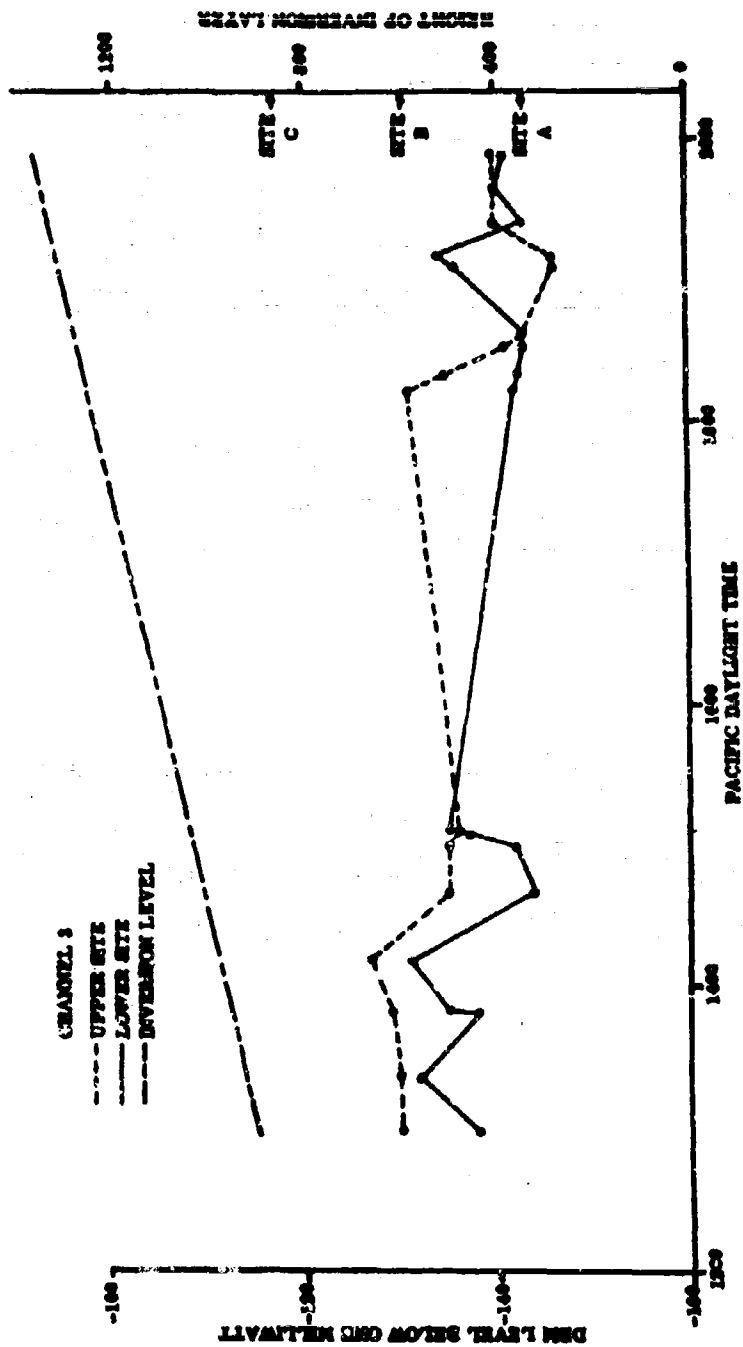


Figure B-4 HEIGHT GAIN MEASUREMENTS. AFTER BOWEN, 1965

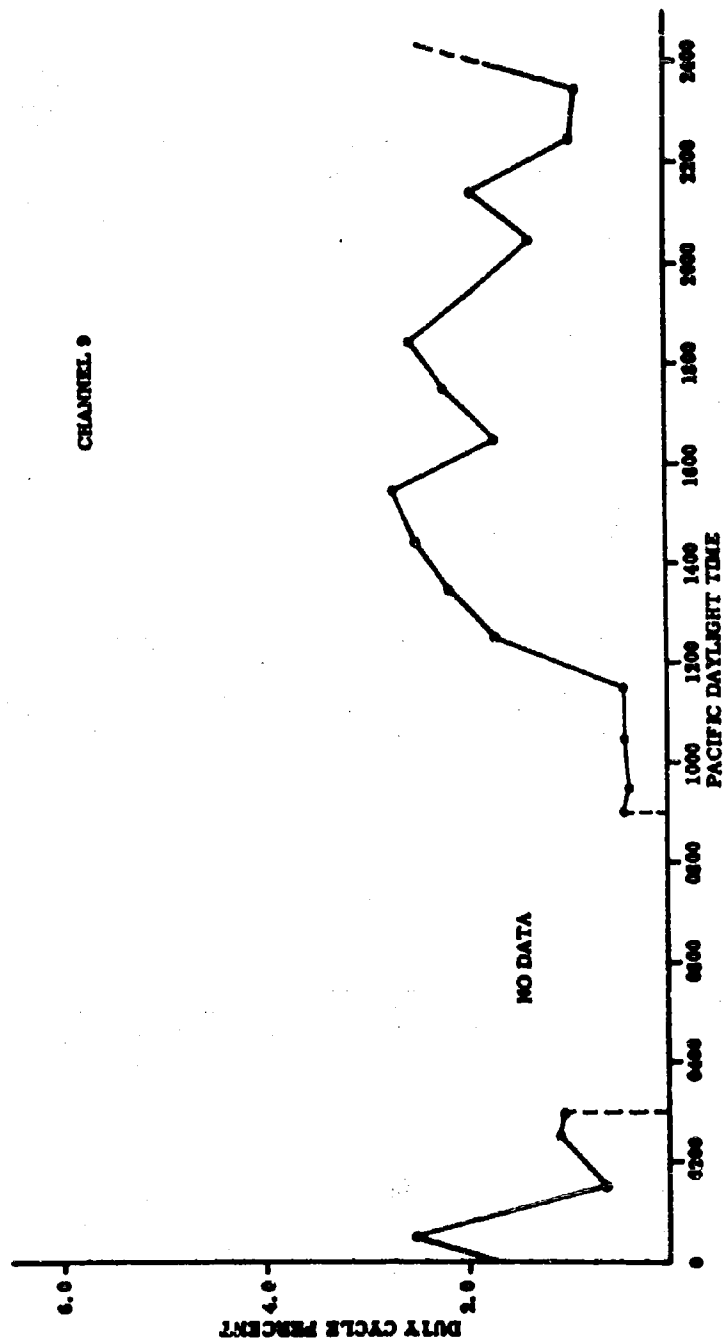


Figure B-5. AVERAGE DIURNAL DUTY CYCLE FOR CHANNEL 9. AFTER BOWEN, 1965.

large, possibly due to strong radiational cooling at the surface producing a meaningless surface N). Note, however, that the more seasonally homogeneous atmosphere at Hilo, Figure B-7 has a correspondingly flat error distribution; and has a generally lower magnitude of error due to the weaker inversion-associated water vapor gradient. In the discussion of Riehl's work, penetrative convection (increasing westward towards Hawaii) is the mechanism for transporting moist marine air through the inversion interface to the dry air aloft. This process tends to destroy sharp gradients. From Sheddy's graphs, one concludes that any atmosphere or any season has acceptable error at Hilo where weak gradients exist. The mid-ocean weather ship data show even less error, with a slight summer bulge in the plot likely due to a warmer marine layer with a higher absolute water load. We see in these statistics the apparent effect of refraction gradient as revealed by angle error calculations for different geographic locations. The conditions differ in the important parameter of water vapor gradient (strength of the inversion). Thus, there is revealed here an additional parameter for any predictor investigation.

LARGE-SCALE METEOROLOGICAL STUDIES

In his study of heat and moisture balance in the marine layer Riehl (1951) showed that the net heat export via the trade wind flow was in the form of latent heat. He also found that radiative cooling at the top of the marine layer increased over the average clear sky rate of cooling by about 33% in the presence of a stratus deck. The normal heat flux of the marine layer leaves a residual of about 1.1 m cal/day available for net export (can be monitored by temperature differential at inversion level). This is about 20% of the heat transferred from ocean to atmosphere and is available for modifying the characteristics of the subsiding air. For this reason the amount of latent heat surplus (monitored via heat flux) could be a parameter of interest in any investigation of inversion activity.

Of further thermal significance absorption of the incoming insolation at any level is proportional to the water vapor content at that level, and inversely proportional to the total moisture content about that level. This places maximum absorption near the base of the inversion at about the 800 mb height and suggests that the resulting thermal expansion may contribute somewhat to those geometric changes of the inversion layer about which we are concerned. We therefore add water vapor at the base of the inversion as a parameter to be monitored (as well as total water vapor profile in the marine layer).

The principal output of Riehl's work, other than explaining the changing geometry of the inversion layer in terms of diffusion of the marine layer into the dry air above, was his explanation of the role of vertical momentum produced by convection. Riehl shows logically that low-level flow from the east-northeast is produced largely by the pressure gradient. However, this flow

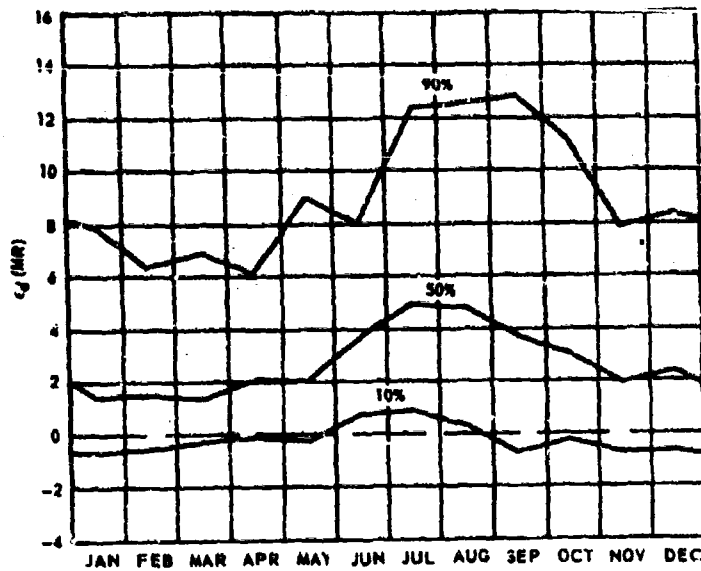


Figure B-6. MONTGOMERY FIELD, SAN DIEGO, 0000Z. $\theta_0 = 0\text{mr}$.
AFTER SHEDDY, 1966

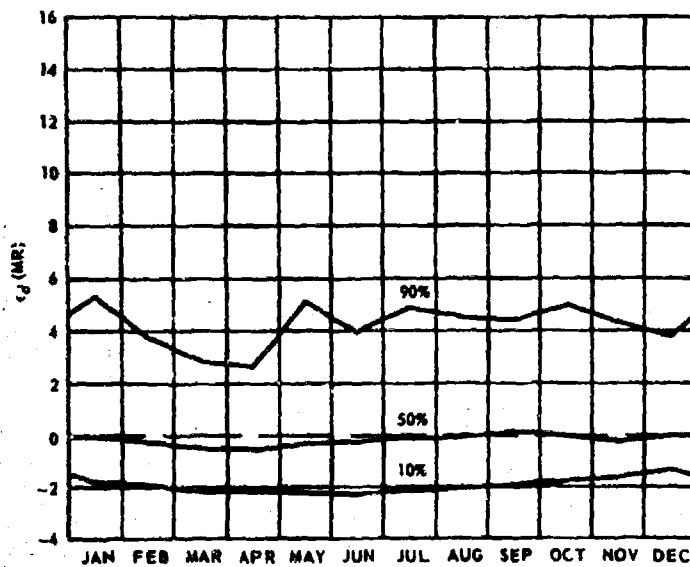


Figure B-7. HILO, HAWAII, 0000Z. $\theta_0 = 0\text{mr}$.
AFTER SHEDDY, 1966

is checked by the generation of vertical momentum in the convective cells of the marine layer. The action of this checking is thought to be largely a function of form drag of the cells. This is suggested by the relationship of wind speed at various levels to cell size at various levels. From the standpoint of predicting inversion layer activity, the vertical momentum generated is instrumental in the penetration of convective cells through the stabilized inversion and thereby contributes to the height alteration, and/or to the total destruction of the inversion. Also, while monitoring the intensity of this mixing at the inversion interface through the momentum parameter, we may wish to monitor the transfer of moisture which Riehl shows is not necessarily proportional to momentum. We therefore will wish to look closely at the Austausch coefficients of momentum and water vapor as possible predictors of inversion layer activity.

We have briefly examined the work of Riehl, et al, and find additional parameters that could logically be exercising control on, or partial control on the activity of the inversion layer. A tabulation of these parameters plus those suggested by the work of other investigators, will be found in the concluding sections of this writing. We next examine the implications of Neiburger's mapped parameter distributions.

Perturbations of the inversion layer must be considered at three general scales of motion: macroscale, or motions comparable to those of large cyclonic/anti-cyclonic weather systems; mesoscale, comparable to the flow associated with land and sea breezes; and microscale, which in this case we will view as motions in the fine structure of the inversion layer such as that produced by single cell convective penetration or gravity wave undulations found at the marine layer and subsiding air interface.

Turning here to the macroscale, we have noted that the semi-permanent anti-cyclonic high (Figure B-7) which sits over the Eastern Pacific is a principal instrument in the creation of the inversion layer. One might view this high as a large spiral descending vortex. As the air descends it diverges outward and anti-cyclonically around the center of the high. The other input necessary for the formation of the inversion layer is the marine layer, which is manufactured by moisture from the ocean surface. Bearing in mind the outward divergent flow, we note in Figure B-8 the coincidence of the inversion layer presence with the region of this strong divergence, which suggests connection between the two. Therefore, we may wish to add divergence to the list of possible statistical prediction parameters. Note that the shaded area of Figure B-8 is coincident with the region of strongest divergence shown in Figure 1. The lessening inversion layer presence to the westward of the Hawaiian Islands area is due to converging southwesterly flow. The dropoff of observed inversion presence along the coast of Baja, California is due to frequent north westward migration of tropical cyclones (convergence) and the dropoff to the north, off the coast of Washington, is due to the frequent passage

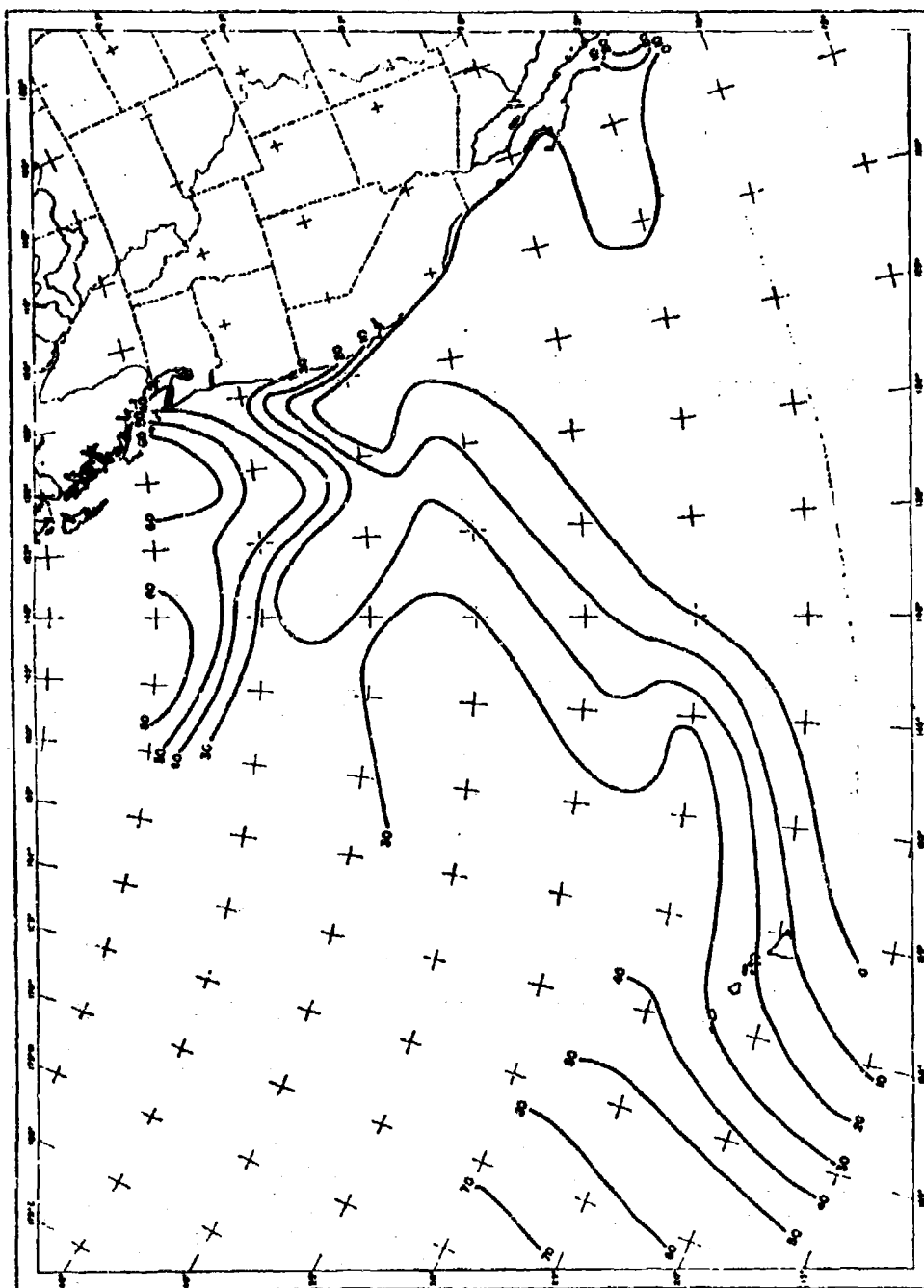


Figure B-8 PERCENTAGE OF OBSERVATIONS WITH NO INVERSIONS DURING THE MONTHS
JUNE-SEPTEMBER, AFTER NEIBURGER, 1966

of winter storms (convergence). South toward the Equator, the map shows an absence of data. However, we know from the late 1940 cruises of the Horizon and crest that the inversion layer slopes upward as one proceeds south, and as one approaches the zone of inter-tropical convergence the inversion is ultimately destroyed. The zone of inter-tropical convergence is where the northeasterly flowing trades of the northern hemisphere converge with the southeasterly flowing trades of the southern hemisphere. At this point of convergence the air rises vigorously and the inversion layer is destroyed in the process.

Let us deviate for a moment to explain the meteorological concept of convergence and divergence. Assuming a volume to remain constant as we deform the geometry of a cube of air, it is clear from the conservation of mass that if we reduce the height of the volume (vertical subsidence), we must expand laterally in either the x or y direction or both. Conversely, if we increase the height of the volume, an inward flow, or convergence, must take place. The area of strong divergence in our Pacific anti-cyclone has strong subsidence and outward lateral flow. (Subsidence is also directly related to vorticity, or intensity of rotation of the total vortex.)

If this subsidence is opposed with upward flow produced by the warm ocean surface heating the air and generating upward momentum within this convective layer, an interface is formed between the upward rising marine air and the downward subsiding adiabatically warmed air being yet warmer than the ocean warmed air which has cooled slightly with altitude. Not only does the temperature profile reverse itself, but sharp changes in water content also occur.

There is strong indication from the distribution of inversion layer presence, and distribution of divergence (or convergence) that a strong cause and effect relation may exist between these phenomena. We submit divergence (or subsidence, or vorticity; not statistically independent as a parameter for further investigation. What affects the inversion on an eastern Pacific macroscale, can also affect it on a Vandenberg local scale. Let us continue with the Neiburger mappings.

Figure B-9 is a map of potential temperature distribution. Potential temperature is a term employed by meteorologists to exclude compressive heating when comparing tow parcels of air from separate altitudes. We Note in Figure B-9 that the gradient of potential temperature follows closely the gradient distribution of ocean surface temperature (Figure B-10). Apparently, the marine layer temperature is being controlled specifically by the temperature of the underlying ocean surface, at least on the macroscale. The cold sink off the California coast is due to well-known upwelling conditions wherein cold ocean bottom water is brought to the surface. Note in Figure B-11 how the height of the inversion base has a distribution very similar to that of potential temperature. Similarities of these distributions

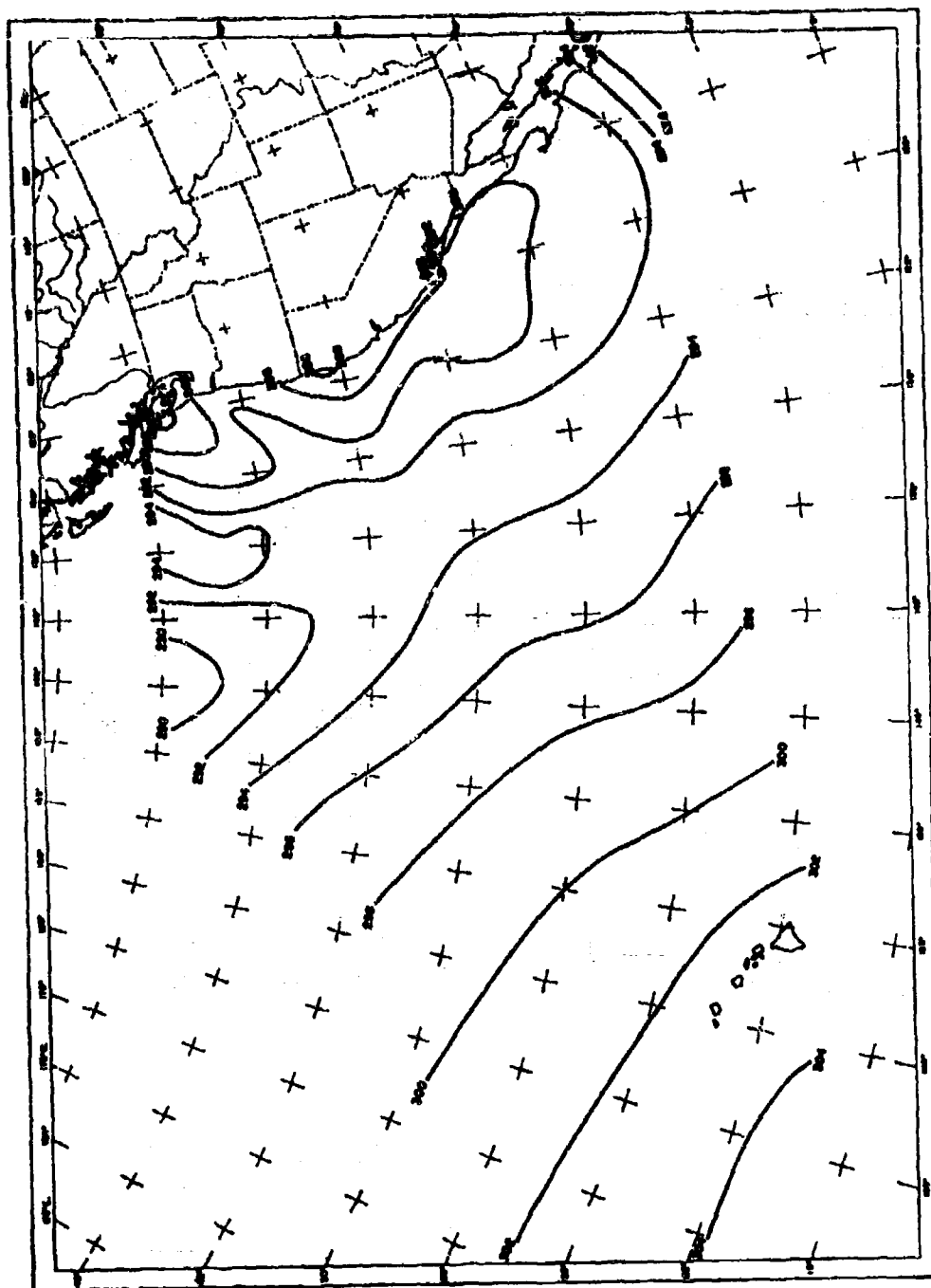


Figure B-9 AVERAGE POTENTIAL TEMPERATURE OF INVERSION BASE DURING
SUMMER ('K). AFTER NEIBURGER, 1966.

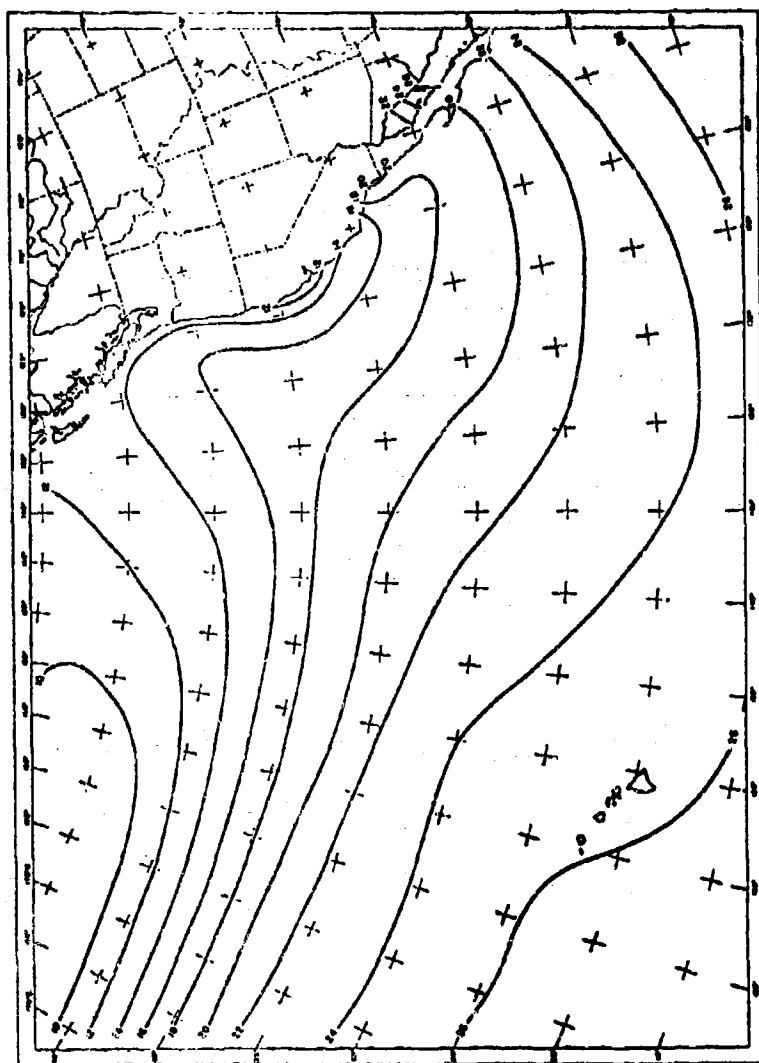


Figure B-10 NORMAL SEA SURFACE TEMPERATURES IN JULY (°C). AFTER NEIBURGER, 1936

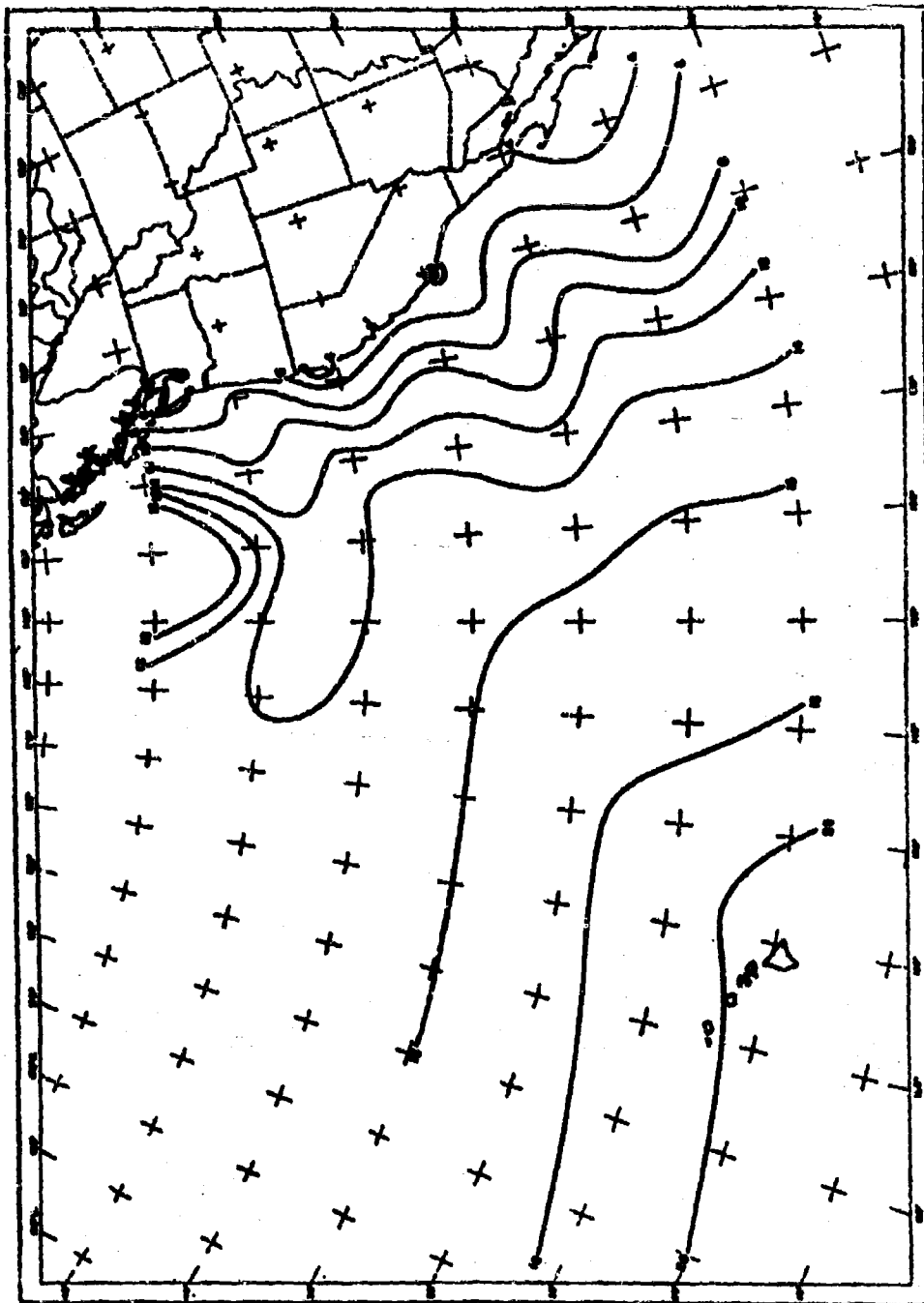


Figure 8-11 AVERAGE HEIGHT OF INVERSION BASE DURING SUMMER
(HUNDREDS OF METERS). AFTER NEIBURGER, 1966

suggest that a strong cause and effect relationship may exist between these parameters. We therefore isolate potential temperature as another parameter to be investigated. Note also that the inversion base slopes upward to the west from about 400 m. near the California coast to more than 2,000 m. near the vicinity of the Hawaiian Islands. The slope is the greatest over the eastern portion of the ocean, namely about 1:1000. As we observed from already initiated field work, the slope becomes much steeper (1:50) on the Vandenberg local scale. The significance of slope is that it alters the grazing angle of a given radar transmission path (ray) as it goes through the inversion layer. This is, the ray may be reflected or refracted at shallow angles, depending on the geometry of layer height and station height.

We have excluded a diagram of the average height of the inversion top during summer. It conforms closely to the topography of the inversion base, suggesting that the dominating influence in determining these average heights is the same for each case. However, an observed point which does not show in the averages is that a rise in inversion base is often preceded by a rise in inversion top. We therefore add rate of change of inversion top to our list as a possible predictor of change in inversion base.

Figure B-12 shows the distribution of inversion layer thickness, with minimum thickness directly off the coast of California in the Vandenberg area. The area of smallest thickness and greatest temperature increase going through the inversion layer reflects strong subsidence. The greatest temperature at the inversion top is in the southeast where the inversion is lowest. A minimum sea surface temperature in the coastal area produces cooling and settling of the surface layers, which enhances the subsidence and divergence produced by the anti-cyclonic high aloft. This is in contrast to other regions where warming of the sea surface produces strong cells of warmed rising air which diminish the inversion contrast. Where we have the strongest gradients we may also expect the strongest perturbations. This re-emphasizes our need to monitor temperature gradient through the inversion layer (already suggested as an indicator of heat flux).

Figure B-13 presents a summary of the macroscale cross-section of the inversion layer between the Pacific Coast and Honolulu. First, note the rapid rise of the inversion height near the coast (excludes mesoscale coastal upwarp), with a gradual lessening of slope to the westward. Note also the high temperature at the top of the inversion near the coast, presumably from the strong subsidence; and thirdly, note the gradual warming of the entire air column below the inversion as one proceeds westward over an increasingly warmer water surface.

We noted in looking at this early Neiburger work that there seemed no direct relationship between windspeed and inversion height. Other sources, however, (Kauper, 1961) point out that gradient winds in the local Los Angeles

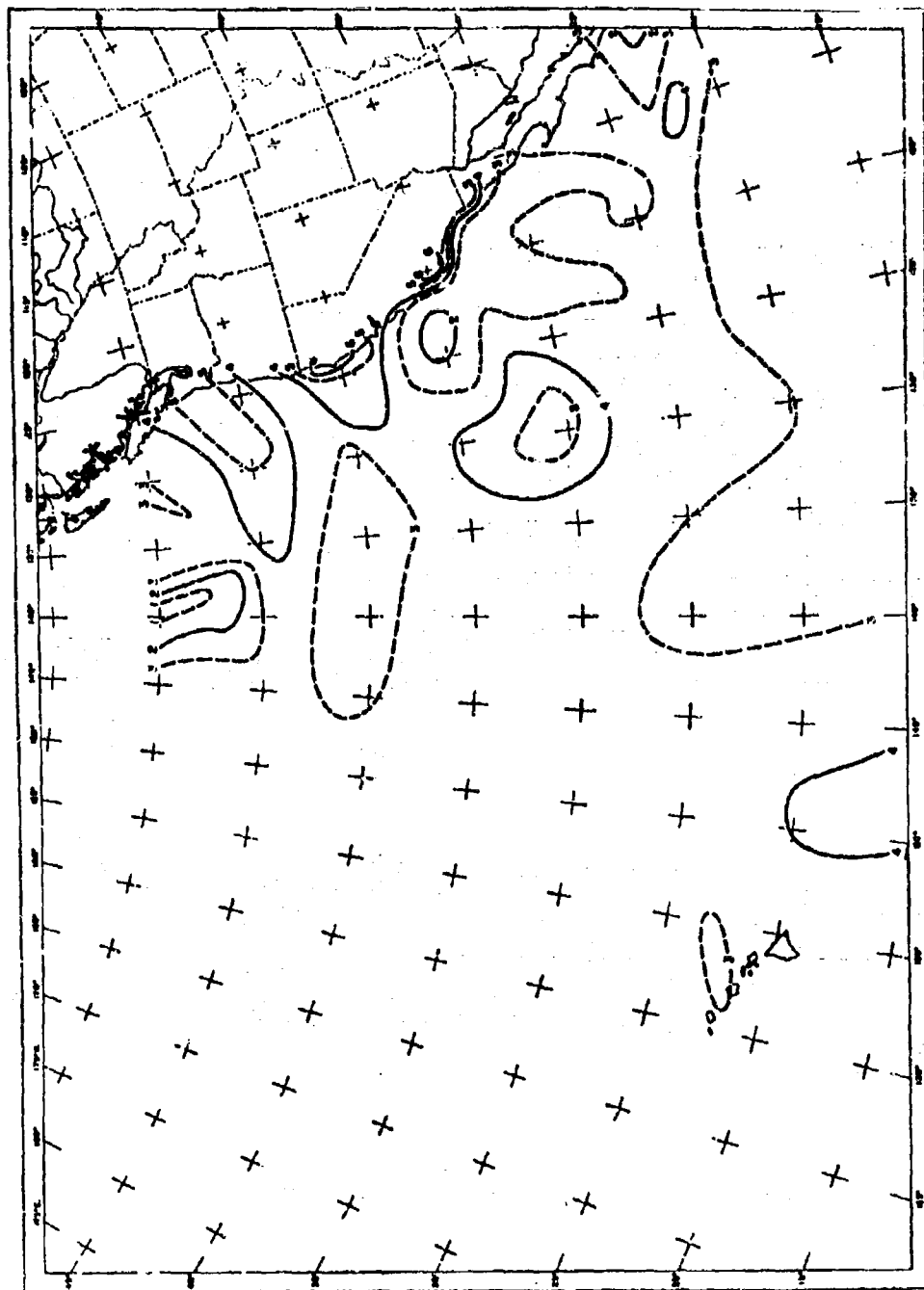


FIGURE B-12. AVERAGE THICKNESS OF INVERSION DURING SUMMER (HUNDREDS OF METERS). AFTER NEIBURGER, 1966.

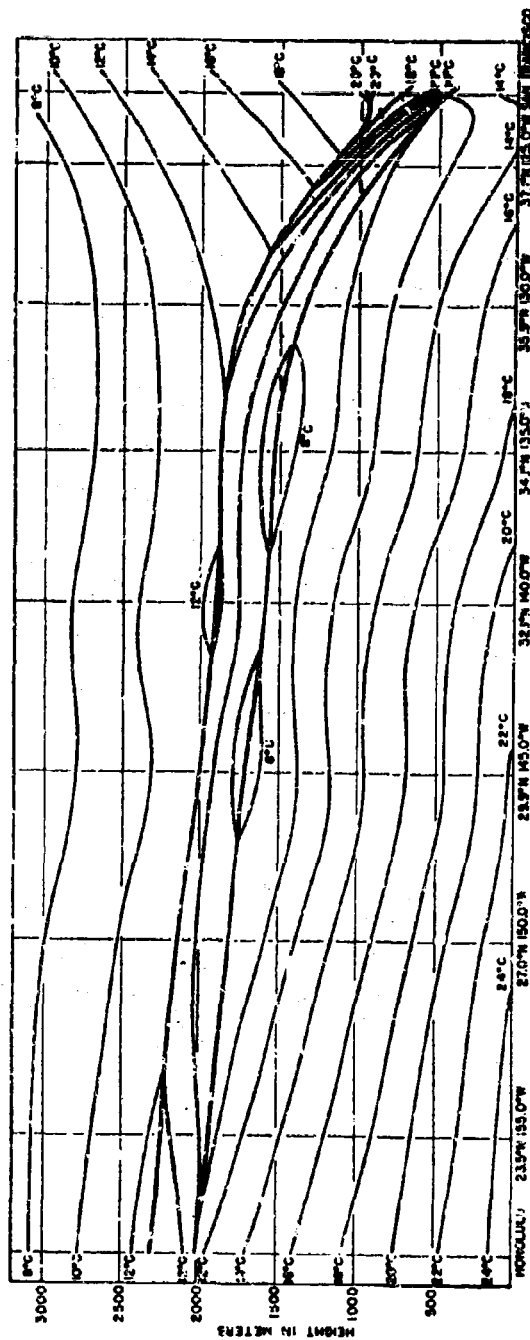


Figure B-13 AVERAGE SUMMER CROSS SECTION FROM SAN FRANCISCO TO HONOLULU, AFTER NEIBURGER, 1966

TABLE B-1
Summary of Pertinent Meteorological Parameters

VARIABLE	WHERE MEASURED	REASON FOR SELECTION	EXPECTED EFFECT
Mixing ratio.	Top of marine layer	Place of max. insolation absorption by water vapor	Diurnal change in inversion geometry
Potential temp.	Total marine layer profile; and a mean value above inversion	Major form of heat advection (export) — and a stability factor	Greater than above time scale; change in geometry and in inversion strength
Temp. differential	Through inversion layer	Represents radiative heat flux, and marine layer heat surplus.	Diurnal change in geometry.
Inversion height rate of change	Inversion top	Empirical observation (top leads the base)	Change in inversion base.
Subsidence, vorticity, or divergence	Routine radiosondes, plus calculations for 700 mb level	A measure of downward momentum and rate of adiabatic heating	Defines geometry and strength of inversion
Stability index* (an indirect measurement)	Significantly, marine layer	An indirect measure of vertical momentum and water vapor transport (convection). Contributes to mixing at inversion interface	Change of geometry and strength
Pressure gradient	NE to E quadrant of Pacific high	Controls low level wind (and consequent mixing).	Change of geometry and strength
Gradient wind, and sea breeze	L.A. - Lancaster, surface; and VGB	Empirical observation	Change of geometry and strength

* Not statistically independent of potential temp., but could be a better representation.

SUMMARY AND SUGGESTIONS

The variable to be predicted (e. g. height of inversion) is classified into several mutually exclusive groups. Drawing on the total collection of inversion height-change data we can use for respective groups such distinctions as no change = 0 + 5%; average change = 5% to 1 standard deviation; significant change = 1 standard deviation. Expressed in symbols we might use 5, S and >, respectively. In its most simple form we can plot the observed value of our predictor, X, --- say, change in potential temperature which preceded the inversion activity, for each case of inversion category mentioned above, 5, S, >. The average predictor value for respective categories, \bar{X}_5 , \bar{X}_S , $\bar{X}_>$, might appear as below, as would the average for all cases, \bar{X} .

38

$\lambda = \frac{\text{measure of distance among group means}}{\text{measure of spread about means}}$

$$\text{or, } \lambda = \frac{\sum_g n_g (X_g - \bar{X})^2}{\sum_g n_g \sigma_g^2}$$

where g represents 5, S, λ and n_g is the number of cases in each group.

There are refined techniques for selecting a minimum set of efficient predictors from a larger set of possible predictors, referred to as screening discriminant analysis. Many variations and refinements to this general theme are available, and could be decided upon if and when the next phase of work were initiated. Once identified, time plots of strong parameters could be analyzed for respective partial contributions to the fluctuations found, and time lag between apparent cause and effect could be similarly investigated.

Assuming controlling parameters could be statistically confirmed, the stage should be well set for mathematical modeling. An excellent point of departure exists for this phase of work. We cite the heated island model of Lavoie (1968), wherein predictions of similar inversion activity are made for predicting lines of cumulus build-up.

There is every reason to believe that significant strides could be made in our ability to understand the activity of the Pacific inversion. A program of this nature would be free of field support requirements. Access to routine measurements would be the source of necessary inputs.

We point out also that the present work has revealed the considerable correlation between theoretical flow dynamics and the behavior of inversion distortions at Western Test Range. A Froude number approach would be excellent for prediction and monitoring of local inversion anomalies.

REFERENCES

- Bowen, E. D., "Tradewind Ducting", Rome Air Development Center, Griffiss Air Force Base, New York, Tech. Report No. RADC-TR-64-549, February 1965.
- Carr, T. R., "Tropospheric Propagation Study, Progress Report for 1957," Naval Air Missile Test Center, Tech. Memo Report No. 112, 13 June 1958, 53 pages.
- Enger, II, "An Elementary Description of the Screening Multiple Discriminant Analysis Forecast Technique," Travelers Research Center, Hartford, Connecticut; presented at Fourth Conference Applied Meteorology, Hampton, Virginia, 13 September 1962.
- Kauper, E. K., David F. Hartman and Charlotte J. Hopper, "Smog Forecasting in the Los Angeles Basin", Air Pollution Control District, County of Los Angeles, Air Quality Report No. 37, 1 September 1961, 21 pages.
- Neiburger, M., D. S. Johnson, and Chen-Wu Chien, "Studies of the Structure of the Atmosphere over the Eastern Pacific Ocean in Summer", University of California Publications in Meteorology, 1965.
- Riehl, H., T. C. Yeh, J. J. Malkus, and N. E. LaSeur, "The Northeast Trade of the Pacific Ocean", Quart. Jour. Royal Meteorological Society, Vol. 77, 1951, pp. 598-626.
- Sheddy, C. H., "Refraction of Real Atmosphere and of CRPL Reference Atmosphere Compared", U. S. Navy Electronics Laboratory, San Diego, California, Research Report, 2 February 1966.
- Stanfield, J. W., "An Aid for Predicting Radar Refraction in the Point Mugu Area", U. S. Naval Missile Center, Point Mugu, California, Tech. Memo No. NMC-TM-62-44, 27 September 1962, 18 pages.
- Stidd, C. K., "The Use of Eigenvectors for Climatic Estimates", Jour. of Appl. Meteorology, Vol. 6, No. 2, April 1967, pp. 255-264.
- Lavoie, R. L., 1968: "A numerical model of the atmosphere on the meso-scale with applications to lake-effect storms". Unpublished Ph. D. thesis, Penn State College, State College, Penn.

Security Classification

DOCUMENT CONTROL DATA - R & D

(Security classification of title, body of abstract and indexing annotation must be entered when the overall report is classified)

1. ORIGINATING ACTIVITY (Corporate author) EG&G, Incorporated Environmental Services Operation P O Box 1022 Boulder, Colorado 80302		2a. REPORT SECURITY CLASSIFICATION UNCLASSIFIED	
3. REPORT TITLE AIRBORNE MEASUREMENTS OF ATMOSPHERIC ANOMALIES		2b. GROUP N/A	
4. DESCRIPTIVE NOTES (Type of report and inclusive dates) None			
5. AUTHOR(S) (First name, middle initial, last name) None			
6. REPORT DATE July 1969		7a. TOTAL NO. OF PAGES 110	7b. NO. OF REFS 36
8a. CONTRACT OR GRANT NO. FI9628-68-C-0321		9a. ORIGINATOR'S REPORT NUMBER(S) ESD-TR-69-194	
b. PROJECT NO.		9b. OTHER REPORT NO(S) (Any other numbers that may be assigned this report)	
10. DISTRIBUTION STATEMENT This document has been approved for public release and sale; its distribution is unlimited.			
11. SUPPLEMENTARY NOTES		12. SPONSORING MILITARY ACTIVITY Aerospace Instrumentation Program Office, Electronic Systems Division, AFSC, USAF, L G Hanscom Field, Bedford, Mass. 01730	
13. ABSTRACT Anomalous atmospheric conditions at Western Test Range were measured by aircraft. The inversion layer was found to possess upward warp as it approached the coast, as well as dilation, lensing, sandwiching, and waving. Flow geometry, when associated with topographic obstacles, was found to be markedly similar to that produced on laboratory models. Froude number concepts classified the anomalies accurately. Refraction corrections produced by three possible data sources were compared to assess the effects of the above described anomalies. When data from full cross sections along the sighting path were employed, along with steering equations, elevation and bending corrections were considerably greater (2x) than those produced by single point radiosondes or aircraft spiral measurements. Moreover, corrections produced by spiral data increased to seaward where the inversion became sharply defined. The validity of full cross sections defining the propagation path was best established by examining ray paths for antenna elevation angles existing at the time of signal loss when a target simulation aircraft encountered a radio hole. Ideally, a trapped ray could be expected to bend back to earth at the aircrafts' position in time and space when any one of three tracking radars lost lock on the target. A cross-section corrected propagation path defined this target position better than any other means of defining the path. Strength and distinctive geometry of the inversion at the position of loss are displayed. Mathematics employed for real-time corrections at any angle (including negative) are presented, as are mathematics for steering corrections.			

DD FORM 1473

UNCLASSIFIED

Security Classification